TOPOLOGICAL INSULATORS AND SEMIMETALS IN THE PRESENCE OF INTERACTIONS

BY

MOON JIP PARK

DISSERTATION

Submitted in partial fulfillment of the requirements
for the degree of Doctor of Philosophy in Physics
in the Graduate College of the
University of Illinois at Urbana-Champaign, 2018

Urbana, Illinois

Doctoral Committee:

Professor Michael Stone, Chair
Associate Professor Matthew J. Gilbert, Director of Research
Professor Nadya Mason
Professor Umberto Ravaioli

Abstract

Topological insulators and semimetals possess the exotic gapless excitations that are governed by relativistic quantum mechanics. Due to the growing interests in these phases, the number of the materials predicted and shown to have the topological characters are continuously increasing. Nevertheless, the physical behaviors of the topological materials in the presence of various types of interactions are not well-understood. In this thesis, we study the quantum mechanical responses of the topological insulators and the topological semimetals in the presence of the interactions.

In chapter. 1, we begin our discussion by introducing the general concepts of the topological materials as a prerequisite to understanding the research in the subsequent chapters. We introduce the low energy Hamiltonian and the unique physical responses of the topological insulators and the topological semimetals. In addition, we construct the tight-binding models that are used in the next chapters.

In chapter. 2, we study the superconducting proximity effect in the 3D time-reversal invariant topological insulator(TI)[1]. The 3D TI proximity coupled with s-wave superconductor is predicted to host Majorana fermions. To experimentally detect the Majorana fermions, the 3D TI should be thinner than the decay length of the proximity effect to have the fully superconducting TI surface. We study the superconducting proximity effect on the thin film TI, which has a finite hybridization gap between the top and the bottom surface. By calculating the induced superconducting order parameter in the TI as a function of the hybridization gap, Zeeman energy, and chemical potential, we determine the relevant experimental parameters that harbor the topological superconductivity. Our results offer the relevant experimental parameters in searching for the topological superconductivity and the Majorana fermions in the 3D TI-superconductor proximity systems.

In chapter. 3, we investigate the unconventional superconducting pairing symmetry that may occur in the 3D TI-superconductor proximity coupled system[2]. In the presence of the in-plane Zeeman effect to the TI surface, we find that Fulde-Ferrell(FF) state can be induced in the conventional superconductor. This occurs when the inverse proximity effect(IPE) of the TI to the superconductor is large enough that the normal band of the superconductor possesses a proximity induced spin-orbit coupling and magnetization.

We compare the ground state energies of the FF pairing and the BCS pairing to determine the relevant parameters of the system that energetically favor the FF pairing. When we increase the thickness of the superconductor film, we find that the BCS pairing is more favored than the FF pairing. This is because of the increased number of the metallic bands near the Fermi surface that originally favor the BCS pairing. Our result indicates that the FF pairing can only be found in the thin-film limit of the superconductor.

In chapter 4, we turn our attention from the TI to the superconducting state of Weyl semimetal(WSM). Fulde-Ferrell-Larkin-Ovchinnikov (FFLO) and point nodal BCS state are known to be the possible superconducting states in inversion symmetric doped WSM. To experimentally determine the preferred pairing state, we propose a Josephson junction transport method that shows a unique quantum interference pattern in the presence of FFLO[3]. The Josephson junction consists of a doped WSM and a conventional s-wave superconductor. By applying an external transverse current in the s-wave superconductor, the s-wave order parameter effectively gains a momentum. When the momentum of the s-wave superconductor matches with the momentum of the FFLO states, we find the enhancement of the Josephson current, that serves as an indicator of FFLO states in doped WSMs.

In chapter 5, we study the effect of Anderson-type disorder on inversion symmetric Weyl semimetal[4]. In general, the WSMs can be classified into two types by considering the underlying symmetries: type-I WSMs, that have broken inversion or time-reversal symmetry, and type-II WSMs, that additionally breaks Lorentz invariance. Using the Born approximation, we find that the Anderson disorder renormalizes the topological mass of the WSM. The renormalization of the topological mass induces a quantum phase transition from type-I WSMs to type-II WSMs. The phase transition occurs since the renormalization of the topological mass effectively reduces the Fermi velocity of the Weyl node. We also confirm the disorder-induced phase transitions using the numerical exact diagonalization method on the tight-binding model of the WSM.

In chapter 6, we study the gravitational anomaly of the Weyl and the Dirac fermions[5]. One possible means of studying the topological phases of matter is to examine the quantum anomalies in the boundary theory, which indicates the presence of the non-trivial topology in the higher dimensional bulk. This approach is based on the fact that if the edge theory has a non-trivial response to certain transformations, then the edge theory cannot be consistent on its manifold and will manifest itself as the edge of a higher dimensional system. As such, we calculate the responses of the Weyl fermions on torus under modular transformations, known as large gravitational anomaly. In $(d+1)$-D torus, the modular transformations form $PSL(\mathbb{Z}, d+1)$ group. Using both analytical and numerical regularization methods that support the analytical calculation, we find that both Dirac fermions in $(2+1)$-D and Weyl fermions in $(3+1)$-D are anomaly free under $PSL(\mathbb{Z}, 3)$ and $PSL(\mathbb{Z}, 4)$ groups respectively. Yet, we find that the Weyl fermion still has the gravitational

anomaly when external magnetic field is coupled. We conclude that this is a modification of a mixed chiral anomaly of the Weyl fermion.

To God, for his guidance.

To my parents, for their support.

Acknowledgments

First of all, I would like to thank my advisor, Professor Matthew J. Gilbert. Matthew has supported my graduate study with enlightening discussions and conversations. He has always been enthusiastic about expanding my experience and collaborations with many researchers in academia. He has helped and cared of me on my side whenever I stuck with problems in Doctoral study. Matthew has been not only a great advisor, but he also has been a good mentor and friend over graduate years in Champaign. Without him, I could not successfully finish my doctoral study.

During the five years in the Gilbert group, I have made countless mistakes and written poor drafts. I feel sorry for Matthew, and I also deeply appreciate that he has been patient and helped me to improve these problems. Even at this moment, he carefully went through and helped me with editing this thesis.

I also would like to thank all of my colleagues in the Gilbert group. Youngseok Kim has been my best collaborator. Youngseok was the most reliable person in the office, and he has given me a lot of encouragements during the overall graduate study. As the longest colleague, Tim Philip must have endured a lot of my immaturities. Tim taught me many engineering knowledge, and I always enjoyed the discussions with him. I appreciate Mark Hirsbrunner for being kind to me and closely listening to me. Without him, Tim and I could not finish the interconnect project. I also thank Greg Hamilton. During the Majorana project, he worked hard and tried to follow me during the discussions. I thank Bora Basa for motivating and helping me with the disorder project. Brian Dellabetta and Chen Fang helped me and taught me a lot when I started my research in the Gilbert group. I especially thank Chen for teaching me many field theoretical and mathematical techniques.

I also would like to thank my collaborators and fellows outside the group: Professor Jeffrey Teo, Professor Andrei Bernevig, Professor Nadya Mason, Angela Chen, and Gil Young Cho. Jeffrey has taught me a lot of bosonization languages and strongly correlated systems. I appreciate his patience whenever I bother him with a number of lengthy questions. I thank Andrei Bernevig for offering a lot of helpful criticism when we studied the gravitational anomaly. I feel very lucky that Nadya shared the experimental data, and I could collaborate with Nadya and Angela. It was my first experience to apply my theoretical techniques to the

real experiment, and I could learn lots of experimental wisdom from Nadya and Angela. I also thank Gil Young Cho for giving me countless advice and teaching me many know-hows in physics research. I recognize that I always have tried to catch up with Gil. He has been a good role model.

I must mention the staff members of the physics department. I thank Professor Lance Cooper, Ms. Wendy Wimmer and Ms. Melodee Schweighart for making sure that I get the financial supports. In particular, I cannot forget the moment that I was banned from the United States in my first year. I could not possibly continue my graduate study without the help of the staff members. I sincerely appreciate their efforts to save my visa status and helping me to continue the graduate study. I also appreciate Wendy again for setting up the preliminary exam and the final exam.

I wish to thank my friends in the physics department. I thank Hyuneil Kim for caring about me all the time. He has been the best elder brother and the closest friend of mine. I shared a lot of difficulties and fun moments with him. I cannot express how much Champaign became a boring place after he graduated. I appreciate Sungwook Hong for driving an hour everyday during this winter. We eat together and study together. I wish him good luck in the field of finance. I thank SangJun Lee for hanging out with me and listening to me. I thank Chanul Kim for being the roommate during all the March meetings we have attended. I only would like to express my sincere gratitude to Jiwon Park during the most of the time in the graduate school. I also wish to mention David ChangMo Yang, Junyoung Yang, Jaehyung Yu, Philip Chang, Jungsick Park, Juhyun Ahn, and other friends for giving me many inspirations. My research at Illinois would not have been possible without encouragement of these friends.

I acknowledge financial support from Office of Naval research under grant $N0014-11-1-0123$ and the National Science Foundation (NSF) under grant CAREER EECS-1351871, NSF under Grant No. DMR $17-10437$, and departmental research assistantship in UIUC.

Last but not least, I appreciate my thesis committee members, Professor Michael Stone, Professor Nadya Mason, and Professor Umberto Ravaioli. I am very proud to defend my final exam under the supervision of the great physicists and engineers in Illinois as my committee members.

Table of Contents

Chapter 1

Introduction

As this thesis concerns the topological materials, in this first section, we provide introductory materials to be able to understand the research in the next chapters. The outline of this chapter is as follows. We begin by discussing the first topological insulator, which is the integer quantum Hall effect. After we present the basic properties of the integer quantum Hall effect, we generalize the concept of the integer quantum Hall effect to the topological band insulators that do not require external magnetic fields. The first topological band insulator we introduce is Chern insulator, which breaks the time-reversal symmetry. Then, I introduce the time-reversal invariant topological insulators, whose topological character persists in the presence of the time-reversal symmetry. Lastly, we introduce the Weyl semimetal and its basic physical properties.

1.1 Integer quantum Hall effect

In a two-dimensional electron gas subjected to a perpendicular strong magnetic field, the eigenstates of the electrons form highly degenerate Landau levels[6, 7]. The Landau levels are the states that are analogous to classical cyclotron orbits of the electrons in the presence of the external magnetic field. To begin our discussion, we write down the Hamiltonian of the two-dimensional free electron gas in $\hat{x} - \hat{y}$ plane under a uniform magnetic field, B, pointing $\hat{z}$-direction. The Hamiltonian is given as,

$$H_{IQHE} = \frac{1}{2m}[(p_x - eA_x)^2 + (p_y - eA_y)^2] \tag{1.1}$$

where $\mathbf{A}$ is the vector potential of the magnetic field in the Landau gauge, which is given by $\mathbf{A} = (0, Bx, 0)$. e is electron charge. To simplify the Hamiltonian, we now define new momentum operator Π such that $\Pi_x = p_x$ and $\Pi_y = p_y - \frac{eBx}{c}$. With this new definition, the Hamiltonian can be re-expressed as,

$$H_{IQHE} = \frac{1}{2m}(\Pi_x^2 + \Pi_y^2) \tag{1.2}$$

where Π satisfies the following canonical commutation relation, $[\Pi_x, \frac{c}{eB}\Pi_y] = i\hbar$. By observing the commutation relation and the form of the Hamiltonian, we immediately notice that we can map the system into the well-known problem of the harmonic oscillator by making the following substitution: $\Pi_x \to P$ and $\frac{c}{eB}\Pi_y \to X$. With this substitution, the Hamiltonian becomes

$$\begin{aligned} H_{IQHE} &= \frac{1}{2m}\Pi_x^2 + \frac{1}{2}m\left(\frac{eB}{mc}\right)^2\left(\frac{c}{eB}\Pi_y\right)^2 \\ &= \frac{1}{2m}P^2 + \frac{1}{2}m\omega_0^2 X^2. \end{aligned} \tag{1.3}$$

where $\omega_0 = \frac{eB}{mc}$ is the angular frequency of the harmonic oscillator. The energy levels of the harmonic oscillator are now given as,

$$E_n = \hbar\omega_0(n + \frac{1}{2}), \tag{1.4}$$

where $n \geq 0$ is positive integer. Each harmonic oscillator state is localized by the length scale, often referred to as the magnetic length, $l_b = \sqrt{\frac{m\omega}{\hbar}}^{-1} = \sqrt{\frac{\hbar c}{eB}}$. We may now replace $\frac{c}{eB}\Pi_y = \frac{c}{eB}p_y - x$ as new position operator X. By making this substitution, we notice that the center of the harmonic oscillator is shifted away from zero and now located at $x_0 = \frac{c}{eB}p_y$. As mentioned previously, these energy levels, referred to as Landau levels, are highly degenerate. We can observe this degeneracy in a finite sized sample by examining the area that each Landau level occupies. When the two- dimensional space has the finite size in the $\hat{x}$ and $\hat{y}$-direction, L_x and L_y respectively, the space between the successive momentum is given by $\frac{2\pi}{L_y}$. The confinement of the electrons, $0 < x_0 < L_x$, restricts the allowed ranges of the momentum as, $0 < k_y < \frac{eBL_x}{\hbar c}$. As a result, there must be the degeneracy in the Landau level, which is given as,

$$N = \frac{L_y}{2\pi}\frac{eBL_x}{\hbar c} = \frac{eB}{2\pi\hbar c}L_xL_y. \tag{1.5}$$

We now have the understanding of the Landau level by recasting the Hamiltonian in Eq. (1.1) into the form of the soluble harmonic oscillator problem in (1.3). We now would like to solve for the basic transport properties of the integer quantum Hall effect. To do so, we notice that the energies of the successive Landau levels are separated by $\hbar\omega_0$. If the Fermi energy sits between the Landau levels, the bulk of the system is gapped and in insulating phase. When we turn on a weak electric field, E, along the $\hat{x}$-direction, there are no states available at the Fermi level to conduct within the bulk of the system. As a result, the bulk longitudinal conductance, σ_{xx}, vanishes. However, the Landau level gains a finite group velocity in the $\hat{y}$-direction, $v_y = \frac{\partial E}{\hbar\partial k_y} = \frac{Ec}{B}$, because the potential energy of the electron can be approximated as

$Ex_0 = E\frac{c}{eB}p_y$ when the magnetic length is short enough. This $\hat{y}$-directional group velocity induces a Hall current to the $\hat{y}$-direction, which is given as,

$$j_y = eNv_y = \frac{e^2 L_x L_y}{2\pi\hbar}E. \tag{1.6}$$

The non-zero Hall current can be translated into the quantized Hall conductance, $\sigma_{xy} = \nu\frac{e^2}{2\pi\hbar}$, where v is the number of the occupied Landau levels.

1.2 Chiral edge state

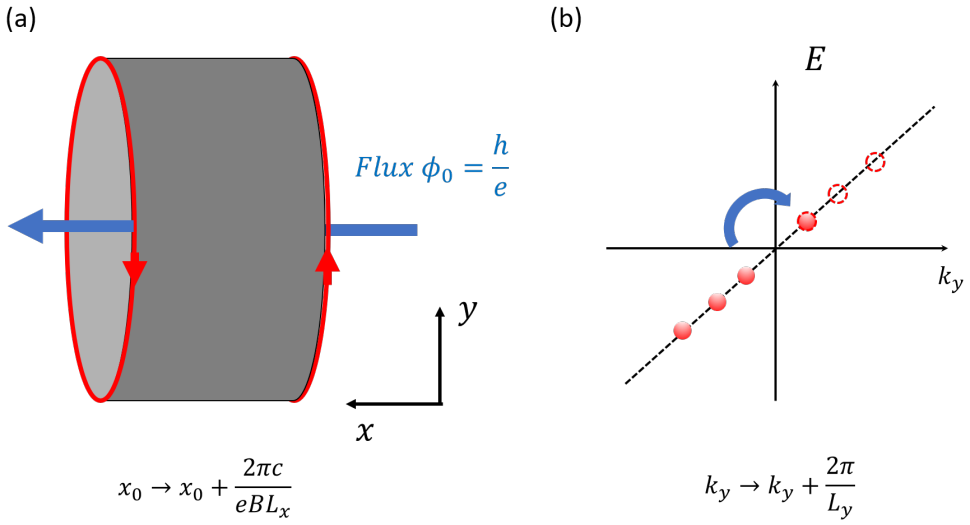

Figure 1.1: (a) Schematic setup of the Laughlin's gauge argument. We consider a cylindrical geometry where the periodic boundary condition along $\hat{y}$-direction and the open boundary condition along $\hat{x}$ direction are taken. The magnetic flux ϕ_0 is adiabatically threaded inside the cylinder. The magnetic flux introduces the adiabatic change of the $\hat{y}$-directional momentum k_y to $k_y + \frac{2\pi}{L}$. The adiabatic change of the momentum operator k_y leads to the change in the center of the harmonic oscillator in Eq. (1.3), such that $x_0 \to x_0 + \frac{2\pi c}{eBL_x}$. This leads to the adiabatic charge pumping from one edge to the other. (b) In the edge perspective, the charge pumping can be understood as a consequence of having chiral edge state. If the chiral edge state exists, the adiabatic shift of the momentum corresponds to loss or gain of the electron charge depending on the chirality of the edge state. In the figure, we can see that the first empty state(dashed circle) is now filled after the shift of the momentum. This is the manifestation of the chiral anomaly in the quantum Hall effect.

Another important aspect of having a finite Hall conductance in the quantum Hall insulator is the appearance of the chiral edge mode on the boundary of the system. A way of understanding the origin of the edge state is the Laughlin's gauge argument for the quantum Hall effect[8]. To begin our discussion, we consider a cylindrical geometry of the quantum Hall fluid where the periodic boundary condition is taken along the y-direction and the open boundary condition is taken along the $\hat{x}$-direction, as shown in Fig. 1.1

(a). We now thread a magnetic flux through the cylinder. The magnetic flux introduces the adiabatic shift of the momentum by, $k_y \rightarrow k_y + \frac{2\pi}{L_y}$. The shift of the momentum leads to the shift of the center of the harmonic oscillator as $x_0 \rightarrow x_0 + \frac{2\pi c}{eBL_y}$. Since each Landau level has the degeneracy of $N = \frac{eB}{2\pi c} L_x L_y$, it is equivalent to that a single electron flows by $\Delta x_0 \times N = L_x$, which is the height of the cylinder. As a result, the adiabatic flux insertion pumps a single electron charge from one edge to the other. This is known as the Laughlin's charge pumping. The Laughlin's charge pumping is the consequence of the finite bulk Hall conductance in the system.

We now focus on what happens on the boundary of the cylinder. When a single electron is adiabatically pumped from one edge to the other, the one edge loses an electron, and the other edge gains the electron. This is seen as non-conservation of the electron charge on the boundary of the cylinder[9, 10, 11]. How can we explain the non-conservation of the electron charge? To answer this question, we postulate that the edge of the cylinder has a gapless chiral edge state. Here, the word 'chiral' means that the number of left moving and the right moving mode are different each other. For example, we can consider the Hamiltonian of a single right-moving chiral edge mode, which is given as,

$$H_{IQHE-edge} = \sum_{k_y} \hbar v_f k_y c^{\dagger}_{k_y} c_{k_y} \tag{1.7}$$

where $k_y = \frac{2\pi(n+\frac{1}{2})}{L_y}$ and n is an integer. Fig. 1.1 (b) shows the dispersion of the right-moving chiral edge mode. If we set the chemical potential equal to zero, the electrons are filled up to the states with negative $k_y (n < 0)$. We now begin to thread the same magnetic flux we did in Fig. 1.1 (a). As the magnetic flux ϕ_0 shifts the momentum by $k_y \rightarrow k_y + \frac{2\pi}{L_y}$, the emptied state with $n = 0$ is now occupied as $n = -1$ state replaces $n = 0$ state. As a result, the number of the occupied electrons is increased by one after the flux insertion. The similar argument also applies to the loss of the electron when the left-moving edge mode exists. Therefore, postulating the chiral edge modes on the boundary of the cylinder explains the Laughlin's charge pumping. In general, one edge may possess both the left-moving and the right-moving edge state, but it cannot have the same number of the gapless state or fully gapped state. Otherwise, the charge pumping between the two edge states of the opposite chirality would be canceled. For this reason, the boundary of the integer quantum Hall effect possess the chiral edge modes.

We have found that the insertion of the magnetic flux leads to the non-conservation of the electron charge within the $1D$ chiral mode. This non-conservation is formally known as the chiral anomaly that generally occurs even space-time dimensions[9, 10, 12]. The chiral anomaly states that the conservation of the electron charge can be broken, when the external electric and magnetic fields are coupled to the chiral fermions. As

such, it is important to note that the chiral mode cannot solely exist in $1D$ material. Otherwise, we can repeat the same argument to insert a magnetic flux in the ring of such a material. The total number of the electron inside the material is not conserved. On a lattice such as condensed matter systems, the chiral mode cannot exist as its own and only exists as an edge state of higher dimensional bulk theory. This is more rigorously known as Nielsen-Ninomiya theorem[13, 11].

1.3 Chern insulator

Not all quantum Hall effects require the presence of the external magnetic field[14]. The necessary ingredient of the quantum Hall effect is the presence of a non-trivial berry curvature that breaks time-reversal symmetry[15]. When the magnetic field is absent and the translational symmetry exists, the Hall conductance can be evaluated by the integral of the Berry curvature over the Brillouin zone(BZ). This integral is known as the Chern number or the TKNN invariant, which is given as[15],

$$C = \frac{i}{2\pi} \int dk_x dk_y (\langle u_k | \partial_{k_x} \partial_{k_y} | u_k \rangle - \langle u_k | \partial_{k_y} \partial_{k_x} | u_k \rangle) \tag{1.8}$$

where u_k is the eigenstate of an occupied band with momentum k. The integrand, $F_{xy}(k)$, is the Berry curvature, $F_{xy}(k) = \langle u_k | \partial_{k_x} \partial_{k_y} | u_k \rangle - \langle u_k | \partial_{k_y} \partial_{k_x} | u_k \rangle$. The Chern number is found to be always an integer-valued quantity when the integral is performed over a lattice BZ. As a result, the Chern number cannot be continuously deformed, and it is therefore referred to as a topological invariant. The non-zero Chern number indicates that the system has a non-zero Hall conductance without the external magnetic field, and it characterizes the quantum anomalous Hall insulator from a trivial insulator[14].

The quantum anomalous Hall insulator, or commonly known as Chern insulator, is the first example of the topological band insulators that have the topological behavior due to the non-trivial electronic band. To better understand the properties of the Chern insulator, we introduce the simplest form of the Chern insulator, using two-band tight-binding model. A two-band Hamiltonian is composed of a set of Pauli matrices,

$$h(k_x, k_y) = \sum_{k_x, k_y} \epsilon(\mathbf{k}) I_2 + n_x(\mathbf{k}) \sigma_x + n_y(\mathbf{k}) \sigma_y + n_z(\mathbf{k}) \sigma_z, \tag{1.9}$$

where σ_i is i-th Pauli matrix, and I_2 is the 2×2 identity matrix. The energy eigenvalue of this Hamiltonian is given as, $E = \epsilon(k) \pm \sqrt{n_x(k)^2 + n_y(k)^2 + n_z(k)^2}$. In the two-band model, the Chern number can be

visualized as skyrmion number, which is given as,

$$C = \frac{1}{4\pi}\int d^2k\hat{\mathbf{n}}\cdot(\partial_{k_x}\hat{\mathbf{n}}\times\partial_{k_y}\hat{\mathbf{n}}) \tag{1.10}$$

We can treat the unit vector $\hat{\mathbf{n}} = \frac{\mathbf{n}}{|\mathbf{n}|}$ as a function of the momentum $(k_x, k_y) \in \mathbb{R}^2$ that maps into the two dimensional surface of the sphere, $\mathbb{S}^2$. In this picture, the skyrmion number is a topological index which counts the number of sphere that the unit vector $\hat{\mathbf{n}} = \frac{\mathbf{n}}{|\mathbf{n}|}$ encircles. To be more concrete, we consider a massive Dirac Hamiltonian in two dimensions that is given by,

$$H_{Chern-continuum} = \sum_k c_k^\dagger(k_x\sigma_x + k_y\sigma_y + m\sigma_z)c_k, \tag{1.11}$$

where m is a mass term that opens a finite energy gap in the Dirac Hamiltonian. In this Hamiltonian, $\mathbf{n}$ is given as, $\mathbf{n} = (k_x, k_y, m)$. Fig. (1.2) (a) shows the distribution of $\hat{\mathbf{n}}$ vector in the momentum space. $\hat{\mathbf{n}}$ points in the $\hat{z}$-direction when $k_x = k_y = 0$. If we continuously increase the momentum to infinite ($|k| \to \infty$), $\hat{\mathbf{n}}$ cants from the $\hat{z}$-direction and converges to the direction parallel to $\hat{\mathbf{n}}||\mathbf{k}$. As a consequence, when considered over the whole BZ, the $\hat{\mathbf{n}}$ vectors cover a hemisphere of $\mathbb{S}^2$. As a consequence, the Chern number of the massive Dirac Hamiltonian is $\pm\frac{1}{2}$ depending on the sign of m.

Based on the analysis using the skyrmion number, we can build a lattice Hamiltonian which has a non-zero Chern number. Unlike the continumm limit, the lattice Hamiltonian must be defined by periodic functions as the lattice BZ is 2π periodic. The lattice version of the Dirac Hamiltonian in Eq. 1.11 can be written as,

$$H_{Chern-lattice} = \sum_k c_k^\dagger(sin(k_x)\sigma_x + sin(k_y)\sigma_y + (2 - cos(k_x) - cos(k_y) + m))c_k. \tag{1.12}$$

In low momentum, $sin(k) \approx k$. Therefore, this Hamiltonian converges to Eq. 1.11. the $cos(k)$ terms are added to gap out the additional Dirac points that arise at corners of BZ at $\mathbf{k} = (\pm\pi, \pm\pi)$. Now we can consider the skyrmion number of the lattice model. In this Hamiltonian, the $\mathbf{n}$ vector is now given as, $(n_x, n_y, n_z) = (sin(k_x), sin(k_y), 2 - cos(k_x) - cos(k_y) + m)$. Fig. (1.2) (b) shows the distribution of $\hat{\mathbf{n}}$. When $m \approx 0^+ > 0$, $\mathbf{n}$ points $+\hat{z}$-direction when $\mathbf{k} = 0$. $\hat{\mathbf{n}}$ starts to cant into $x - y$ plane as $|k|$ increases. However at the corner of BZ, $\mathbf{n}$ points in $+z$ direction again. Therefore, the skyrmion number is zero, identifying the trivial phase. On the other hand, if $m \approx 0^- < 0$, then $\mathbf{n}(k = 0)$ points in $-\hat{z}$-direction. As a consequence, the Chern number is 1, identifying the Chern insulator phase. It is important to note that the Chern number is now integer valued, while the continuum model admits a half-integer Chern number. This discrepancy

can be understood from the observation that the number of the sphere that $\hat{\mathbf{n}}$ vector encircles must be an integer in a periodic domain. As we have seen in the section 1.1.1, the finite Hall conductance in the

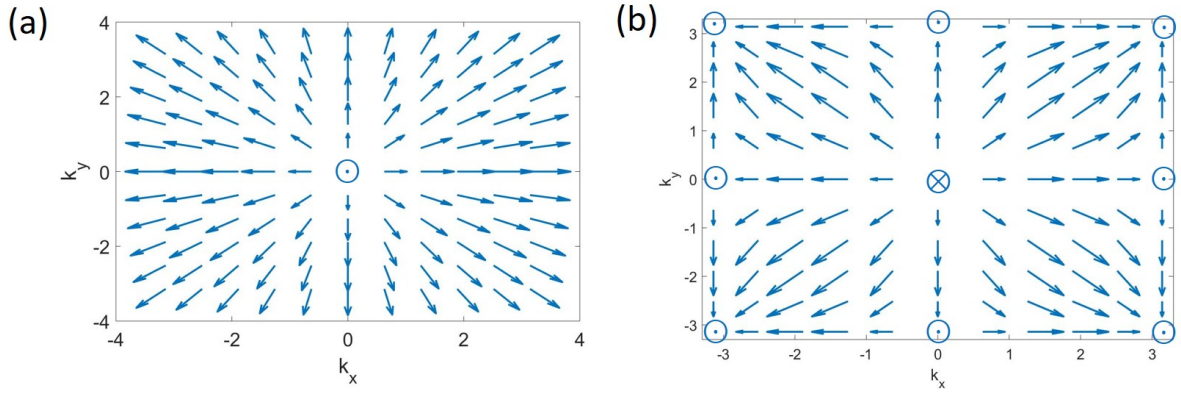

Figure 1.2: (a) $\mathbf{n}$ vector distribution of the massive Dirac fermion in the continuum model. We find that the arrow covers a half of the sphere indicating the Chern number is 1/2. (b) $\mathbf{n}$ vector distribution in the lattice model. At $\mathbf{k} = (0, 0)$, $\mathbf{n}$ point $+\hat{z}$-direction. At $\mathbf{k} = (\pm\pi, 0) = (0, \pm\pi)$, $\mathbf{n}$ point $-\hat{z}$-direction. We find that the Chern number is 1.

integer quantum Hall state manifests itself as a chiral edge state on the boundary of the system. The same argument is true for the Chern insulator. To see the manifestation of the edge state, we explicitly construct the chiral edge mode solution of the Chern insulator Hamiltonian. To do so, we create an interface along the $\hat{y}$-direction and perform the fourier transform along the $\hat{x}$-direction of the Hamiltonian, shown in Eq. 1.11. As a result, we now have the real-space Hamiltonian, which is given as,

$$H_{Chern-domainwall} = \sum_k c_k^\dagger(-i\partial_x\sigma_x + k_y\sigma_y + m\frac{x}{|x|})c_k. \tag{1.13}$$

where $m\frac{x}{|x|}$ now models a domain wall dividing the two insulating phases having the Chern number $\pm\frac{1}{2}$. The above Hamiltonian possess a gapless solution of the energy $E = k_y$ that is given by,

$$\psi_{k_y} = e^{ik_y y}e^{-|m|x}(1, 1)^T. \tag{1.14}$$

This state is localized on the interface as can be seen by the exponential dependence in position in Eq. (1.14). Given the eigenstate and the eigenenergy, we derive the effective Hamiltonian of chiral edge state localized on the interface between two insulators,

$$H_{Chern-edge} = \sum_{k_y} k_y\psi_{k_y}^\dagger\psi_{k_y}. \tag{1.15}$$

Therefore, the Chern insulator possesses a chiral edge state in a similar fashion to that of the integer quantum Hall effect. In general, the Chern number can be any integer. In this case, the same number of the chiral edge modes propagate in the same direction and are protected from the backscattering. Since any electron tunnelings between the chiral edge modes are forward scattering processes that only renormalize the velocity and cannot introduce a mass. Therefore, the Chern insulator phase has $\mathbb{Z}$ topological classification.

1.3.1 Haldane Model

Haldane model effectively realizes the Chern insulator phase[14]. To describe the Haldane model, we consider a honeycomb lattice that consists of A and B atoms as shown in Fig. 1.3 (a). We define the translational vector of the lattice $\mathbf{a}_1 = \frac{1}{2}(3, \sqrt{3})$, $\mathbf{a}_2 = \frac{1}{2}(3, -\sqrt{3})$ and $\mathbf{a}_3 = \mathbf{a}_1 - \mathbf{a}_2$, where each bond has the length 1. In the honeycomb lattice, we add a periodic magnetic flux in the $\hat{z}$-direction normal to the plane of the lattice. We assume that this periodic flux has the zero-net flux in each unit cell. The magnetic flux adds a phase to the hopping term from the site, r_j, to the site, r_i, through the Peierls substitution as,

$$t_{\mathbf{r}_i,\mathbf{r}_j} c^\dagger_{\mathbf{r}_i} c_{\mathbf{r}_j} \rightarrow t_{\mathbf{r}_i,\mathbf{r}_j} e^{i\frac{e}{\hbar}\int_{\mathbf{r}_j}^{\mathbf{r}_i} \mathbf{a}\cdot d\mathbf{r}} c^\dagger_{\mathbf{r}_i} c_{\mathbf{r}_j}. \tag{1.16}$$

where a is the vector potential describing the magnetic flux. Since the net flux is zero, we can choose a gauge that the nearest-neighbor hopping term does not change. However, the next nearest-neighbor hopping term gains the phase ϕ. As a result, the Hamiltonian of this honeycomb lattice can be written as,

$$H_{Haldane} = t_1 \sum_{<i,j>} c^\dagger_i c_j + t_2 \sum_{<<i,j>>} e^{-iv_{ij}} c^\dagger_i c_j + M \sum_{i=A} c^\dagger_i c_i - M \sum_{i=B} c^\dagger_i c_i, \tag{1.17}$$

where M is the on-site energy level difference between A and B atoms. the t_1 and t_2 are the nearest hopping term and the next-nearest hopping term respectively. v_{ij} is the Peierls phase that takes the value of $\pm\phi$ depending on the orientation. The real space Hamiltonian in Eq. (1.17) can be Fourier transformed into the momentum space Bloch Hamiltonian that is given by,

$$\begin{aligned} h(k_x, k_y) = 2t_2 cos(\phi)(\sum_{i=1,2,3} cos(\mathbf{k}\cdot\mathbf{a}_i))I_2 + t_1((\sum_{i=1,2} cos(\mathbf{k}\cdot\mathbf{a}_i) + 1)\sigma_x + \sum_{i=1,2} sin(\mathbf{k}\cdot\mathbf{a}_i)\sigma_y) \\ +(M + 2t_2 sin(\phi)(sin(\mathbf{k}\cdot\mathbf{a}_1) - sin(\mathbf{k}\cdot\mathbf{a}_2) - sin(\mathbf{k}\cdot\mathbf{a}_3)))\sigma_z. \end{aligned} \tag{1.18}$$

To further analyze this Hamiltonian, we expand the Hamiltonian near $K = \frac{2\pi}{3}(1, \frac{1}{\sqrt{3}})$ and $K' = \frac{2\pi}{3}(1, -\frac{1}{\sqrt{3}})$. This can be done by taking the Taylor expansion at $K(K') + \kappa$, which is given as,

$$
\begin{aligned}
& h(K_x + \kappa_x, K_y + \kappa_y) \qquad (1.19)\\
&= t_1[(cos(\frac{4\pi}{3} + \kappa \cdot \mathbf{a}_1) + cos(\frac{2\pi}{3} + \kappa \cdot \mathbf{a}_2) + 1)\sigma_x + (sin(\frac{4\pi}{3} + \kappa \cdot \mathbf{a}_1) + sin(\frac{2\pi}{3} + \kappa \cdot \mathbf{a}_2))\sigma_y] \\
&\approx \frac{3}{2}t_1(k_x\sigma_x - k_y\sigma_y) + (M - 3\sqrt{3}t_2 sin(\phi))\sigma_z - 3t_2 cos(\phi) I_2, \\
& h(K'_x + \kappa_x, K'_y + \kappa_y) \\
&\approx \frac{3}{2}t_1(-k_x\sigma_x + k_y\sigma_y) + (M + 3\sqrt{3}t_2 sin(\phi))\sigma_z - 3t_2 cos(\phi) I_2.
\end{aligned}
$$

When $M = t_2 = 0$, the above Hamiltonian reduces to the model of the graphene, having the massless Dirac fermions at K and K'. As soon as we turn on the non-zero M and t_2, the two Dirac points are gapped. t_2 contributes to the mass gap with the opposite signs on K and K', while M contributes as the same signs. According to the analysis in Eq. (1.11), we know that a single gapped Dirac fermion contributes to the Chern number $\pm\frac{1}{2}$ depending on the sign of the mass gap. Therefore, the Haldane model has the Chern number $1 = \frac{1}{2} + \frac{1}{2}$ or $-1 = -\frac{1}{2} - \frac{1}{2}$ when the two Dirac cones have the opposite signs of the mass. If the two Dirac cones gain the mass with the same sign, the Chern number is zero, $0 = \frac{1}{2} - \frac{1}{2}$.

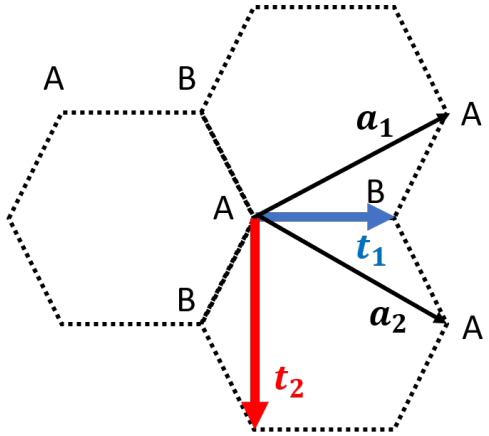

Figure 1.3: Schematic figure of the Haldane model in honeycomb lattice. a_1 and a_2 are the lattice translational vectors. t_1 and t_2 are the nearest neighbor hopping term and the next nearest hopping term respectively.

1.4 Time-reversal symmetry

Before considering the time-reversal invariant topological insulator, we explain the time-reversal symmetry in general context. The time-reversal symmetry is an anti-unitary operator which reverses the momentum and the spin of the electrons simultaneously. To be explicit, the time-reversal symmetry in a spinless system can be written as,

$$T : c_k \to c_{-k}, \tag{1.20}$$

which squares to 1. Similarly, in the spin-$\frac{1}{2}$ system, it can be written as,

$$T : c_{k,\uparrow} \to c_{-k,\downarrow}, \tag{1.21}$$

$$c_{k,\downarrow} \to -c_{-k,\uparrow}, \tag{1.22}$$

which squares to (-1). The additional -1 phase is the consequence of the 2π rotation in $SU(2)$ group. In the presence of the time-reversal symmetry, the Chern number must vanish. For example in a spinless system, this can be seen by observing that the time-reversal symmetry place a constraint on the Berry curvature as

$$F_{ij}(k_x, k_y) = -F_{ij}(-k_x, -k_y). \tag{1.23}$$

As a consequence, the integration of the Berry curvature always becomes zero, leading to the trivial phase. In the presence of the time reversal symmetry, the quantum Hall effect cannot exist.

In addition, imposing the time-reversal symmetry in the system places a constraint on the explicit form of the Hamiltonian. To derive the constraint, we consider the generic form of the spin-1/2 Hamiltonian, which is written by,

$$H_{TRS} = \sum_{\mathbf{k}} c^{\dagger}_{s,a,\mathbf{k}} h_{ss'aa'}(k) c_{s',a',\mathbf{k}} \tag{1.24}$$

where s and a are the spin and the orbital degree of the freedom. By acting the time-reversal symmetry

upon the Hamiltonian, the above Hamiltonian transforms as,

$$
\begin{aligned}
TH_{TRS}T^{-1} = \sum_{\mathbf{k}} & Tc^{\dagger}_{s,a,\mathbf{k}} h_{ss'aa'}(k) c_{s',a',\mathbf{k}} T^{-1} \\
\sum_{\mathbf{k}} & i\sigma_{y_{s,s''}} c^{\dagger}_{s'',a,-k} h_{ss'aa'}(k)^* i\sigma_{y_{s',s'''}} c_{s''',a',-k} \\
\sum_{\mathbf{k}} & c^{\dagger}_{s'',a,\mathbf{k}} - i\sigma_{y_{s'',s}} h_{ss'aa'}(-k)^* i\sigma_{y_{s',s'''}} c_{s''',a',\mathbf{k}}
\end{aligned}
\tag{1.25}
$$

By equating the above Hamiltonian with the one in Eq. (1.24), we find that the time-reversal symmetric Hamiltonian needs to satisfy the following condition,

$$
h_{ss'aa'}(k) = -i\sigma_{y_{s,s_1}} h_{s_1,s_2,a,a'}(-k)^* i\sigma_{y_{s_2,s'}}. \tag{1.26}
$$

Another consequence of the time-reversal symmetry in the spin-$\frac{1}{2}$ system is the presence of the Kramer's theorem. The Kramer's theorem states that when the time-reversal symmetry is preserved, there exist at least two degeneracy at the high symmetry points of the time-reversal symmetry. This degeneracy is known as the Kramer's degeneracy. To prove this theorem, we consider the eigenstate, $|\psi>$, at a time-reversal symmetric point in the BZ. Its time-reversal partner $T|\psi>$ is also the eigenstate of the same energy since $[H,T]=0$. T can be generally written as the product UK, where K is the complex conjugate operator and U is the generic unitary operator, satisfying $U^T = -U^{-1}$. The wave function overlap of $|\psi>$ and its time-reversal partner $T|\psi>$ can be evaluated as,

$$
<\psi|T|\psi> = \sum_{i,j} \psi_i U_{ij} K\psi_j = -\sum_{i,j} \psi^*_j U_{ji} K\psi_i = -<\psi|T|\psi> = 0 \tag{1.27}
$$

Since the wave function overlap is zero, the two wave functions are orthogonal each other, indicating the presence of the degeneracy.

1.5 Time-reversal Invariant Topological Insulator

In the presence of the time-reversal symmetry, the Chern number vanishes. However, the concept of the topological insulator can be further generalized to the time reversal symmetric system[16, 17, 18]. The first example of realizing this phase is the quantum spin Hall insulator[17]. The Hamiltonian of the quantum spin Hall insulator consists of the two copies of the Chern insulator for each spin sector. The Chern insulator of the spin-up sector has the opposite Chern number of the spin-down sector. The Hamiltonian can be

explicitly written as,

$$H_{QSH} = c_k^\dagger \begin{pmatrix} d_x(k)\sigma_x + d_y(k)\sigma_y + d_z(k)\sigma_z & 0 \\ 0 & d_x(k)\sigma_x + d_y(k)\sigma_y - d_z(k)\sigma_z \end{pmatrix} c_k \tag{1.28}$$

where $c_k = (c_{A,\uparrow}, c_{A,\downarrow}, c_{B,\uparrow}, c_{B,\downarrow})^T$ and A, B are the orbital degree of the freedom. $\mathbf{d}(k) = (sin(k_x), sin(k_y), 2 - cos(k_x) - cos(k_y) + M)$. The upper and lower block-diagonal part of the above Hamiltonian are the exactly same as the massive Dirac Hamiltonian of the Chern insulator but with the opposite mass in Eq. (1.12). Therefore, each block-diagonal Hamiltonian possesses the Chern number ± 1 when $m \approx 0^- < 0$. H_{QSH} is in the insulator phase as can be seen from the energy spectrum of the Hamiltonian, which is given as,

$$E_{QSH}(k_x, k_y) = \pm\sqrt{sin(k_x)^2 + sin(k_y)^2 + (2 - cos(k_x) - cos(k_y) + M)^2}. \tag{1.29}$$

H_{QSH} preserves the time-reversal symmetry. This can be explicitly checked by using the condition in Eq. (1.26).

As the quantum spin Hall insulator consists of the two Chern insulator, the edge of the quantum spin Hall insulator possesses a couple of the counter-propagating chiral edge states, which is known as the helical edge states. The Hamiltonian of the helical edge state can be written as,

$$H_{QSH-edge} = \sum_k c_k^\dagger \begin{pmatrix} \hbar v_f k & 0 \\ 0 & -\hbar v_f k \end{pmatrix} c_k \tag{1.30}$$

In general, the helical edge state can be gapped out by adding a backscattering term between each spin sector. For example, we can add σ_x or σ_y mass term to gap out the edge state. However, these mass terms flip spin-up electrons to spin-down electrons and vice versa. Therefore, the time-reversal symmetry must be broken by such a mass term. On the other hand, as long as the time-reversal symmetry is preserved, the helical edge state is topologically protected. This is the notion of the time-reversal invariant topological insulator. In a more general terminology, it is called symmetry protected topological phase in a sense that the time-reversal symmetry is necessarily present to have the topological protection.

While any integer number of chiral edge state is protected by the integer-valued Chern number, the helical edge state has weaker protection called $\mathbb{Z}_2$ number. In this section, rather than defining a rigorous $\mathbb{Z}_2$ invariant, we explicitly show that the even number of the helical edge state can be gapped out without breaking the time-reversal symmetry. We write down the two copies of the helical edge state, which is

written by,

$$H_{QSH-edge2} = \hbar v_f k \sigma_z \otimes I_2 \tag{1.31}$$

where I_2 is two-dimensional identity matrix. In this case, we can add the time-reversal symmetric mass term which is given as,

$$H_{TRS-mass} = m\sigma_1 \otimes \tau_2. \tag{1.32}$$

Although the time-reversal symmetry flips spin to reverse the sign of σ_2, τ_2 reverses the sign again since the time-reversal symmetry is an anti-unitary operator. Therefore, the above mass is still allowed. The eigenvalues of the helical edge in the presence of the above mass term is given by,

$$E_k = \pm\sqrt{(\hbar v_f k)^2 + m^2}, \tag{1.33}$$

, which explicitly shows that the edge state is now gapped. Therefore, the time-reversal symmetric topological insulator has $\mathbb{Z}_2$ classification, because the two copies can be gapped out without breaking the time-reversal symmetry.

1.5.1 Kane-Mele model

Kane and Mele first proposed the time-reversal symmetric topological insulator model in the honecomb lattice by modifying the Haldane model[16]. In the Kane-Mele model, the spin-orbit coupling plays a central role that substitutes the role of the magnetic flux in the Haldane model. However unlike the Haldane model, the spin-orbit coupling preserves the time-reversal symmetry by effectively realizing the model Hamiltonian in Eq. (1.28). To describe the model, we begin with the honeycomb lattice Hamiltonian in Eq. (1.19) without the mass, M, and the next neareset neighbor hopping t_2. We instead add the spin-orbit coupling term, which is given as,

$$H_{SO} = -t_3 \sum_{<<i,j>>} i v_{ij} c_i^\dagger s_z c_j \tag{1.34}$$

where s is the Pauli matrix for the spin degree of the freedom. This term is very similar to the magnetic flux in the Haldane model, however it flips the sign when the spin is flipped. By oberserving the mathematical

similarity with the Haldane model, we can expand the Hamiltonian again near K and K' point as,

$$h(K_x + \kappa_x, K_y + \kappa_y) \approx \frac{3}{2} t_1 (k_x \sigma_x - k_y \sigma_y) - 3\sqrt{3} t_3 \sigma_z s_z, \tag{1.35}$$
$$h(K'_x + \kappa_x, K'_y + \kappa_y) \approx \frac{3}{2} t_1 (-k_x \sigma_x + k_y \sigma_y) + 3\sqrt{3} t_3 \sigma_z s_z.$$

Firstly, we immediately notice that this low energy Hamiltonian coincide with the low energy Hamiltonian of the quantum spin Hall insulator in Eq. (1.28). We also notice that the spin-orbit coupling, t_3 induces the same mass gap as t_2 in the Haldane model, but the sign is now dependent on the spin. Therefore, a non-zero small t_3 induces the opposite and the nonzero Chern number for each spin sector of the Hilbert space. While the total Chern number is zero by summing up the whole spin sectors, the opposite Hall conductance for each spin generates a non-zero spin Hall conductance, which is given as,

$$\sigma_{xy} = 2 \frac{e^2}{2\pi\hbar}. \tag{1.36}$$

This quantized spin Hall conductance characterizes the quantum spin Hall effect.

1.5.2 3D Time-reversal Invariant Topological Insulator

We can generalize the idea of the two-dimensional time-reversal invariant topological insulator to three-dimensions by considering a massive Dirac fermion in three-dimensions[18]. The Hamiltonian of the three dimensional Dirac fermion can be derived by adding the additional k_z-directional dispersion to the Hamiltonian of the two dimensional Dirac fermion. Thus, the lattice Hamiltonian of the three dimensional Dirac fermion can be written in the similar form as,

$$H(k_x, k_y, k_z)_{3DTI} = c_k^\dagger [\sum_{i=x,y,z} (sin(k_i)\Gamma^i + cos(k_i)\Gamma^0) + (m-3)\Gamma^0] c_k \tag{1.37}$$

where $\Gamma^0 = I_2 \otimes \tau_z$ and $\Gamma^a = \sigma_a \otimes \tau_x$ are the Gamma matrices, and σ and τ are the Pauli matrices for the spin and orbital degree of freedom respectively. We can see that this Hamiltonian is in the insulating phase when $m \sim 0^+ > 0$ by solving for the dispersion, which is given as,

$$E_{QSH}(k_x, k_y, k_z) = \pm \sqrt{sin(k_x)^2 + sin(k_y)^2 + sin(k_z)^2 + (3 - cos(k_x) - cos(k_y) - cos(k_z) + M)^2}. \tag{1.38}$$

In the similar manner as the $2D$ time-riversal invariant topological insulator, the $3D$ topological insulator has the two dimensional helical surface state. This can be seen by explicitly solving for the bulk Hamiltonian

with the open boundary condition. To do so, we create a mass domain wall along the $\hat{z}$-direction while keeping the periodic boundary condition in the $\hat{x}$- and $\hat{y}$-directions. By taking the continuum limit near the Γ point, the Hamiltonian in Eq. (1.39) can be approximated as,

$$h(k_x, k_y)_{3DTI} = -i\partial_z \Gamma^z + \sum_{i=x,y} sin(k_i)\Gamma^i + m\frac{z}{|z|}\Gamma^0 \tag{1.39}$$

The above Hamiltonian possesses a couple of the zero energy solutions at $(k_x, k_y) = (0, 0)$, that will turn out to be the basis of the surface state. The solutions are given by,

$$\psi_1 = e^{-|m|z}(0, 1, 0, -1)^T. \tag{1.40}$$
$$\psi_2 = e^{-|m|z}(0, 1, 0, 1)^T.$$

These states are localized on the domain wall as can be seen by the exponential dependence in position in Eq. (1.40). Given the zero energy eigenstates, we derive the effective Hamiltonian of the surface state by acting upon the bulk Hamiltonian as a function of k_x and k_y,

$$H_{effective-surf,top} = (\psi_1\psi_2)^\dagger h(k_x, k_y)_{3DTI}(\psi_1\psi_2) = k\sigma_x + k\sigma_y. \tag{1.41}$$

As a result, the surface of the three dimensional topological insulator possesses the 2D gapless Dirac fermions. We can solve for the opposite surface state by inverting the sign of the mass term. By doing the same calculation, we find that the opposite surface has the effective Hamiltonian given as,

$$H_{effective-surf,bottom} = -k\sigma_x - k\sigma_y. \tag{1.42}$$

The 3D time-reversal invariant topological insulator also has $\mathbb{Z}_2$ classification. This can be checked by adding time-reversal symmetric mass gap when there are two copies of the surface state. To do so, we write down the two copies of the helical edge state, which is written by,

$$H_{QSH-edge2} = \hbar v_f(k\sigma_x + k\sigma_y) \otimes I_2 \tag{1.43}$$

In this case, we can add the time-reversal symmetric mass term which is given as,

$$H_{TRS-mass} = m\sigma_1 \otimes \tau_2 \tag{1.44}$$

The eigenvalues of the surface state with the above mass Hamiltonian is given by,

$$E_k = \pm\sqrt{(\hbar v_f k_x)^2 + (\hbar v_f k_y)^2 + m^2} \tag{1.45}$$

, which gives the gapped Dirac surface. Therefore, the 3D time-reversal symmetric topological insulator has $\mathbb{Z}_2$ classification.

1.6 Weyl semimetal

To this point, we have discussed the topological insulator phases that harbor unique gapless states on their boundaries. In this section, we discuss the topological semimetal phases which have topologically protected gapless bulk states. Weyl semimetals are topological semimetal phase whose low energy excitations are described by three-dimensional Weyl fermions[19]. The Hamiltonian of the Weyl fermions can be generally written as,

$$H_{Weyl} = \sum_k c_k^\dagger (v_{f,x} k_x \sigma_x + v_{f,y} k_y \sigma_y + v_{f,z} k_z \sigma_z) c_k \tag{1.46}$$

where $sign(v_{f,x} v_{f,y} v_{f_z})$ defines the chirality of the Weyl fermion. H_{Weyl} has a two-fold degeneracy at $\mathbf{k} = 0$, often referred to as Weyl point or Weyl node. In solid-state systems, either inversion or time-reversal symmetry must be broken to realize the Weyl semimetal. Otherwise, these symmetries ensure that the bands are doubly degenerate, which contradicts with the non-degenerate Hamiltonian in Eq. (1.46). Within this two band model of the Weyl fermion, any single-body perturbation cannot gap out the energy spectrum. This can be explicitly seen by adding a mass term in Eq. (1.46). Any arbitrary mass term of the Pauli matrix $m\sigma_i$ can be absorbed into the momentum by the transformation such that $k_i \to k_i + \frac{m}{v_f}\sigma_i$. The consequence is to shift the location of the Weyl point but it does not gap out the energy spectrum. Therefore, the Weyl semimetals that possesses the Weyl fermions have the robust metallic bulk states.

However, the robust metallic states of the Weyl semimetal are not immune to any arbitrary strength of the perturbation. To better understand the stability of the Weyl semimetal, we transform the Hamiltonian in Eq. (1.46) into the lattice version by

$$H_{WSM} = v_f \sum_k c_k^\dagger [sin(k_x)\sigma_x + sin(k_y)\sigma_y + (2 - cos(k_x) - cos(k_y) + sin(k_z))\sigma_z] c_k \tag{1.47}$$

By expanding H_{WSM} near $\mathbf{k} = (0, 0, 0)$, we recover the Weyl Hamiltonian in the continuum version of Eq.

(1.46) that is given by,

$$H_{Weyl,k_z\sim 0} = v_f \sum_k c_k^\dagger [k_x\sigma_x + k_y\sigma_y + k_z\sigma_z] c_k. \tag{1.48}$$

However, if we expand H_{WSM} near $\mathbf{k} = (0, 0, \pi)$, we find another Weyl fermion that is given as,

$$H_{Weyl,k_z\sim \pi} = v_f \sum_k c_k^\dagger [k_x\sigma_x + k_y\sigma_y - k_z\sigma_z] c_k. \tag{1.49}$$

As a result, the lattice Hamiltonian possesses another Weyl fermion of the opposite chirality. The presence of the additional Weyl fermion is an inevitable consequence of the Nielsen-Ninomiya theorem, which states that the Weyl fermions must exist as pairs in lattice model of even space-time dimensions. When the Weyl fermions with the opposite chirality exist in the BZ, they can be simultaneously gapped out. To see this, we consider a pair of the Weyl fermion sitting in the same position in the BZ. The Hamiltonian is given as,

$$h_{Weyl,pair}(k_x, k_y, k_z) = (k_x\sigma_x + k_y\sigma_y - k_z\sigma_z)\tau_z. \tag{1.50}$$

We now notice that this is equivalent to the massless Dirac fermion, which is the Hamiltonian of the 3D topological insulator without the mass term. Thus, this Hamiltonian can be gapped out by breaking the time-reversal symmetry as we have seen in section 1.1.5.

The Weyl semimetal phase also possesses non-trivial edge states, called Fermi arc[20]. The presence of the Fermi arc can be seen by considering the 2D slice of the Hamiltonian at fixed k_z in Eq. (1.47). At the fixed k_z, we notice that the effective $2D$ Hamiltonian is equal to the Hamiltonian of the Chern insulator in Eq. (1.12) but with the mass term replaced by $sin(k_z)$. Therefore, each $2D$ slice has the chiral edge mode if the effective mass, $sin(k_z)$, is in the topological phase. According to the criterion in section 1.1.3, the 2D slice is equivalent to the Chern insulator if $0 < k_z < \pi$. If $0 > k_z$ or $k_z > \pi$, the 2D slice corresponds to the trivial insulator. As a consequence, the chiral edge state only exists in the finite interval of the momentum, $k_z \in [0, \pi]$. This is realized as the open line segment of the Fermi surface, which is known as the Fermi arc. The Fermi arc ends at the two points where two Weyl points are projected on the surface. This is because the Weyl points in the bulk become the gapless transition that changes the Chern number. Since the Weyl semimetal can be regarded as the stacks of the Chern insulator in the momentum space, the Weyl semimetal exhibit the large Hall conductance that is proportional to the number of lattice points between the two Weyl

fermions, which is given as,

$$\sigma_{xy} = \frac{\Delta k}{2\pi} N \frac{e^2}{h}. \tag{1.51}$$

Another form of the Weyl fermion can be reazlied when we add the identity matrix to Eq. (1.46) rather than the Pauli matrix[21]. To see this, we consider the modified Hamiltonian that is given as,

$$H_{Weyl} = \sum_k c_k^\dagger (v_f k_x \sigma_x + v_f k_y \sigma_y + v_f k_z \sigma_z + \alpha k_x I_2) c_k \tag{1.52}$$

We now have the additional $\alpha k_x I_2$ term. The effect of this term is to tilt the angle of the Weyl fermion to the $\hat{x}$-direction. Fig. (1.4) shows the band structure of the Weyl fermion with the α term. When $\alpha = 0$, the Weyl fermion has a circular Fermi surface which is equivalent to the relativistic massless fermion. However when a non-zero α is turned on, the Weyl fermion starts to tilt. At the critical value when $\alpha = v_f$, the Fermi surface undergoes a Lifshitz transition from the eliptical Fermi surface to the hyperbolic Fermi surface. The Weyl fermion having the hyperbolic Fermi surface is called type-II Weyl fermion[21].

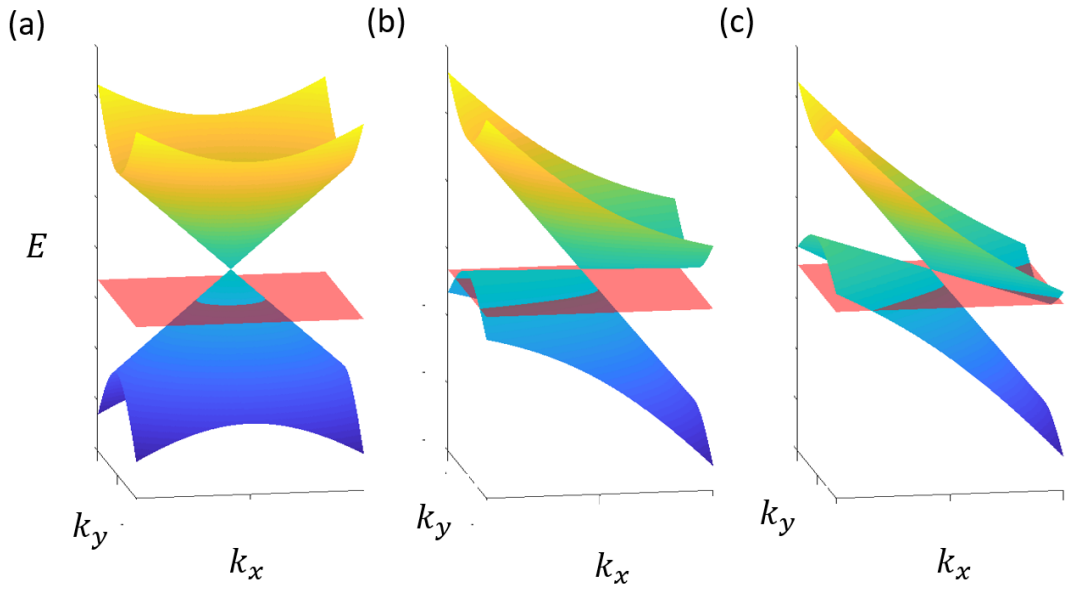

Figure 1.4: Schematic diagram of the tilted Weyl fermion. (a) In the absence of the tilting term, $\alpha = 0$, the Weyl fermion has the elliptical Fermi surface. (b) When $\alpha = v_f$ matches the Fermi velocity, the Fermi surface becomes a parabola. (c) If $\alpha > v_f$ exceeds the Fermi velocity, the Fermi surface undergoes a lifshitz transition to the hyperbola, characterizing the type-II Weyl fermion.

1.6.1 Burkov-Balents model

In this subsection, we review the Burkov-Balents model[22], which realizes the Weyl semimetal in topological insulator multilayer. The basic building block of this model is the surface state of the magnetically doped $3D$ topological insulator in Eq. (1.39) which is given as,

$$H_{TIsurf} = \pm v_f(k_x\sigma_x + k_y\sigma_y + m\sigma_z) \tag{1.53}$$

where v_f is the Fermi velocity of the topological insulator surface state. m is the Zeeman interaction term caused by the magnetic doping. σ is the Pauli matrix for the spin. $\pm$ sign indicates the helicity of the surface depending on the top and the bottom surface of the topological insulator. Within this model, we ignore the bulk states of the topological insulator by assuming that the chemical potential is near the Dirac points of the surface states. We now consider the multilayers of the topological insulator-normal insulator heterostructure, as shown in Fig. 1.5 (a). In general, the thickness of the topological insulator and the normal insulator can be different. This introduces different interlayer hopping between the topological insulators, Δ_s, and the normal insulators, Δ_d, respectively. By adding the interlayer hopping term, the real space Hamiltonian in the $\hat{z}$-direction can be written as,

$$H_{Burkov-Balents} = \sum_{i,j}(v_f(k_x\sigma_x + k_y\sigma_y)\tau_z + m\sigma_z + \Delta_s\tau_x)\delta_{i,j} + \frac{1}{2}(\Delta_d\tau_+\delta_{i,j-1} + \Delta_d\tau_-\delta_{i-1,j}) \tag{1.54}$$

where τ_z is the Pauli matrix indicating the top/bottom surface degree of freedom. i and j indicates the $\hat{z}$-directional coordinates where the multi-layer is stacked. $\tau_\pm = \frac{1}{2}(\tau_x \pm \tau_y)$. By diagonalizing the Hamiltonian, we derive the expression for the dispersion given as,

$$E = \pm\sqrt{v_f^2(k_x^2 + k_y^2) + (m \pm \sqrt{\Delta_s^2 + \Delta_d^2 + 2cos(k_z)\Delta_s\Delta_d})^2} \tag{1.55}$$

First of all, we notice that when $m = 0$, the energy spectrums are two-fold degenerate. This is the consequence of the simutaneous presence of the time-reversal and inversion symmetry. To realize the Weyl semimetal phase, we need to break the time-reversal symmetry by considering case when $m \neq 0$. When $m \neq 0$, we find the gapless points in Eq. (1.55) in BZ, which is given as,

$$kz_0 = arccos(1 - (m^2 - (\Delta_s - \Delta_d)^2)/2\Delta_s\Delta_d \tag{1.56}$$

if the Zeeman sits in the range of,

$$(\Delta_s - \Delta_d)^2 < m^2 < (\Delta_s + \Delta_d)^2 \tag{1.57}$$

As a result, when the non-zero Zeeman term lifts the degeneracy of the bands, a stable Weyl semimetal phase can be realized.

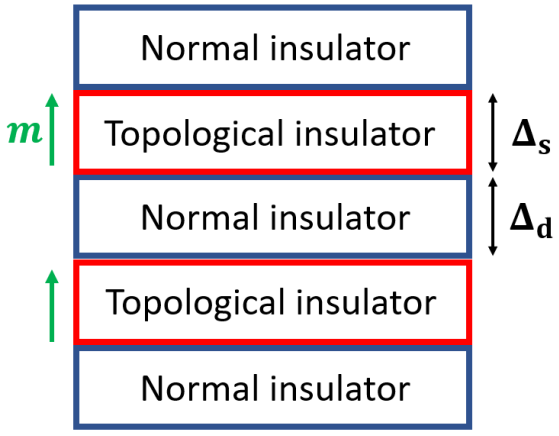

Figure 1.5: Schematic figure of the Burkov-Balents model that is constructed using the magnetically doped topological insulator multilayer. Each topological insulator is sandwitched by trivial insulators.

Chapter 2

Topological superconductivity in an ultrathin, magnetically-doped topological insulator

[1]

2.1 Introduction

In chapter 1, we have found that the insulators can possess the non-trivial topology and the metallic edge states characterizing the topological characters. After the discovery of the topological insulators, it was recognized that the concept of the band topology can be applied to the various phases possessing a finite energy gap. One such phase is the superconductor. The superconductors possess a finite energy gap that is caused by the effective attractive interactions between the electrons. When the superconductors possess the non-trivial band topology, it harbors the in-gap boundary states, known as Majorana fermions[23, 24].

There has been a significant effort to find systems that exhibit topological superconductivity as such systems are predicted to harbor the, heretofore, elusive Majorana fermions[25, 26, 27, 28]. There have been a number of proposals that have been predicted to realize topological superconductivity, and these proposals may be grouped into two: (i) unconventional superconducting materials such as Sr_2RuO_4[29, 30, 31] or doped superconducting materials such as $Cu_xBi_2Se_3$[32, 33, 34] and (ii) proximity-coupled system comprised of a conventional superconductor and a system such as strongly spin-orbit coupled semiconductors[35], magnetic adatoms[36, 28], or 3D time-reversal invariant (TRI) topological insulators (TI)[25]. While much work has taken place on both groups of proposals, there have been few unambiguous signs of topological superconductivity observed experimentally. In this endeavor, the most promising experimental signatures have come from the second class of proposals, in particular the spin-orbit coupled semiconductors[37, 35, 27] and magnetic adatoms proximity-coupled with *s*-wave superconductors[36, 28]. Nonetheless, it is clear that within each of the proposals to observe topological superconductivity, there is a trend in the components required to produce the unconventional superconductivity: non-zero Berry curvature induced by spin-orbit coupling and broken time reversal symmetry by magnetism.

[1] Portions of this study were previously published as [1] and reprinted with permission (Copyright 2016 by American Physical Society).

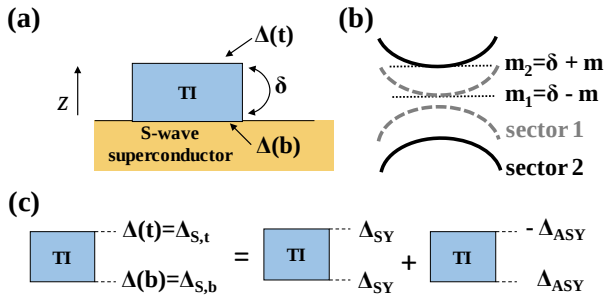

Figure 2.1: (a) A schematic of system under consideration. The ultrathin TI is grown on top of the s-wave superconductor, whose hybridization gap is described as δ. The induced order parameter at top (bottom) surface is indicated as $\Delta(t)$ ($\Delta(b)$). (b) After we apply the proper rotation to the system, we obtain two decoupled systems in hybridization basis of the top and bottom surfaces. Two individual sectors are referred as to a sector 1 and sector 2. (c) Total induced superconducting order parameter is equivalent to a combination of (spatially) symmetric and anti-symmetric superconducting order parameter.

Of the available platforms within which one may combine these ingredients, one of the well known routes to generate topological superconductivity is via the superconducting proximity effect in a heterostructure sample of a conventional s-wave superconductor and 3D TRI TI[25]. In the pioneering work of Fu and Kane, Cooper pairs from s-wave superconductors that are proximity-coupled to 3D TRI TI tunnel from the superconductor into the TI resulting in the acquisition of an topological superconductivity that behaves an effective spinless, chiral $p_x + ip_y$ superconductor without breaking time-reversal symmetry. As compared to proposals using non-TI heterostructures[35, 36] or intrinsic superconductors[29, 30, 31, 32, 33, 34], the Fu-Kane proposal is attractive as it does not require further assumptions on any of the physical parameters such as Cooper pairing amplitudes between different orbitals[38] or the position of the chemical potential[33, 39]. To facilitate the generation of chiral edge states, a Zeeman field may be introduced to open a gap in the energy spectrum and thereby form a boundary at the surface of the TI[25]. To this end, topological insulators with magnetic dopants that break time-reversal symmetry are of great interest[40, 41, 42, 43, 44, 45] as a platform to observe topological superconductivity and chiral edge states. In this work, we study how introducing magnetic dopants affects the proximity induced superconductivity of the 3D TI system. We consider magnetically ordered dopants through the addition of a uniform Zeeman splitting term in a thin 3D TRI TI sample such as Bi_2Se_3 to form a magnetic domain via the net exchange field[43, 44]. As experimental TI samples must be thin for superconductivity to be observed on the surface, we focus on the "ultrathin" limit of the TI where the surface states are not well-isolated but hybridized resulting in a gapped surface state spectrum.

We seek to understand the physics of magnetically-doped, ultrathin TI and its topological phase by analyzing the superconducting order parameter using both analytical and numerical techniques. In Section

2.2, we introduce a 2D continuum model for the surface states of an ultrathin TI that accounts for the hybridization gap. By applying a series of unitary transformations, we note that the model can be separated into independent sectors, whose relevant pairing potential have a symmetric and anti-symmetric spatial form when superconductivity is added. We then analyze the symmetric and anti-symmetric s-wave pairing potential at the phenomenological level by assuming a constant induced order parameter, and find that anti-symmetric pairing is dominant for experimentally relevant strengths of the Zeeman field. Simplifying the Hamiltonian with assumed anti-symmetric pairing potential, we find that gap closing points exist and are controlled by three parameters that can be tuned in experiment: the chemical potential, hybridization gap, and Zeeman energy. As our system is in D class within the Altland-Zirnbauer classification, it is characterized by a $\mathbb{Z}$ topological invariant[23]. Thus we analyze the gap closing points and corresponding topological phase by evaluating the Chern number to obtain the resulting phase diagram. In Section 2.3, we model a more realistic lattice system by self-consistently solving for the superconducting order parameter in a heterostructure of a s-wave superconductor coupled to a TI using the Bogoliubov-de Gennes (BdG) formalism. Our numerical simulation accurately captures the effects of bulk and surface bands that are present in TI and includes the spin dynamics of these bands when magnetism is introduced. An induced superconducting order parameter obtained from bulk states of the TI shows a rapid decay in magnitude with increasing magnetic impurity concentration as the Zeeman energy splits the band and suppresses the s-wave pairing. In contrast, the surface states show an induced order parameter that persists over an experimentally relevant range of the Zeeman energy due to their spin-momentum locked nature and non-zero projection of electron pairs into the s-wave pairing component. Moreover, self-consistent calculation shows that the anti-symmetric pairing potential is dominant at non-zero Zeeman energy, thereby, we confirm our phenomenological analysis.

2.2 Proximity induced superconductivity in the surface ultra-thin TI

2.2.1 Surface state model for ultra-thin TI

Fig. 2.1(a) shows the schematic figure of the system under consideration, in which a ultra-thin TI and s-wave superconducting metal is proximity coupled each other. We start our discussion by writing down the

surface Hamiltonian of the ultra-thin TI, which is given as,

$$H_{TI} = \sum_{\mathbf{k}} \Psi^{\dagger}_{\mathbf{k}} [\begin{pmatrix} \hat{H}_{\text{top}} & \delta I_2 \\ \delta I_2 & \hat{H}_{\text{bot}} \end{pmatrix} - \mu] \Psi_{\mathbf{k}}, \tag{2.1}$$

where $\Psi_{\mathbf{k}} = [c_{t,\uparrow}(\mathbf{k}), c_{t,\downarrow}(\mathbf{k}), c_{b,\uparrow}(\mathbf{k}), c_{b,\downarrow}(\mathbf{k})]^T$. $c_{t,\uparrow}(\mathbf{k})$ ($c_{b,\downarrow}(\mathbf{k})$) is electron annihilation operator at top (bottom) surface with up (down) spin states at momentum $\mathbf{k} = (k_x, k_y)$. σ_i is i-th Pauli matrices. I_2 is identity matrix. δ is the hybridization gap between the surface. We use $\hat{H}_{\text{top}} = -k_y\sigma_x + k_x\sigma_y$ and $\hat{H}_{\text{bot}} = k_y\sigma_x - k_x\sigma_y$ for the low energy description of top and bottom surface state Hamiltonians, respectively[46], to form a hybridized Hamiltonian that preserves time reversal symmetry. As the focus of this work is to understand the influence of magnetic dopants, we add the effect of a uniform perpendicular magnetization to the proximity-coupled TI surface via addition of the Zeeman energy splitting term within the Hamiltonian in Eq. (2.1). The Zeeman term whose principle axis is aligned in $\hat{z}$ takes the form $\hat{H}_{\text{Zeeman}} = (m_z) I_2 \otimes \sigma_z$, where $m_z\sigma_z$ is the energetic splitting of spin states due to the magnetization arising from the dopants included within the TI film, and the identity matrix acts on top and bottom surface (or pseudospin) degree of freedom. Previous work considering the effects of magnetic dopants on the surface physics of TRI TI indicates that the addition of magnetically ordered impurities allows for the development of a net ferromagnetic order,[47, 48, 49] and thus a uniform magnetization can provide a simple but accurate picture of the TI with magnetic dopants. Within this work, we ignore any orbital effects as those resulting from magnetic dopants are negligible[50].

Including the Zeeman term, we may write Eq. (2.1) in 4×4 matrix form as

$$\hat{H}_{\text{surf}}(\mathbf{k}) = \hat{H}_{\text{TI}}(\mathbf{k}) + \hat{H}_{\text{Zeeman}} = \begin{pmatrix} m_z - \mu & -k_y - ik_x & \delta & 0 \\ -k_y + ik_x & -m_z - \mu & 0 & \delta \\ \delta & 0 & m_z - \mu & k_y + ik_x \\ 0 & \delta & k_y - ik_x & -m_z - \mu \end{pmatrix}. \tag{2.2}$$

Eq. (2.2) is further simplified by applying proper rotational matrices. Without loss of generality, we remove k_y by applying an $SU(2)$ rotation, $U_1 = I_2 \otimes e^{i\theta_1\sigma_z}$, where $\theta_1 = -\tan^{-1}(k_x/k_y)/2$. In addition, we apply another $SU(2)$ rotation on the pseudo-spin degree of freedom (top/bottom layer), $U_2 = e^{i\frac{\pi}{4}\tau_y} \otimes I_2$, where τ_y is the Pauli matrix for the pseudospin degree of freedom, and rewrite the Hamiltonian in Eq. (2.2) using a hybridized basis of top and bottom layer. The resultant Hamiltonian is

$$\hat{H}'_{\text{surf}}(k) = U_2 U_1 \hat{H}_{\text{surf}}(k_x, k_y) U_1^{\dagger} U_2^{\dagger}. \tag{2.3}$$

We may write Eq. (2.3) in 4×4 matrix form:

$$\hat{H}'_{\text{surf}}(k) = \begin{pmatrix} m_2 - \mu & 0 & 0 & -k \\ 0 & m_1 - \mu & -k & 0 \\ 0 & -k & -m_1 - \mu & 0 \\ -k & 0 & 0 & -m_2 - \mu \end{pmatrix}, \tag{2.4}$$

where $k = |\mathbf{k}|$. In Eq. (2.4), we define effective Zeeman energy $m_1 = \delta - m_z$ and $m_2 = \delta + m_z$. Note that the Hamiltonian Eq. (2.4) is now decoupled into two sectors:

$$\hat{H}'_{\text{surf},1}(k) = m_1\tau_z - k\tau_x - \mu, \hat{H}'_{\text{surf},2}(k) = m_2\tau_z - k\tau_x - \mu, \tag{2.5}$$

where $\tau_{x,y,z}$ is the Pauli matrix in pseudospin space whose basis is now in linear combination of spin and layer degree of freedoms. For the following arguments, $\hat{H}_{\text{surf},1}$ and $\hat{H}_{\text{surf},2}$ refers to the Hamiltonian in sector 1 and sector 2, respectively, as shown in Fig. 2.1 (b). The rotated basis for Eq. (2.3) is

$$U_2 \begin{pmatrix} c_{t,\uparrow} \\ c_{t,\downarrow} \\ c_{b,\uparrow} \\ c_{b,\downarrow} \end{pmatrix} = \frac{1}{\sqrt{2}} \begin{pmatrix} c_{t,\uparrow} + c_{b,\uparrow} \\ c_{t,\downarrow} + c_{b,\downarrow} \\ -c_{t,\uparrow} + c_{b,\uparrow} \\ -c_{t,\downarrow} + c_{b,\downarrow} \end{pmatrix} = \begin{pmatrix} \nu_{2,\uparrow} \\ \nu_{1,\downarrow} \\ \nu_{1,\uparrow} \\ \nu_{2,\downarrow} \end{pmatrix}, \tag{2.6}$$

where we omit in-plane momentum index $\mathbf{k}$ for simplicity. Eq. (2.6) shows that the electron states at top and bottom surface form bonding and anti-bonding like hybridized states, whose annihilation operator is defined by ν. Due to the opposite helicity of top and bottom surfaces, the hybridized basis satisfies following unitary transformation

$$(\tau_x \otimes \sigma_z)^\dagger \hat{H}_{\text{surf}}(\tau_x \otimes \sigma_z) = \hat{H}_{\text{surf}}, \tag{2.7}$$

which exchanges the particles at top and bottom surfaces, namely, $c_{t,\uparrow} \to c_{b,\uparrow}$ and $c_{t,\downarrow} \to -c_{b,\downarrow}$. Consequently, a band having a basis of $\nu_{1,\downarrow} = (c_{t,\downarrow} + c_{b,\downarrow})/\sqrt{2}$ has $\nu_{1,\uparrow} = (-c_{t,\uparrow} + c_{b,\uparrow})/\sqrt{2}$ as another basis to satisfy Eq. (2.7) and this particular combination of basis forms the bands in sector 1. The other set of basis states forms the bands in sector 2. Having two well separated sectors in our Hamiltonian, we may analyze possible superconductor pairing order parameters.

2.2.2 Symmetric and anti-symmetric superconducting order parameter

When a surface state is coupled to a superconducting system, one may observe an induced superconducting order parameter in the surface states of the TI as Cooper pairs tunnel from the superconductor system[51]. In our system, the induced order parameters in the top and bottom surface differ in their magnitude as the Cooper pair tunneling probability decays as a function of a spatial separation from the interface between TI and s-wave superconductor to the other surface of the TI[52]. Due to this gradient in order parameter magnitude, we may decompose the induced order parameter into two distinct components, whose individual $U(1)$ phases are symmetric and anti-symmetric in $\hat{z}$ direction. Fig. 2.1(c) shows the simplest example, e.g. $\Delta(z) = \Delta_{SY}(z) + \Delta_{ASY}(z)$ where $\Delta_{SY}(t) = \Delta_{SY}(b)$ and $\Delta_{ASY}(t) = -\Delta_{ASY}(b)$.

Having the basis representation in Eq. (2.6), we may examine the induced pair correlation function defined within each of the sectors or across different sectors. A pair correlation function of the intra-band s-wave pairing (within sector 1 or sector 2) is, for example,

$$F_{\text{intra}} = \langle v_{1,\uparrow} v_{1,\downarrow} \rangle = \frac{1}{2} \langle (-c_{t,\uparrow} + c_{b,\uparrow})(c_{t,\downarrow} + c_{b,\downarrow}) \rangle, \tag{2.8}$$

where we suppress the in-plane momentum index $\mathbf{k}$ for brevity. Eq. (2.8) shows an odd parity under the exchange of the layer degree of freedom, or, $F_{\text{intra}} \xrightarrow{t \leftrightarrow b} -F_{\text{intra}}$. By defining the on-site s-wave order parameter[53] as $\Delta_{\text{intra}} = \sum_{\mathbf{k}} F_{\text{intra}}(\mathbf{k})$, we find that the intra-band s-wave order parameter is anti-symmetric in the $\hat{z}$ direction. Meanwhile, a pair correlation function of the inter-band s-wave pairing (between sector 1 and sector 2) is, for example,

$$F_{\text{inter}} = \langle v_{1,\uparrow} v_{2,\downarrow} \rangle = \frac{1}{2} \langle (-c_{t,\uparrow} + c_{b,\uparrow})(-c_{t,\downarrow} + c_{b,\downarrow}) \rangle, \tag{2.9}$$

which shows an even parity under the exchange of the layer degree of freedom, or, $F_{\text{inter}} \xrightarrow{t \leftrightarrow b} +F_{\text{inter}}$ and, thus, the resultant inter-band s-wave order parameter, $\Delta_{\text{inter}} = \sum_{\mathbf{k}} F_{\text{inter}}(\mathbf{k})$, is symmetric in $\hat{z}$ direction. Therefore, Eq. (2.8) shows that the anti-symmetric order parameter is responsible for superconducting pairing that occurs within the same sectors, whereas Eq. (2.9) shows that the symmetric order parameter results in superconducting pairing across different sectors.

The above argument is explicitly shown by constructing the Bogoliubov-de Gennes (BdG) Hamiltonian. We add an induced order parameter to the system as a constant value, Δ, at the phenomenological level[25].

Then the BdG Hamiltonian is

$$\hat{H}_{\mathrm{BdG}}(\mathbf{k}) = \begin{pmatrix} \hat{H}_{\mathrm{surf}}(\mathbf{k}) & \hat{H}_{\mathrm{BCS}} \\ \hat{H}^{\dagger}_{\mathrm{BCS}} & -\hat{H}^{*}_{\mathrm{surf}}(-\mathbf{k}) \end{pmatrix}, \tag{2.10}$$

where the s-wave pairing Hamiltonian is

$$\hat{H}_{\mathrm{BCS}} = \begin{pmatrix} \Delta_t & 0 \\ 0 & \Delta_b \end{pmatrix} \otimes i\sigma_y, \tag{2.11}$$

where Δ_t and Δ_b are the s-wave order parameter at top and bottom surface, respectively. We then decompose the order parameter in Eq. (2.11) into two components, namely, the symmetric and anti-symmetric components. Fig. 2.1(c) depicts symmetric and anti-symmetric components of superconducting order parameter written as

$$\hat{H}_{\mathrm{BCS,SY}} = \begin{pmatrix} \Delta_{SY} & 0 \\ 0 & \Delta_{SY} \end{pmatrix} \otimes i\sigma_y, \tag{2.12}$$

$$\hat{H}_{\mathrm{BCS,ASY}} = \begin{pmatrix} -\Delta_{ASY} & 0 \\ 0 & \Delta_{ASY} \end{pmatrix} \otimes i\sigma_y, \tag{2.13}$$

respectively, where Δ_{SY} and Δ_{ASY} are corresponding decomposed order parameters. By defining $\bar{U}_{1,2} = \begin{pmatrix} U_{1,2} & 0 \\ 0 & U^{*}_{1,2} \end{pmatrix}$, we obtain a simplified Hamiltonian in BdG form,

$$\hat{H}'_{\mathrm{BdG}}(k) = \bar{U}_2\bar{U}_1\hat{H}_{\mathrm{BdG}}(\mathbf{k})\bar{U}_1^{\dagger}\bar{U}_2^{\dagger} = \begin{pmatrix} \hat{H}'_{\mathrm{surf}}(k) & \hat{H}'_{\mathrm{BCS,SY}} + \hat{H}'_{\mathrm{BCS,ASY}} \\ h.c. & -\hat{H}'_{\mathrm{surf}}(-k) \end{pmatrix}, \tag{2.14}$$

where the symmetric and anti-symmetric component of pairing Hamiltonian becomes

$$\hat{H}'_{\mathrm{BCS,SY}} = \begin{pmatrix} 0 & \Delta_{SY} & 0 & 0 \\ -\Delta_{SY} & 0 & 0 & 0 \\ 0 & 0 & 0 & \Delta_{SY} \\ 0 & 0 & -\Delta_{SY} & 0 \end{pmatrix}, \tag{2.15}$$

and

$$\hat{H}'_{\mathrm{BCS,ASY}} = \begin{pmatrix} 0 & 0 & 0 & \Delta_{ASY} \\ 0 & 0 & -\Delta_{ASY} & 0 \\ 0 & \Delta_{ASY} & 0 & 0 \\ -\Delta_{ASY} & 0 & 0 & 0 \end{pmatrix}, \tag{2.16}$$

respectively. The pairing Hamiltonian in Eq. (2.15) explicitly shows that an electron (hole) band in sector 1 is coupled with the hole (electron) band in sector 2, which we refer to as an inter-band pairing. Likewise, Eq. (2.16) shows that the anti-symmetric superconducting order parameter couples electron bands and hole bands in the same sector, which we refer to as intra-band pairing.

2.2.3 Symmetric and anti-symmetric superconducting order parameter at non-zero Zeeman energy

Although the hybridized surface state bands are initially degenerate having both the symmetric and anti-symmetric superconducting pairing, introducing the Zeeman term splits them in energy and changes their relative contributions to the resultant superconductivity. In order to gain insight on the superconducting order parameter evolution as a function of the Zeeman energy, we examine pair correlation function of the TI surface states. We start with the BdG Hamiltonian defined by

$$\tilde{H}_{TI+SC} = \begin{pmatrix} \tilde{H}_{top} & \tilde{\delta} & 0 \\ \tilde{\delta}^{\dagger} & \tilde{H}_{bot} & \tilde{t}_c \\ 0 & \tilde{t}_c^{\dagger} & \tilde{H}_{SC} \end{pmatrix}, \tag{2.17}$$

where $\tilde{H}_{top}$, $\tilde{H}_{bot}$ are top and bottom surface TI Hamiltonian in BdG form, respectively. The top and bottom surface are connected by the hopping matrix $\tilde{\delta}$, $\tilde{H}_{SC}$ is s-wave superconductor Hamiltonian connected to the bottom surface of the TI by the hopping matrix $\tilde{t}_c$. The form of the hopping matrices $\tilde{\delta}$ and $\tilde{t}_c$ are general and their specific definition is dependent on specific basis chosen. Then Eq. (2.17) satisfies $(\hat{H}_{TI+SC} - \epsilon)\Psi_{TI+SC}(\mathbf{r}) = 0$, where $\Psi_{TI+SC}(\mathbf{r})$ is the wavefunction at $\mathbf{r} = (x, y)$ and energy ϵ. By integrating out the superconductor degree of freedom, and assuming that tunneling from s-wave superconductor to bottom surface of the TI is local in space[54], we now have

$$\tilde{H}_{TI} = \begin{pmatrix} \tilde{H}_{top} & \tilde{\delta} \\ \tilde{\delta}^{\dagger} & \tilde{H}_{bot} + \tilde{\Sigma}_{SC} \end{pmatrix}, \tag{2.18}$$

which satisfies $(\tilde{H}_{TI} - \omega)\Psi_{TI}(\mathbf{r}) = 0$ where $\Psi_{TI}(\mathbf{r})$ is the wavefunction of TI system. In Eq. (2.18), the proximity-induced superconductivity comes into play through the s-wave superconductor self-energy term, $\tilde{\Sigma}_{SC} = -\tilde{\delta}\tilde{G}_{SC}\tilde{\delta}^{\dagger}$, where $\tilde{G}_{SC} = (\tilde{H}_{SC} - \epsilon)^{-1}$ is the superconductor Green's function. Specifically, we only consider the off-diagonal part (or the anomalous part of the Green's function) of the self-energy term to elucidate qualitative behavior of the pair correlation function. By adopting the energy independent self-energy term near $\epsilon \sim 0$, we find a simple expression,[54] $\tilde{\Sigma}_{SC} = \Delta_0 i\sigma_y$, for the s-wave superconductor self-energy term.

To utilize our analysis in section 2.2.1 and 2.2.2, we adopt the low energy description of the ultrathin TI surface states Hamiltonian in Eq. (2.2) and its BdG form in Eq. (2.10). We set order parameter in Eq. (2.11) as $\Delta_t = 0$ and $\Delta_b = \Delta_0$ following the discussion in Eq. (2.18). Then we evaluate the top (t) and bottom (b) surface on-site s-wave pair correlation function,

$$F_{t/b} = \sum_{\mathbf{r}} \langle c_{t/b,\uparrow}(\mathbf{r}) c_{t/b,\downarrow}(\mathbf{r}) - c_{t/b,\downarrow}(\mathbf{r}) c_{t/b,\uparrow}(\mathbf{r}) \rangle = \sum_{\mathbf{k}} [F^{\uparrow\downarrow}_{t/b}(\mathbf{k}) - F^{\downarrow\uparrow}_{t/b}(\mathbf{k})], \tag{2.19}$$

which explicitly captures the superconducting proximity effect[55]. In Eq. (2.19), we define momentum space resolved correlation function, $F^{\uparrow\downarrow}_{t/b}(\mathbf{k}) = \langle c_{t/b,\uparrow}(\mathbf{k}) c_{t/b,\downarrow}(-\mathbf{k}) \rangle$. For detailed calculation for the correlation function, see Appendix A.1. In this work, we are interested in the coupled system where the surface states of the TI and metallic states in superconductor are not strongly mixed, which is a valid regime for realistic proximity-coupled TI systems[52]. Then we may assume that the host superconductor's order parameter is unaffected by the TI and, as a result, we compute the pair correlation function $F_{t/b}$ without considering self-consistency. We now examine spatial distribution of the order parameter by defining the symmetric and anti-symmetric pair correlation functions,

$$F_{SY} = (F_b + F_t)/2, \quad F_{ASY} = (F_b - F_t)/2. \tag{2.20}$$

In Fig. 2.2, we show the symmetric and anti-symmetric pair correlation function F_{SY} and F_{ASY} as a function of the Zeeman energy. Although, based on Fig. 2.2, we may conclude that the symmetric pairing potential determines the system order parameter at the zero or low Zeeman energy, the pair correlation function becomes dominantly anti-symmetric as we increase the Zeeman energy. This particular transition may be understood in terms of the inter-band and intra-band pairings described in Eq. (2.15) and (2.16), which are governed by the symmetric and anti-symmetric pairing potential, respectively.

Inter-band pairing: The ultrathin TI system is described by two decoupled subspaces, namely, sector 1 and sector 2, as shown in Eq. (2.4) in hybridized basis. The non-zero Zeeman energy splits sector 1 and

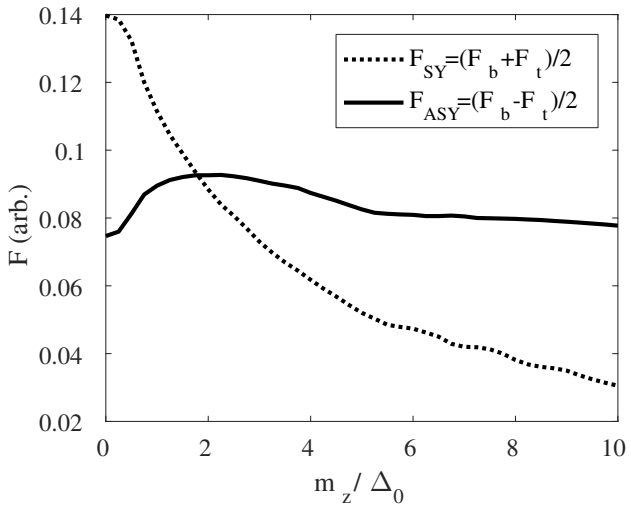

Figure 2.2: Symmetric and anti-symmetric pair correlation function of the top and bottom surfaces of the TI. The hybridization gap of the system is set to $\delta = 0.5$ eV. We set the chemical potential of TI $\mu/\delta = 1.5$, whose location crosses the hybridized surface band. We set $\Delta_0/\delta = 0.1$, and cut-off energy is set to be $|E_c/\delta| = 1.0$. Adapted from [1].

sector 2 in energy and, for example, electron states at Fermi wavevector $\mathbf{k}_F$ in sector 1 no longer has a pair at $-\mathbf{k}_F$ in sector 2. Consequently, the Cooper pairs formed by the inter-band pairing experience a Fermi surface mismatch as the Zeeman energy splits the bands in energy. Further increase in the Zeeman energy results in a larger mismatch in Fermi surface that costs more energy to form Cooper pairs reducing the number of pairing states. Although we may not see such phase transition in proximity coupled system, BCS formalism captures this Fermi surface mismatch. As a result of the Fermi surface mismatch, Fig. 2.2 shows a rapid decrease of the symmetric pair correlation function (dashed line).

Intra-band pairing: In the absence of the Zeeman energy, one can observe s-wave electron pairing within each band due to the spin-momentum locked nature of the surface states. In the presence of the Zeeman field, however, the TI surface states exhibit canted "hedgehog" spin texture[44] and, consequently, the projected s-wave pairing magnitude decreases due to the out-of-plane canting induced by the Zeeman field. However, each band still possesses non-zero s-wave pairing as the paired electrons experience no Fermi surface mismatch, unlike those in the inter-band pairing case. As a result, Fig. 2.2 shows the anti-symmetric pair correlation function (solid line) persisting with increasing Zeeman field.

The above analysis shows that the anti-symmetric pairing potential is the dominant factor to form induced superconductivity for Zeeman energies whose scale is larger than the zero-field superconducting gap. This is the experimentally relevant regime considering that the typical superconducting gap is few meV for 4-quintuple-layer Bi_2Se_3[52] while the Zeeman energy may be as large as ~ 50 meV in 2.5% Mn doped Bi_2Se_3[44] system. In this regard, the anti-symmetric pairing potential is more relevant than the symmetric

one for magnetically-doped ultrathin TI system.

2.2.4 Topologically non-trivial phases in ultrathin TI

Our analysis in Section 2.2.2 shows that the anti-symmetric pairing potential plays a major role in superconductivity in the magnetically-doped ultrathin TI system when the induced Zeeman energy is larger than the zero-field induced superconducting gap. Taking advantage of the property of the anti-symmetric pairing potential discussed in Eq. (2.16), the BdG Hamiltonian in Eq. (2.14) is now decoupled into two independent sectors. With the reduced BdG Hamiltonian, we now obtain the analytic form of the quasi-particle spectrum and use the gap closing points to identify topologically non-trivial phases.

From Eqs. (2.4, 2.14, 2.16), we obtain a block diagonal form of the BdG Hamiltonian, which we rewrite as two decoupled BdG Hamiltonian for sector 1 and sector 2,

$$\hat{H}'_{\mathrm{BdG,i}} = \begin{pmatrix} \hat{H}'_{\mathrm{surf,i}}(k) & -\Delta_0 i\tau_y \\ -(\Delta_0 i\tau_y)^\dagger & -\hat{H}'^{*}_{\mathrm{surf,i}}(-k) \end{pmatrix}. \tag{2.21}$$

In Eq. (2.21), τ_y is the Pauli matrix whose representation is in the hybridized basis shown in Eq. (2.6), and $\hat{H}'_{\mathrm{surf,i}}(k)$ is the sector $i = (1, 2)$ Hamiltonian in Eq. (2.5). From this, we obtain the quasi-particle spectrum

$$E_i(k) = \pm\sqrt{k^2 + m_i^2 + \Delta_0^2 + \mu^2 \pm 2\sqrt{m_i^2\Delta_0^2 + k^2\mu^2 + m_i^2\mu^2}}, \tag{2.22}$$

where $m_1 = \delta - m_z$ and $m_2 = \delta + m_z$ is the effective magnetic field defined in Eq. (2.4) for each of the sectors. For non-zero Δ_0, we find that a gap closing occurs only at $k = 0$ when $|m_i| = \sqrt{\Delta_0^2 + \mu^2}$. The system undergoes a phase transition at the identified gap closing point[56] with the Zeeman energy $m_z = \delta + \sqrt{\Delta_0^2 + \mu^2}$ and, therefore, the gap closing point is determined by the system parameters: the hybridization gap (δ), the position of the chemical potential (μ), and the induced superconducting gap (Δ_0). As a topological classification of our system is in D class[23], the relevant phase is classified by the $\mathbb{Z}$ topological invariant. In this regard, we numerically evaluate the Chern number by varying the chemical potential and Zeeman energy, whose values are normalized by the hybridization gap.

Prior to our analysis on the system Chern number, we first define a lattice regularized model for the top surface Hamiltonian[46]

$$\hat{H}^{\mathrm{latt}}_{\mathrm{top}} = (\hbar v_F/a)[-\sin(k_y a)\sigma_x + \sin(k_x a)\sigma_y] + (D/a^2)[2 - \cos(k_x a) - \cos(k_y a)]\sigma_z, \tag{2.23}$$

and bottom surface Hamiltonian is $\hat{H}^{\text{latt}}_{\text{bot}} = -\hat{H}^{\text{latt}}_{\text{top}}$, where a is a lattice constant, v_F is the Fermi velocity, D is a parameter that controls the quadratic term at higher energy. Without loss of generality, we set $a = 1$ and $\hbar v_F = D = 1$. The second line of the Eq. (2.23) gaps out the extra Dirac points at $(0, \pi)$, $(\pi, 0)$, (π, π). Although this term breaks time-reversal symmetry, the system under consideration has broken time-reversal symmetry due to the magnetic dopants. Therefore, Eq. (2.23) correctly captures relevant low energy physics in our system. Using the Eqs. (2.10, 2.23), we construct the BdG Hamiltonian to obtain eigenstates of the nth band to calculate corresponding Chern number[57], $\tilde{c}_n$. For calculation details of the Chern number, see Appendix A.2. Finally, the total Chern number of the system is obtained using $\tilde{c} = \sum_n \tilde{c}_n$, where n runs over all of the occupied bands.

We return to the discussion below Eq. (2.21) to examine the Chern number of the BdG Hamiltonian for the sector 1 with the assumed anti-symmetric pairing potential. Assuming the hybridization gap satisfies $\delta > \sqrt{\Delta_0^2 + \mu^2}$, the proximity coupled ultrathin TI system is initially gapped and in the trivial regime for $m_z < \delta - \sqrt{\Delta_0^2 + \mu^2}$. As we increase the magnetic dopant concentration and, as a result, the Zeeman energy m_z, the Chern number of the system becomes -1 after the first gap closing point at $m_z = \delta - \sqrt{\Delta_0^2 + \mu^2}$ and becomes -2 after the second gap closing point at $m_z = \delta + \sqrt{\Delta_0^2 + \mu^2}$. Other gap closing points exist at $\mathbf{k} = (\pi, 0)$ and $(0, \pi)$ for $|m_z - \delta| = 2D/a^2 \pm \sqrt{\Delta_0^2 + \mu^2}$ and at $\mathbf{k} = (\pi, \pi)$ for $|m_z - \delta| = 4D/a^2 \pm \sqrt{\Delta_0^2 + \mu^2}$. As a result, the Chern number becomes 0 in the large m_z limit. However, we only consider low-energy physics in this work, thus we only consider the gap closing point at $\mathbf{k} = (0, 0)$. A similar analysis may be applied for $m < 0$ using the Hamiltonian in sector 2. In fact, the Hamiltonian in Eq. (2.21) is analogous to the surface states of the TI system proximity coupled with the domain of the s-wave superconductor and ferromagnet (3D TI-SC-FM)[25, 58, 59]. The analogy is made evident by taking the limit of $\delta \to 0$, where the corresponding gap closing point converges to that of the 3D TI-SC-FM system. For example, by setting $\mu = 0$, the gap closing points are at $m_z = \delta \pm \sqrt{\Delta_o^2 + \mu^2} \to \pm\Delta_0$, which coincide with the phase transition points of the 3D TI-SC-FM system[59].

To obtain a generic phase diagram, we assume that both the symmetric and anti-symmetric pairing potential are present. Specifically, we assume that the magnitude of the induced superconducting gap satisfies the experimentally relevant regime for the ultrathin TI system[52], namely, $\Delta_0 \ll \delta$. In this regime, the specific form of the pairing potential is insignificant as we construct the phase diagram with other parameters relative to δ. Thus, we set the pairing Hamiltonian to satisfy $\Delta_t = 0$, $\Delta_b = \Delta_0$. Then we compute the Chern number and construct the phase diagram of the ultrathin TI in Fig. 2.3 by varying the chemical potential, μ, and the Zeeman energy, m_z, normalized by the hybridization gap, δ. Each region in the phase diagram is illustrated by a schematic of the surface state band diagram in a normal phase TI with

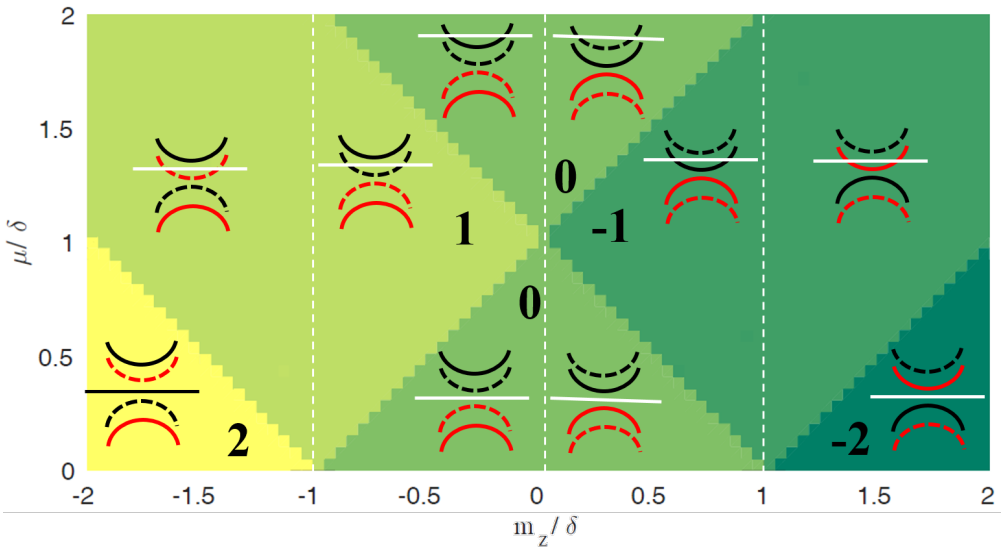

Figure 2.3: The phase diagram and corresponding Chern number of an ultrathin TI as a function of the chemical potential, μ, and the Zeeman energy m. Both axises are normalized by the hybridization gap, δ. For illustration purposes, we draw schematics that describe the motion of the surface state bands in different sectors and the corresponding Chern numbers. Note that solid curve (dashed curve) represents surface state band in sector 1 (sector 2), and black (red) color represents conduction (valence) band when $m = 0$. The horizontal line in each band diagram corresponds to the position of the chemical potential. The s-wave order parameter at top and bottom surface is $\Delta_0 = 0$ and 0.01δ, respectively. Adapted from [1].

a specified location of the chemical potential. Specifically, solid and dashed curves are the bands in sector 1 and sector 2, respectively, and the horizontal line indicates a location of the chemical potential. Note that the normal phase of the ultrathin TI undergoes the quantum phase transition[60] at $|m_z| = \delta$ due to the crossing of the conduction and valance band, which are initially separated by the hybridization gap. In order to capture this quantum phase transition point in our schematics, the initial valence and conduction bands at $m_z = 0$ are indicated by red and black color, respectively. To illustrate the system behavior in more detail, we follow, for example, the $\mu/\delta = 0.8$ cut in Fig. 2.3. At $m_z/\delta = 0$, the chemical potential is located within the hybridization gap and the system is in trivial phase (the Chern number is 0). As we increase the Zeeman energy, the conduction band is shifted and touches the chemical potential at $k = 0$, which corresponds to a gap closing point in the quasi-particle spectrum of BdG Hamiltonian. Then, the band acquires a non-trivial Chern number of -1. Note that the valence band and conduction band are shifted further due to the Zeeman energy until they touch at $m_z/\delta = 1$. However, this particular band crossing of the conduction and valence band has no effect on the Chern number, as there is no gap closing in quasi-particle spectrum of the BdG Hamiltonian. Once the Zeeman energy passes the second gap closing point, the additional band crossing at the chemical potential results in a Chern number of -2. Therefore, it is important to place the relevant parameters such as chemical potential and Zeeman energy in the right position to observe the topological

superconductivity in the system. Further increase in Zeeman energy, m_z, will result in a gap closing at other high symmetry points, such as $\mathbf{k} = (\pi, 0)$ and (π, π), which eventually results in the Chern number becoming 0 in the $|m_z| \to \infty$ limit. However, this is not important as we present the phase diagram within the experimentally relevant region where the Zeeman energy of the magnetic dopants is comparable to the hybridization gap.

The physics of the non-trivial phase in the system may be further described by mapping our system to one of the well known topological superconducting systems. The Hamiltonian in Eq. (2.21) has a close analogy to the surface states of the 3D TI (for example, a top surface) proximity coupled to the interface of a ferromagnet and s-wave superconductor[59, 25, 58], where one may find chiral Majorana edge modes at the domain wall of the ferromagnet and superconductor region. Likewise, by properly choosing the concentration of the magnetic dopants and chemical potential of the ultrathin TI, we may also find the chiral edge states at the domain wall of the magnetically doped and undoped region of our system.

2.3 Induced superconductivity of ultra-thin TI beyond phenomenological level

Our motivation in this section is to examine the induced order parameter beyond the phenomenological model presented in Section 2.2. Instead of assuming the induced order parameter is a constant value, we examine the self consistently calculated induced order parameter by adopting a four band 3D TI model coupled to an s-wave superconductor.

2.3.1 Effective model for 3D TI

In Fig. 2.4, we show a schematic of the s-wave superconductor and 3D TI system that we consider in this work. In this heterostructure, we assume the presence of a non-zero attractive interaction, parametrized by the pairing strength V, within the superconducting layer and no explicit pairing strength within the TI film. We begin the construction of our model by first considering the non-superconducting Hamiltonian for our heterostructure including the contributions from both the superconductor and the TI. As we wish to accurately model spatially large structures, we write the in-plane directions ($\hat{x}$ and $\hat{y}$) within the momentum-space representation while we write the out-of-plane direction ($\hat{z}$) in real space. In order to maintain notational simplicity, $\mathbf{k}$ is used to represent the in-plane momentum $k_x\hat{x} + k_y\hat{y}$. The mixed-representation, or that which is composed of both real- and momentum-space components, non-superconducting, nearest-

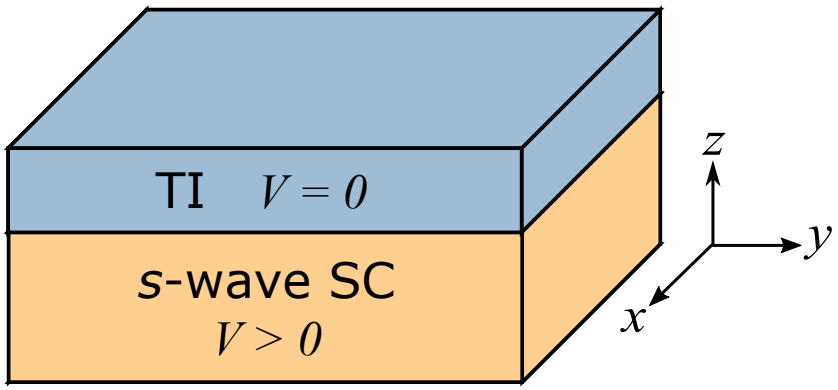

Figure 2.4: Schematic illustration of the s-wave superconductor–3D TI heterostructure that we consider in this work. In our 3D self-consistent simulation, we include a non-zero interaction strength within the s-wave superconductor, V, but, the interaction strength is initially set to zero in the TI as it contains no natural pairing. The self-consistent procedure to solve for the order parameter then allows for pairing amplitudes from the superconductor to enter the TI and induce superconductivity via the proximity effect. Adapted from [1].

neighbor-hopping Hamiltonian is

$$\mathcal{H} = \sum_{\mathbf{k},z} \left[\Psi^{\dagger}_{\mathbf{k},z} \left(\hat{H}_0(\mathbf{k}, z) \right) \Psi_{\mathbf{k},z} \; + \left(\Psi^{\dagger}_{\mathbf{k},z} \hat{H}_z \Psi_{\mathbf{k},z+\hat{z}} + \text{H.c.} \right) \right], \tag{2.24}$$

where the annihilation operator $\Psi_{\mathbf{k},z} = (c_{\mathbf{k},z,A\uparrow}\; c_{\mathbf{k},z,A\downarrow}\; c_{\mathbf{k},z,B\uparrow}\; c_{\mathbf{k},z,B\downarrow})^T$ is defined by a basis containing two orbitals (A, B) and two spin degrees of freedom ($\uparrow$, $\downarrow$). The TI Hamiltonian is represented by a minimal bulk model for 3D topological insulator which consists of two spin and two orbital bases[46, 61],

$$\hat{H}^{\text{latt}}_{\text{3D}}(\mathbf{k}) = M(\mathbf{k})\Gamma_0 + \sum_{i=x,y,z} d_i(\mathbf{k})\Gamma_i + m_z\Gamma_Z \tag{2.25}$$

with a momentum space lattice description of

$$d_i(\mathbf{k}) = (\hbar v_F/a)\sin(k_i a), M(\mathbf{k}) = (b/a^2)[\cos(k_x a) + \cos(k_y a) + \cos(k_z a)] - 3b/a^2 + \mathbb{M}, \tag{2.26}$$

where v_F is the Fermi velocity, a is a lattice constant, and b is a material parameter used to fit to a specific material band structure. In Eq. (2.26), $\mathbb{M}$ is a parameter that controls a topological phase of the system and the system is a trivial (topological) insulator when $\mathbb{M}/b < 0$ ($\mathbb{M}/b > 0$)[61]. The gamma matrices in Eq. (2.25) are defined as $\Gamma_{x,y,z} = \tau_x \otimes \sigma_{x,y,z}$ and $\Gamma_0 = \tau_z \otimes I_2$, where I_N are $N \times N$ identity matrices, σ_i and τ_i are the Pauli matrices for spin and orbital degrees of freedom, respectively. The Hamiltonian in Eq. (2.25) captures the low-energy characteristics of 3D TRI TIs with the A and B orbitals, for example, that

correspond to the linear combination of the p orbitals of Bi^{3+} and Se^{2-} of Bi_2Se_3, respectively[62, 46]. In addition, we introduce the Zeeman energy, m_z, with the corresponding gamma matrix $\Gamma_Z = I \otimes \sigma_z$ in the TI Hamiltonian to capture the magnetization arising from the magnetic dopants in the TI[46] . To model the s-wave superconductor-TI interface of our heterostructure, we represent the conventional superconductor portion of our heterostructure by a simple four-fold degenerate Hamiltonian

$$\hat{H}_{\mathrm{m}}^{\mathrm{latt}}(\mathbf{k}) = t_m[3 - \cos(k_x a) - \cos(k_y a) - \cos(k_z a)]I_4, \tag{2.27}$$

where t_m is the hopping parameter of the system. The metallic Hamiltonian in Eq. (2.27) describes a conventional s-wave superconductor, for example $NbSe_2$, in the normal phase. Without a loss of generality, we choose $a = b = 1$, $t_m = 1$, and $\hbar v_F = 1$ as our main focus of this work is a qualitative analysis on the order parameter rather than an analysis of an order parameter for a specific material. To examine the strong topological insulator regime, we set the mass parameter $\mathbb{M} = 0.35$[63].

In our model, we select the first 10 grid points within our solution space in the $\hat{z}$-direction to be the metal and the subsequent 4 points are chosen to be 3D TI in order to represent the possible experimental setup in Fig. 2.4. The disparate metal and TI models are incorporated into the full mixed-space Hamiltonian by making the following definitions for the matrices given in Eq. (2.24):

$$\hat{H}_0(\mathbf{k}, z) = \begin{cases} (3 - \cos k_x - \cos k_y)I_4 - \mu_m I_4 & , z \leq 10 \\ (\mathbb{M} - 3 + \cos k_x + \cos k_y)\Gamma_0 + \sin k_x \Gamma_x + \sin k_y \Gamma_y + m_z \Gamma_Z - \mu_{TI} I_4 & , 10 < z \leq 14 \end{cases} \tag{2.28}$$

$$\hat{H}_z = \begin{cases} (1/2)I_4 & z < 10 \\ (1/2)t_c I_4 & z = 10 \\ (1/2)\Gamma_0 + (i/2)\Gamma_z & 10 < z \leq 14, \end{cases} \tag{2.29}$$

where μ_m and μ_{TI} are the chemical potential of the metallic and TI system, respectively, and $0 \leq t_c \leq 1$ is a coupling constant that controls a coupling strength between the metallic and ultrathin TI system.

Unlike the isolated TI system, the presence of the metallic states modifies the surface states of the TI when the coupling constant, t_c, is introduced. To examine how this coupling modifies the surface states of the TI, we compute the momentum- and real-space resolved local density of states, $LDOS(\mathbf{k}, z)$, computed by the system Green's function[64] using Eqs. (2.28, 2.29). Figs. 2.5 (a, b, c) depict the $LDOS(\mathbf{k}, z)$ at the metallic surface, the bottom layer, and the top layer of the ultrathin TI system, respectively, when a coupling constant is $t_c = 0.8$. Due to the connecting hopping constant, $t_c \cdot t_m$, whose magnitude is comparable to that of the hopping constant in TI, the surface states of the TI exhibit strong imprint of the electronic states

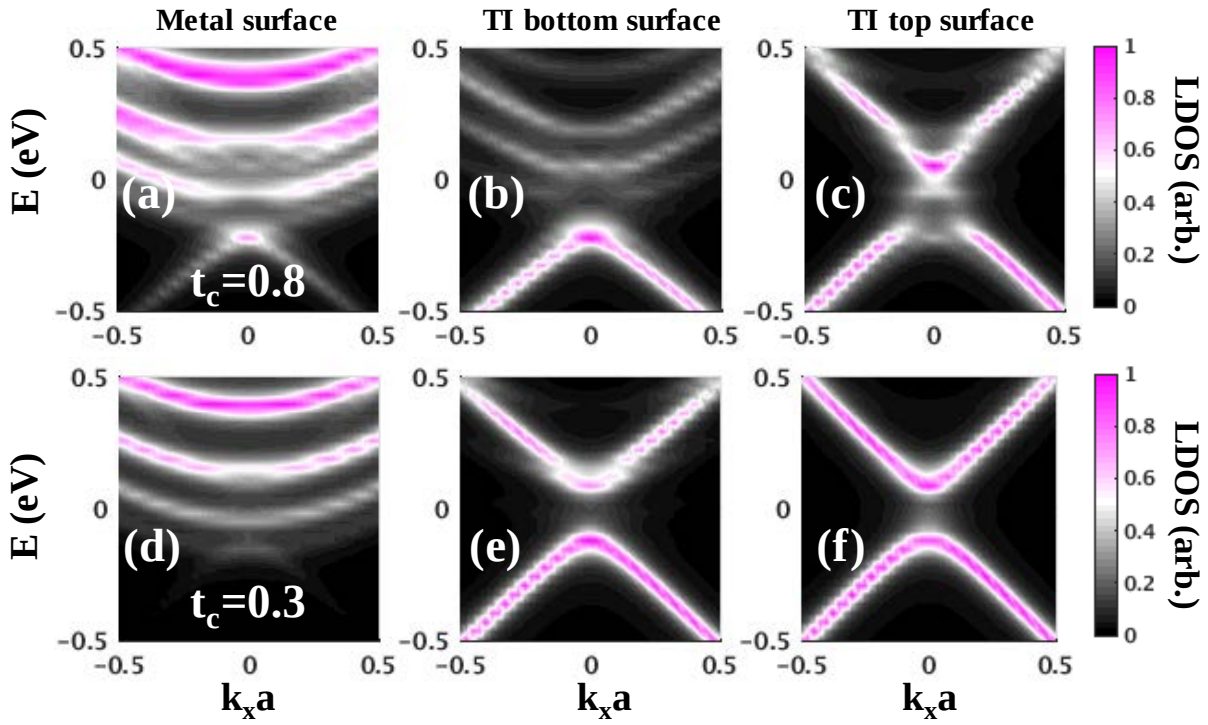

Figure 2.5: $LDOS(\mathbf{k}, z)$ is plotted at (a) the metallic surface ($z = 10$), (b) the bottom surface ($z = 11$), and (c) the top surface ($z = 14$) for $t_c = 0.8$ at $k_y = 0$. Similarly, $LDOS(\mathbf{k}, z)$ is plotted at (d) the metallic surface, (e) the bottom surface, and (f) the top surface for $t_c = 0.3$. The obtained $LDOS$ is normalized by its maximum magnitude at each layer. Adapted from [1].

from the metallic states and, as a result, the top surface of the TI shows a reduced hybridization gap. In addition, charge accumulation at the interface may occur and cause a structural inversion asymmetry (SIA) potential, which further modifies the surface states band structure of TI[65]. Such substrate effect and the resultant discrepancy of the band structure from that of the ideal ultrathin TI surface states are observed in, for example, Bi_2Se_3 system grown on Si(111) substrate[66]. In this work, we focus on the moderate to weak coupling regime where the generic band structure of the TI system is minimally affected by the metallic system and we may exclude substrate effects from subsequent analysis. In Figs. 2.5 (d, e, f), we shows the $LDOS(\mathbf{k}, z)$ at $t_c = 0.3$, where we find the TI surface states are close to that of the ideal ultrathin TI system with a well defined hybridization gap. For this reason, we use the coupling constant $t_c = 0.3$ for the remainder of this work.

2.3.2 Induced s-wave order parameter for bulk and surface states of TI and its spatial distribution

With the non-superconducting Hamiltonian defined, we may now incorporate the superconductivity into the system. In this work, we include superconductivity at the mean-field level, using an intra-orbital on-site interaction of the form [39]

$$\mathcal{H}_{\text{int}} = -V \sum_{\mathbf{k},z,\alpha=A,B} \left\{ \Delta^*_{S,\alpha}(z) b_\alpha(\mathbf{k},z) \ + \Delta_{S,\alpha}(z) b^\dagger_\alpha(\mathbf{k},z) - |\Delta_{S,\alpha}(z)|^2 \right\}, \tag{2.30}$$

where V is the on-site attractive interaction strength, and $b_\alpha(\mathbf{k},z) = (c_{\mathbf{k},z,\alpha\uparrow} c_{-\mathbf{k},z,\alpha\downarrow} - c_{\mathbf{k},z,\alpha\downarrow} c_{-\mathbf{k},z,\alpha\uparrow})$ is the singlet pair annihilation operator. In Eq. (2.30), we set $V > 0$ in the metal to indicate superconducting pairing whereas $V = 0$ in the TI as there is no inherent pairing within the TI. To examine proximity effect of the TI, we define the s-wave order parameter, $\Delta_{S,\alpha}$, as a unitless quantity by separating the interaction strength V from its expression in Eq. (2.30). For definitions and numerical calculation procedures for the order parameter in Eq. (2.30), see Appendix A.3 and Eq. (A.15). To incorporate superconductivity into the non-interacting Hamiltonian of Eq. (2.24), we expand it into a BdG Hamiltonian with corresponding eight-component Nambu spinor $\Phi_{\mathbf{k},z} = [\Psi_{\mathbf{k},z}, \Psi^\dagger_{-\mathbf{k},z}]^T$ as[67]

$$\mathcal{H}_{\text{BdG}} = \sum_{\mathbf{k},z} \Phi^\dagger_{\mathbf{k},z} \begin{bmatrix} \hat{H}_0(\mathbf{k},z) & -V\hat{\Delta}(\mathbf{k},z) \\ -V\hat{\Delta}^\dagger(\mathbf{k},z) & -\hat{H}_0(-\mathbf{k},z)^* \end{bmatrix} \Phi_{\mathbf{k},z} + \Phi^\dagger_{\mathbf{k},z} \begin{bmatrix} \hat{H}_z(z) & 0 \\ 0 & -\hat{H}_z(z)^* \end{bmatrix} \Phi_{\mathbf{k},z+\hat{z}}. \tag{2.31}$$

The intra-orbital s-wave interaction term in Eq. (2.30) is incorporated in the metallic portion of the Hamiltonian through off-diagonal components $\tilde{\Delta}$, which are written as

$$\hat{\Delta}(\mathbf{k},z) = i\sigma_y \otimes \begin{bmatrix} \Delta_{S,A}(\mathbf{k},z) & 0 \\ 0 & \Delta_{S,B}(\mathbf{k},z) \end{bmatrix}. \tag{2.32}$$

Using the material parameters defined in section 2.3.1, we obtain a hybridization gap of $2\delta \simeq 221$ meV and bulk gap of ~ 1.647 eV for the 4 layer thick TI Hamiltonian in Eqs. (2.28, 2.29) in normal phase. The chemical potential of the metal is set to $\mu_m = 0.2t_m$ to obtain sufficient density of states near the chemical potential to induce superconductivity within the metallic system. The interaction strength of the metal is set to $V = 0.2$ eV to obtain a converged superconducting gap whose magnitude in energy is $\sim 0.24\delta$. From the self-consistent solution of the BdG Hamiltonian given in Eq. (2.31), we compute the induced intra-orbital s-wave pair correlation function, $F^{\uparrow,\downarrow}_{A,A}(\mathbf{k},z) = \langle c_{\mathbf{k},z,A\uparrow} c_{\mathbf{k},z,A\downarrow} \rangle$, and corresponding s-wave order parameter,

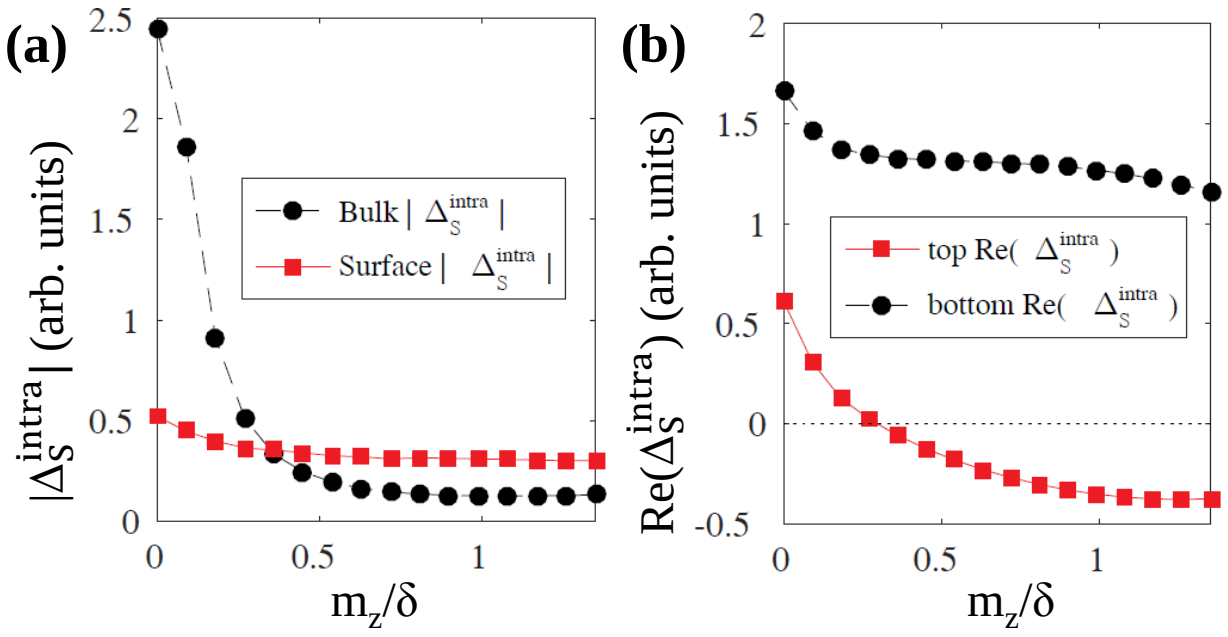

Figure 2.6: (a) A plot of induced s-wave order parameter magnitude as a function of Zeeman splitting energy at the chemical potential $\mu_{TI} = 850$ meV, whose location crosses both bulk and surface bands of the TI. Black circles indicate the bulk state contribution and red squares indicate the surface state contribution for the obtained order parameter at the interface of the metal-TI ($z = 11$). (b) A plot of the induced s-wave order parameter as a function of Zeeman splitting energy at the chemical potential of $\mu_{TI} = \delta$, whose location only crosses the surface bands of the TI. Unlike (a), the induced order parameter is computed solely from the surface states of TI. Black circles indicate the order parameter obtained at bottom layer ($z = 11$), whereas the red squares indicate the order parameter at top layer ($z = 14$). Adapted from [1].

$\Delta_{S,A}(z) = \sum_{\mathbf{k}}[F^{\uparrow,\downarrow}_{A,A}(\mathbf{k},z) - F^{\downarrow,\uparrow}_{A,A}(\mathbf{k},z)]/2$, within the ultrathin TI system. For detailed numerical calculation procedure, see Appendix A.3. Although similar analysis may be done for inter-orbital pairing, we focus on the intra-orbital induced order parameter for this study as an inclusion of the inter-orbital pairing does not differ from the qualitative trends presented here.

We first examine the induced order parameter for surface and bulk states in the TI and compare its relative magnitude, as well as its evolution as a function of the Zeeman energy. To this end, we locate the chemical potential of the TI at $\mu_{TI} = 850$ meV, which crosses both bulk and surface states of the TI. We calculate the magnitude of the intra-orbital s-wave order parameter, $|\Delta_S^{\text{intra}}(z)| = |\Delta_{S,A}(z) + \Delta_{S,B}(z)|$, by considering the surface and bulk state contributions separately as a function of the Zeeman splitting energy. The details of how the bulk and surface contributions are separated are discussed in Appendix A.4. The induced order parameter is maximized at the interface ($z = 11$) as the TI layer is directly coupled to the metallic s-wave superconducting system and decays as a function of depth as we move toward the other TI surface ($z = 14$). To see a clear trend of the induced order parameter as a function of the Zeeman splitting energy, we examine the magnitude of the induced order parameter at the interface ($z = 11$). Considering

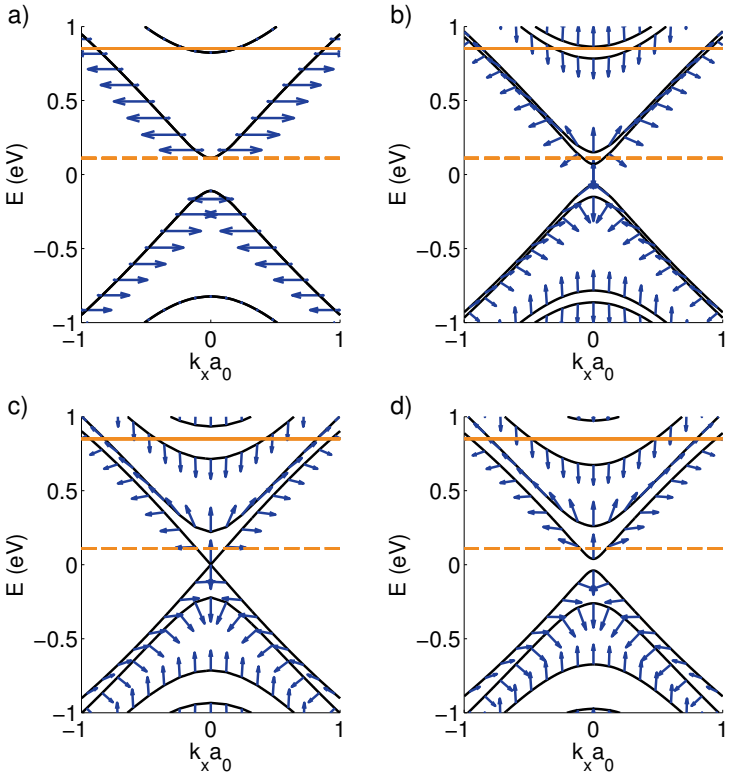

Figure 2.7: Band structure of the non-superconducting 4 layer thick TI with Zeeman energies of (a) 0 meV, (b) 40 meV, (c) 110 meV, and (d) 150 meV with chemical potentials of 850 meV and 111 meV($= \delta$) marked with solid and dashed horizontal lines, respectively. The spin expectation is marked with blue arrows, where the horizontal component of spin corresponds to $\langle S_y \rangle$ and vertical, $\langle S_z \rangle$. (a) With no Zeeman field, we see that the surface bands are gapped due to hybridization between the two surfaces. (b) When a small Zeeman term is included, the bulk states split into strictly up and down spins while the surface states' spin cant out of plane. (c) With a Zeeman term of 110 meV, we observe a quantum phase transition into a Chern insulating state[60]. At this transition, the spin rotates back to an in-plane configuration at small momenta. (d) The Chern insulating state is characterized by the inversion of the band structure, which is apparent in the rotation of spin that is observed within a band when scanning from low to high momenta. Adapted from [1].

that a typical range of the hybridization gap of $3-5$ quintuple layer Bi_2Se_3 is $2\delta \sim 138-41$ meV[68] and magnetic doping induced gap size is $2m_z \sim 87-23$ meV for $\sim 10-0.2$ % Mn doping in Bi_2Se_3[44], we sweep the Zeeman splitting energy up to $m_z/\delta = 1.5$. As we increase m_z, Fig. 2.6(a) shows a rapid decrease in induced order parameter of the bulk states (black circle), whereas the induced order parameter of the surface states (red square) shows nearly constant magnitude. The seemingly different trend of the bulk and surface states may be explained by understanding the changes in band structure and the spin polarization near the Fermi surface. To explain this, we plot the band structure of a 4 layer thick TI with corrsponding spin texture in Fig. 2.7, specifically focusing on the states that cross the solid line representing a chemical potential of $\mu_{TI} = 850$ meV. When $m_z = 0$ in Fig. 2.7(a), we see that the surface states exhibit their spin-locked nature. As the Zeeman field is increased in Figs. 2.7(b-d), the bulk and surface states show qualitatively different pictures. The bulk states split into strictly up and down spin states, making a spin singlet state energetically unfavorable to form and causing Δ_S^{intra} to drop precipitously. The spin of the surface states is markedly different. Because the spin is already locked to momentum at $m_z = 0$, the addition of the Zeeman interaction has the effect of canting the spin out of the xyplane. However, as there is always a projection of spin that is anti-aligned in xyplane, s-wave pairing is always allowed, explaining why the induced s-wave pairing in the surface states decreases much smaller rate than in the bulk.

We now narrow down our scope to the surface states and examine the induced order parameter at the top and bottom surfaces. Particularly, we change our chemical potential and place it to the bottom of the surface band of the TI. As the introduced Zeeman energy lifts the band degeneracy, this particular position of the chemical potential allows us to focus on a single, non-degenerate surface band and the resultant induced order parameter to elucidate and validate our analysis of the 2D surface model in Section 2.2. To this end, we locate the chemical potential of the TI at $\mu_{TI} = \delta$ indicated as a dashed line in Fig 2.7(a). In Fig. 2.6(b), we find a purely real s-wave order parameter from our self-consistent calculation at the top ($z = 14$, red square) and bottom ($z = 11$, black circle) layer of the ultrathin TI. Both top and bottom layer order parameter exhibit positive sign for zero or small Zeeman splitting energy, implying that symmetric part of the pairing is the dominant factor. As we increase Zeeman energy, we lift the degeneracy to separate the surface bands beyond the superconducting gap and observe a sign change in the induced s-wave order parameter at the top layer, implying that the anti-symmetric pairing potential now plays a dominant role over the symmetric pairing potential. Although the overall behavior agrees with the phenomenological model analysis, Fig. 2.6(b) shows that the spatial distribution of the top and bottom layer induced order parameter is always a mixture of the symmetric and anti-symmetric form. This is due to the fact that the 3D model Hamiltonian takes account the effect of the hopping from the metallic system to the TI. For clarity, we adopt

2D surface model to write an analytic expression of the self-energy term including the hopping from metallic system to bottom surface state of the TI as[54]

$$\Sigma(\epsilon) \simeq -\frac{\lambda}{\sqrt{\Delta_m^2 - \epsilon^2}}(\epsilon\tau_0' + \Delta_m\tau_x') \tag{2.33}$$

at energy ϵ. In Eq. (2.33), the Pauli matrices $\tau'_{i=0,1,2,3}$ act on the Nambu space, Δ_m is an assumed order parameter of the s-wave superconducting system, and λ^{-1} is an estimation of the electron life-time at the metal-TI interface which is determined by the hopping constants, t_c and t_m, and the chemical potential of the metal. The phenomenological model in Eq. (2.10) takes account second term of Eq. (2.33), however, the first term has been ignored. Assuming that the above self-energy is applied only to the bottom layer of the ultrathin TI due to its direct proximity to the metallic system, we may insert the first term as an on-site potential within the bottom layer Hamiltonian. Specifically, we first define the first term of the self-energy in Eq. (2.33) as $\Sigma_{1,\epsilon} = -\epsilon\lambda/2\sqrt{\Delta_m^2 - \epsilon^2}$. Utilizing the symbols defined in Eq. (2.2) and below, we incorporate the first term of the self-energy in Eq. (2.33) with the 2D surface Hamiltonian in Eq. (2.2) as an on-site potential at bottom layer, $\hat{H}_{BdG,\Sigma_{1,\epsilon}} = \Sigma_{1,\epsilon}\tau_0' \otimes (I_2 \otimes I_2 - \tau_z \otimes I_2) = \tau_0' \otimes \hat{H}_{\Sigma_{1,\epsilon}}$. Following the discussion in Eq. (2.3), we apply the relevant rotational matrices to obtain a surface Hamiltonian

$$\hat{H}'_{surf}(k,\epsilon) = U_2U_1[\hat{H}_{surf}(k_x,k_y) + \hat{H}_{\Sigma_{1,\epsilon}}]U_2^\dagger U_1^\dagger, \tag{2.34}$$

whose matrix form is

$$\hat{H}'_{\text{surf}}(k,\epsilon) = \begin{pmatrix} m_2 - \mu' & 0 & -\Sigma_{1,\epsilon} & -k \\ 0 & m_1 - \mu' & -k & -\Sigma_{1,\epsilon} \\ -\Sigma_{1,\epsilon} & -k & -m_1 - \mu' & 0 \\ -k & -\Sigma_{1,\epsilon} & 0 & -m_2 - \mu' \end{pmatrix}, \tag{2.35}$$

where $\mu' = \mu + \Sigma_{1,\epsilon}$. Note that the off-diagonal term, $\Sigma_{1,\epsilon}$, in Eq. (2.35) couples the sectors 1 and 2 which were previously decoupled in Eq. (2.4). Considering the correlation function near the chemical potential, or $\epsilon \sim 0$, the additional coupling term $\Sigma_{1,\epsilon}$ has a small but non-zero value. Therefore, the presence of the coupling between sector 1 and sector 2 leads the co-existence of the symmetric and anti-symmetric components of the induced order parameter, as we no longer can decouple sector 1 and sector 2 completely. As a result, Fig. 2.6(b) exhibits the spatial distribution of the induced order parameter as a mixture of the symmetric and anti-symmetric form and exhibits a smooth transition of the pairing potential from symmetric to anti-symmetric form. Nevertheless, we clearly observe a transition of the induced s-wave order parameter

from a symmetric dominant to an anti-symmetric dominant spatial distribution and thereby confirm that qualitative behavior of the induced order parameter is sufficiently captured at the phenomenological level.

2.4 Conclusion

In summary, we studied magnetically-doped ultrathin TI system that is proximity coupled to a conventional s-wave superconductor in order to identify possible topological phases. We find that the system is described in two individual sectors comprised of the hybridized basis with top and bottom surfaces of TI. Using a simplified picture for proximity induced order parameter, we identify that a symmetric and anti-symmetric spatial configuration of the induced order parameter pair electrons in the individual sectors differently. Our subsequent analysis of the total energy of this system reveals that the anti-symmetric spatial distribution of the induced order parameter is dominant in the presence of a Zeeman energy larger than the magnitude of the induced order parameter. As the choice of an anti-symmetric order parameter greatly simplifies the analysis, we perform analytic analysis on the quasi-particle spectrum of the BdG Hamiltonian. We then find the gap closing points at $\mathbf{k} = 0$ and identify that the gap closing points are modified by the hybridization gap, Zeeman energy, and chemical potential of the ultra-thin TI. Taking account both symmetric and anti-symmetric pairing potential, we draw a generic phase diagram to identify a relevant region in parameter space for topological superconductivity. To enhance our understanding on proximity coupled ultrathin TI system, we study a more realistic model with a four band 3D TI Hamiltonian directly coupled with metallic superconducting system. In this system, the induced order parameter is determined self-consistently. We confirm that our phenomenological model captures the correct behavior of the induced order parameter as the self-consistently determined order parameter shows a clear transition from symmetric to anti-symmetric dominant spatial distribution form. Furthermore, the results show that the surface state induced s-wave order parameter survives even at a relatively high magnitude of Zeeman energy, whereas the bulk state induced s-wave order parameter exhibits a rapid decay for the increased Zeeman energy. We believe that this work not only explains why topological superconductivity yet to be observed in this system, but also provides useful experimental insight into the proper choice of parameters where it may be found.

Chapter 3

Fulde-Ferrell States in Magnetically-Doped Topological Heterostructures

[1]

3.1 Introduction

In chapter 2, we find that the topological superconductivity can be induced in the thin-film limit of the topological insulator-superconductor proximity effect. Besides the topological character, we now study the pairing symmetry that may arise in the superconducting proximity effect of the 3D topological insulator. The superconducting states with non-trivial linear momentum have been proposed to exist in strong spin-orbit coupled materials other than TI[69, 70, 71, 72, 73, 74, 75, 3]. The examples are spin orbit coupled Fermi gases in the cold atom systems[70, 71, 72, 73] and the bulk doped Weyl semimetals[74, 75, 3]. This unconventional superconducting state is known as Fulde-Ferrell-Larkin-Ovchinnikov(FFLO) phase, in which Cooper pairs in equilibrium have a non-zero linear momentum. The FFLO phase is predicted to exhibit phenomena, which are not found in the conventional BCS superconductors such as a spatial modulation of the pairing potential[76, 77] in equilibrium. The FFLO phase has been proposed when coupled with the ferromagnetic alloys[76], which utilize spin imbalanced Fermi surface to generate finite momentum pairing[78]. Interestingly, a non-trivial Fraunhofer pattern in HgTe quantum well[79], which may support the finite momentum pairing, has been recently observed with the application of the external magnetic field. Nevertheless, a clear signature of the FFLO pairing in the absence of the external field is lacking in the condensed matter systems. While the spin-orbit coupled materials are known to offer a larger parameter space to support the FFLO phase[70], it is desirable to explore candidate spin-orbit coupled systems comprised of readily available materials. In this regard, we propose a ground state with the FF pairing can occur in a conventional BCS superconductor that is proximity-coupled to a magnetically doped TI surface state. The FF pairing is a specific type of the FFLO phase that is characterized the spatial modulation of the order parameter phase while the LO pairing is characterized by the modulation of the superconducting pairing amplitude. In our

[1] Portions of this study were previously published as [2] and reprinted with permission (Copyright 2017 by American Physical Society).

setup, the magnetic dopants within the TI induce a uniform Zeeman field pointing in a direction parallel to the surface. Our proposal has clear advantages in experimental accessibility: i) The proximity coupled superconductivity on the surface of the TI has been widely realized[80, 81, 52, 82, 83, 80, 84, 85, 86, 87, 88]. ii) The magnetic energy gap in the magnetically doped surface of TI with non-zero exchange field has been experimentally observed[89, 90]. iii) There is no magnetism inside the superconductor. Thereby ensuring superconductivity is preserved. In this work, we analyze the energetics of a proximity-coupled magnetically doped TI-superconductor structure to determine the stability of the FF phase as function of experimentally relevant parameters.

First, in section 3.2, we introduce a model that describes the proximity coupled structure of a TI and a conventional BCS superconductor. Here we utilize the low energy bands of Bi_2Se_3 derived from ARPES experiment and a free electron model with effective mass and chemical potential derived from first principle calculation to accurately capture the relevant physics of the recent experiments $NbSe_2$[80, 52, 88]. In this model, we choose the model of the superconductor to be relevant to $NbSe_2$ due to its wide use in experiments[52]. In section 3.3, we show that the metallic bands of the superconductor exhibit an anisotropic Fermi surface in the Brillouin zone(BZ) as a consequence of the 'inverse proximity effect'(IPE), which we denotes as the proximity effect of the TI acting upon the superconductor[91]. In section 3.4, we use mean-field theory of superconductivity to calculate the energetic stability of the BCS pairing and the FF pairing. We show that the metallic bands of the superconductor can have a FF pairing as its ground state in the thin film limit due to the proximity induced anisotropic Fermi surface, where the decay length of the IPE exceeds the entire region of the superconductor. We also consider the case where the thickness of the superconductor exceeds the penetration length of the IPE. We find that the FF pairing becomes unstable as the thickness of the superconductor increases, since more BCS favored bands become populated and overwhelm the FF phases. Nevertheless, we show that the FF pairing can survive at the interface of the heterostructure in the thick sample limit. In section 3.5, we propose two transport methods to measure the induced FF phase. Our transport proposals show distinct transport signatures that distinguish the FF phase from that of the conventional superconductor.

3.2 Model

In Fig. 3.1, we show the system comprised of a metallic superconductor grown on top of a magnetically doped 3D TI. We begin our discussion by writing down the metallic Hamiltonian that describes the parent superconductor. We model the metallic bands of the superconductor using a free electron model with the

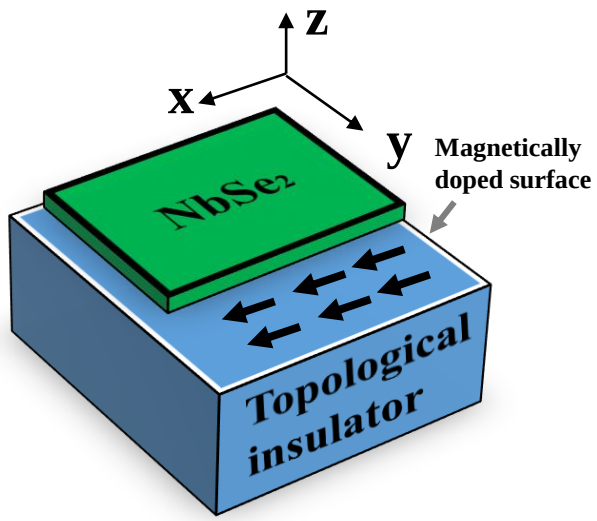

Figure 3.1: The schematic figure of the magnetically doped TI superconductor hetero-structure. On the top of the TI surface, a thin film of the BCS superconductor is deposited. The magnetization points out the parallel direction to the surface of the TI to shift the location of the Dirac cone in momentum space. Adapted from [2].

effective mass m_M and the effective chemical potential μ_M [92, 93]:

$$\hat{H}_M(\mathbf{k}) = \frac{k^2}{2m_M} - \mu_M \tag{3.1}$$

where $k = \sqrt{k_x^2 + k_y^2}$ is the magnitude of the in-plane momentum, Throughout this work, we set the value of the effective mass to be $\frac{1}{2m_M} = -0.5eV$ and the chemical potential to be $\mu_M = -0.8eV$ in order to capture the relevant scale of parameters in existing experiments using $2H - NbSe_2$ as $2H - NbSe_2$ is the most commonly used superconductor to observe the proximity effect in the TI. $2H - NbSe_2$ is known to be superconducting even in single layer limit having a reduced critical temperature of $T = 1.9K$, as compared to its bulk critical temperature of $T = 7.2K$[94]. We extracted the parameters of the effective mass and the chemical potential from the central Fermi pocket of $NbSe_2$ at Γ point using quadratic fitting. We only consider the central Fermi pocket as it has momentum matching with the topological surface states.

We now consider the surface state Hamiltonian of the magnetically doped 3D TI:

$$\hat{H}_{TI}(\mathbf{k}) = v_F(k_x\sigma_y - k_y\sigma_x) + m\sigma_x - \mu_{TI}I_2, \tag{3.2}$$

where, without loss of generality, we set $\hbar = 1$. v_F is the Fermi velocity of the TI surface state, m is the exchange field Zeeman term, μ_{TI} is the chemical potential of the TI, I_2 is 2×2 identity matrix, and σ_i is

the i-th Pauli matrix for spin. The choice of the above parameters is taken from ARPES experiments[95] of the surface bands to derive the values of the parameters: $v_F = 1.19eV$ and $\mu_{TI} = 0.26eV$. From Eqs. (3.1) and (3.2), our system is described by the total Hamiltonian written as

$$H_{M-TI} = H_M + H_{TI} + H_{coupling}. \tag{3.3}$$

In Eq. (3.3), the metallic Hamiltonian is $H_M = \sum_{\mathbf{k}} \psi^\dagger_{M,\mathbf{k}} \hat{H}_M(\mathbf{k}) \psi_{M,\mathbf{k}}$ in which we define the 2 component spinor $\psi_{M,\mathbf{k}} = [d_{\mathbf{k}\uparrow}, d_{\mathbf{k}\downarrow}]^T$, and $d^\dagger_{\mathbf{k}\uparrow}$ ($d_{\mathbf{k}\downarrow}$) is up-spin (down-spin) electron creation (annihilation) operator of the metal. Likewise, the TI Hamiltonian is $H_{TI} = \sum_{\mathbf{k}} \psi^\dagger_{TI,\mathbf{k}} \hat{H}_{TI}(\mathbf{k}) \psi_{TI,\mathbf{k}}$ where we define $\psi_{TI,\mathbf{k}} = [c_{\mathbf{k}\uparrow}, c_{\mathbf{k}\downarrow}]^T$ where $c^\dagger_{k\uparrow}$ ($c_{\mathbf{k}\downarrow}$) is up-spin (down-spin) electron creation (annihilation) operator. In Eq. (3.3), we introduce $H_{coupling}$ which couples the TI and the metallic system as

$$H_{coupling} = \sum_{\mathbf{k},s=\uparrow\downarrow} t_c (c^\dagger_{\mathbf{k}s} d_{\mathbf{k}s} + d^\dagger_{\mathbf{k}s} c_{\mathbf{k}s}) \tag{3.4}$$

where t_c is a coupling constant between the metal and the TI. In general, the tunneling between the TI surface and the superconductor hops between different in-plane momenta in the BZ. This is due to a lattice mismatching between the two materials and disorder on the interface. In this work, we assume a clean interface limit between the two materials. Therefore, the in-plane momentum is conserved. From the Hamiltonian in Eqs. (3.1), (3.2), and (3.4), we construct the matrix form of the metal-TI heterostructure Hamiltonian, $H_{M-TI} = \sum_{\mathbf{k}} \Psi^\dagger_{\mathbf{k}} \hat{H}_{M-TI}(\mathbf{k}) \Psi_{\mathbf{k}}$, where

$$\hat{H}_{M-TI}(\mathbf{k}) = \begin{pmatrix} \hat{H}_M(\mathbf{k}) & \hat{H}_{coupling} \\ \hat{H}^\dagger_{coupling} & \hat{H}_{TI}(\mathbf{k}) \end{pmatrix}, \tag{3.5}$$

with the operator $\Psi_{\mathbf{k}} = [\psi_{TI,\mathbf{k}}, \psi_{M,\mathbf{k}}]^T$, and the coupling Hamiltonian $\hat{H}_{coupling} = t_c I_2$.

3.3 Inverse proximity effect

After establishing the description of the model and the Hamiltonian, we now consider the IPE of the TI to the metallic bands of the superconductor. We choose to examine the IPE in this model in recognition of the fact that the IPE on the superconductor will significantly alter the metallic bands and the corresponding superconductivity. The IPE can be evaluated by calculating the effective Hamiltonian of the metallic region in the presence of the finite coupling, t_c, with the TI. To calculate the effective Hamiltonian, we first consider the full matrix form of the Schrodinger equation without the superconducting pairing term, as given in Eq.

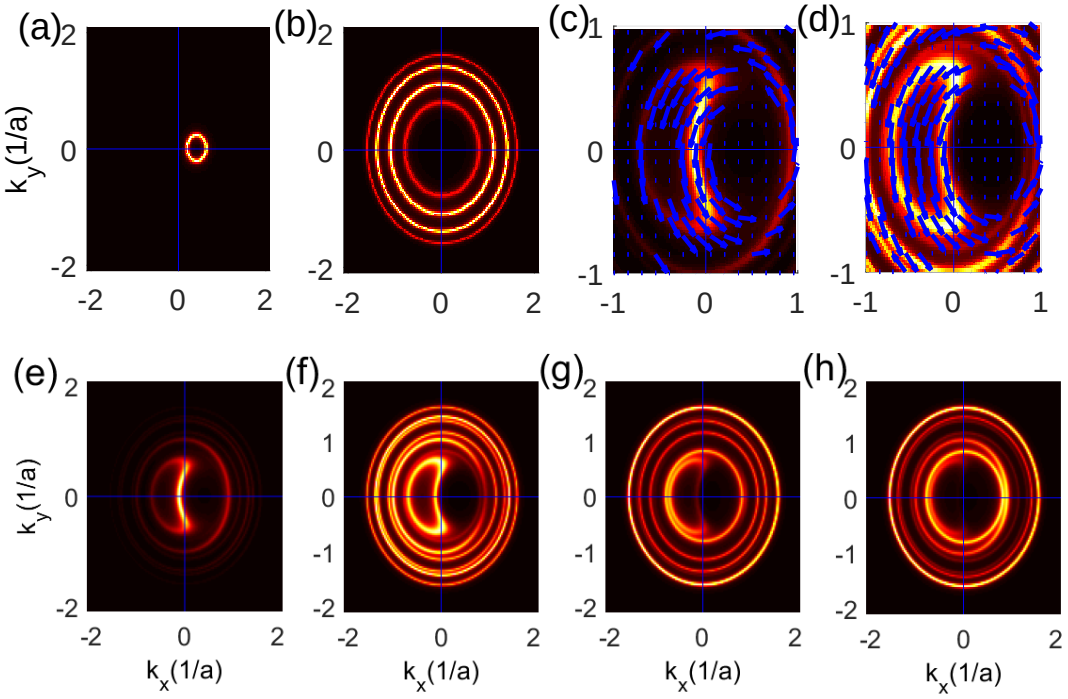

Figure 3.2: The local density of the state in momentum space at the TI and the superconductor with $m = 0.4eV$ and $t_c = 0.5eV$. (a) and (b) show the LDOS of the TI and the first layer of the superconductor when $t_c = 0$. The magnetically ordered dopants shift the Dirac cone along the x-direction because the magnetism is aligned in the x-direction. As t_c is turned on, the IPE starts to hybridize the Fermi surface. (c) and (d) show the LDOS and the spin texture. We find the non-zero spin orbit coupling and the effective Zeeman field in the superconductor. (e)-(h) show the LDOS of the TI surface and the first, the second, and the third layer of the superconductor. We find that the Fermi surface starts to recover the isotropy and the IPE decays as we look further away from the surface of the TI. Adapted from [2].

(3.5):

$$\begin{pmatrix} \hat{H}_M & \hat{H}_{couple} \\ \hat{H}^\dagger_{couple} & \hat{H}_{TI} \end{pmatrix} \begin{pmatrix} \psi_m \\ \psi_{TI} \end{pmatrix} = E \begin{pmatrix} \psi_m \\ \psi_{TI} \end{pmatrix} \tag{3.6}$$

where ψ_m and ψ_{TI} is the wave function in the metallic and the TI region respectively and E is the corresponding energy eigenvalue. To derive the self-energy term, $\hat{\Sigma}(E)$, which takes account the effect of the IPE, we integrate out the wave function in the TI region. The new effective Hamiltonian of the metal with the self-energy term now satisfies the following Schrodinger equation,

$$\hat{H}_{eff}(E)\psi_m = (\hat{H}_m + \hat{\Sigma}(E))\psi_m = E\psi_m \tag{3.7}$$

where the self energy is evaluated as,

$$\begin{aligned} \hat{\Sigma}(E) &= \hat{H}_{couple}(E - \hat{H}_{TI})^{-1}\hat{H}^\dagger_{couple} \\ &= \frac{t_c^2}{m^2 + (v_F|k|)^2 - \mu_{TI}^2} \begin{pmatrix} \mu_{TI} + m & -v_F(k_y + ik_x) \\ -v_F(k_y - ik_x) & \mu_{TI} - m \end{pmatrix}. \end{aligned} \tag{3.8}$$

As it has been shown from Eq. (3.8), the effective metallic Hamiltonian now possesses a non-zero spin-orbit coupling and a non-zero Zeeman field with the coefficients of the strengths being $\frac{t_c^2 v_F}{m^2+(v_F|k|)^2-\mu_{TI}^2}$ and $\frac{t_c^2 m}{m^2+(v_F|k|)^2-\mu_{TI}^2}$, respectively. The presence of the both spin-orbit coupling and the Zeeman field distort the isotropic Fermi surface and shift the center of the momentum, which eventually decreases the energy gain from the Fermi surface instability under the singlet BCS pairing of the metal.

After deriving the analytical insight into the IPE, we now confirm the IPE by numerically evaluating the local density of state in the metallic region. The local density of state(LDOS) can be computed from the calculation of the imaginary part of the spectral function which is given as,

$$LDOS(\omega, i, k) = \sum_n -Im(\frac{|\phi_{n,i}(k)|^2}{\omega - E_n + i\eta}) \tag{3.9}$$

where η is the infinitesimal broadening of the states, $\phi_{n,i}$ is the n-th eigenstate, and E_n is the corresponding energy eigenvalue of the system. i is the orbital degree of the freedom which represent the z coordinate.

The local spin density of state(LSDOS) can be similarly calculated by inserting pauli matrix by following

$$LSDOS_j(\omega, i, k) = \sum_n -Im(\frac{< \phi_{n,i}(k)|\sigma_j|\phi_{n,i}(k) >^2}{\omega - E_n + i\eta}) \tag{3.10}$$

In Fig. 3.2, we plot the numerically computed $LDOS(\omega, k)$ to show the change of the metallic bands of the superconductor due to the IPE. Figs. 3.2 (a) and (b) show the LDOS of the TI and the metallic layers, respectively, at $t_c = 0$. In Fig. 3.2 (a), we find that the Fermi surface of the TI is shifted in $\hat{x}$ direction as the finite Zeeman term shifts the location of the Dirac cone to $\Delta k_x = \frac{m}{v_F}$ in the BZ. Since the IPE($t_c = 0$) is zero, Fig. 3.2 (b) still shows isotropic fermi surfaces of the metallic bands in which one can always find a conventional BCS cooper pair with opposite momenta $\mathbf{K}$ and $-\mathbf{K}$ on the Fermi surface. On the other hand, as t_c is turned on, we find that the the surface bands of the TI and the metallic bands of the superconductor layers start to hybridize. Fig. 3.2 (c) and (d) shows the hybrdized Fermi surface and corresponding spin texture of the TI and the first layer of the metal respectively. While the singlet superconducting pairing only couples the opposite spins, the LDOS depicted in Fig. 3.2 (d) does not possesses a pair of the states that have opposite spins and zero net momentum simultaneously. On the other hand, Fig. 3.2 (d) alternatively shows that a pair of the states with opposite spins have rather a finite net momentum along x direction, which leads to the FF instability. In this case, it is not guaranteed to find two arbitrary electrons with the opposite momenta and the opposite spin on the Fermi surface. As a consequence, the BCS pairing may not be efficiently formed to lower the total ground state energy and the finite momentum pairing phase may have lower ground state energy. Indeed, we observe that the system with induced anisotropic Fermi surface favors FF states in certain parameter space in section 3.4. Additionally, Figs. 3.2 (e)-(h) show the LDOS of the TI and the first, the second, and the third superconductor layer respectively. While Figs. 3.2 (e) and (f) shows the same anisotropic LDOS shown in Figs. 3.2 (c) and (d), we immediately observe that Fig. 3.2 (g) and (h) show the anisotropy of the Fermi surface decays as we look further away from the interface between the metal and the TI. This is the consequence of the exponential decaying of the IPE away from the interface. As can be seen from Eq. (3.8), the strength of the IPE decays exponentially as the inter-layer directional hopping of the $NbSe_2$ is known to be very small compared to the hopping in the intra-layer direction[92, 93], so that we expect the proximity effect of the TI only survives in the first few layers.

3.4 Numerical Calculation of the ground state energies

3.4.1 Single-layer limit of the superconductor

With our understanding on the IPE of the metallic Hamiltonian, we consider superconducting phase to calculate ground state energy of the BCS and the FF states. We first consider the s-wave superconducting order in metallic system. The s-wave pairing Hamiltonian in mean-field level is

$$H_{BCS} = -U \sum_{\mathbf{k}} [\Delta d^{\dagger}_{\mathbf{k}\uparrow} d^{\dagger}_{-\mathbf{k}\downarrow} + \Delta^* d_{-\mathbf{k}\downarrow} d_{\mathbf{k}\uparrow} - |\Delta_{\mathbf{k}}|^2] \tag{3.11}$$

where $U = 2eV > 0$ is the on-site attractive interaction and $\Delta = \sum_{\mathbf{k}} \langle d_{-\mathbf{k}\downarrow} d_{\mathbf{k}\uparrow} \rangle$ is the superconducting order parameter. As our major interest is in FF phase, we further introduce FF pairing in the Hamiltonian whose mean-field form is

$$H_{FF} = -U \sum_{\mathbf{k}} [\Delta_{\mathbf{q}} d^{\dagger}_{\mathbf{k}+\mathbf{q}\uparrow} d^{\dagger}_{-\mathbf{k}+\mathbf{q}\downarrow} + \Delta^*_{\mathbf{q}} d_{-\mathbf{k}+\mathbf{q}\downarrow} d_{\mathbf{k}+\mathbf{q}\uparrow}], \tag{3.12}$$

where the superconducting order parameter is now defined as $\Delta_{\mathbf{q}} = \sum_{\mathbf{k}} \langle d_{-\mathbf{k}+\mathbf{q}\downarrow} d_{\mathbf{k}+\mathbf{q}\uparrow} \rangle$, and the Cooper pair carries a finite momentum of $2\mathbf{q}$. We construct Bogoliubov de Gennes (BdG) Hamiltonian whose matrix form is

$$H_{BdG} = \sum_{\mathbf{k}} \Phi^{\dagger}_{\mathbf{k}+\mathbf{q}} \begin{pmatrix} \hat{H}_{M-TI}(\mathbf{k}) & \hat{H}_{pair}(\mathbf{q}) \\ \hat{H}^{\dagger}_{pair}(\mathbf{q}) & -\hat{H}^*_{M-TI}(-\mathbf{k}) \end{pmatrix} \Phi_{\mathbf{k}+\mathbf{q}}, \tag{3.13}$$

where we define the 8-component Nambu spinor $\Phi_{\mathbf{k}+\mathbf{q}} = [\Psi_{\mathbf{k}+\mathbf{q}}, \Psi^*_{-\mathbf{k}+\mathbf{q}}]^T$, and the pairing Hamiltonian is defined as

$$\hat{H}_{pair}(\mathbf{q}) = \begin{pmatrix} U\Delta_{\mathbf{q}} i\sigma_y & 0 \\ 0 & 0 \end{pmatrix}. \tag{3.14}$$

Alternatively, we may define

$$\hat{H}_{BdG}(\mathbf{k}, \mathbf{q}) = \begin{pmatrix} \hat{H}_{M-TI}(\mathbf{k}-\mathbf{q}) & \hat{H}_{pair}(0) \\ \hat{H}^{\dagger}_{pair}(0) & -\hat{H}^*_{M-TI}(-\mathbf{k}-\mathbf{q}) \end{pmatrix}, \tag{3.15}$$

which satisfies $H_{BdG} = \sum_{\mathbf{k}} \Phi^{\dagger}_{\mathbf{k}} \hat{H}_{BdG}(\mathbf{k}, \mathbf{q}) \Phi_{\mathbf{k}}$. By setting $\mathbf{q} = 0$, Eq. (3.15) becomes BdG Hamiltonian for BCS pairing.

With the Hamiltonian defined in Eq. (3.15), the BdG Hamiltonian can be diagonalized through Bogoli-

ubov transformation as[96]

$$\begin{pmatrix} d_{\mathbf{k}s} \\ d^{\dagger}_{-\mathbf{k}\bar{s}} \end{pmatrix} = \sum_{n} \begin{pmatrix} u^{*}_{n,s} & v_{n,s} \\ -v^{*}_{n,\bar{s}} & u_{n,\bar{s}} \end{pmatrix} \begin{pmatrix} \gamma_n \\ \gamma^{\dagger}_n \end{pmatrix}, \tag{3.16}$$

where $s = \uparrow$ ($\downarrow$) is an index for up (down) spin, $\bar{s}$ indicates opposite spin index from s, $\gamma^{\dagger}_n$ (γ_n) is the creation operators for a quasi-particle (quasi-hole) operator, and n is the eigenstate index. In Eq. (3.16), u and v are the matrix elements of the eigenvector matrix, V, which satisfies $\hat{H}_{BdG}V = VD$ where D is a diagonal matrix containing $2n$ eigenvalues. Then, the correlation function at zero temperature is obtained as

$$F_{s\bar{s}}(\mathbf{k}, \mathbf{q}) = \langle d_{-\mathbf{k}\bar{s}} d_{\mathbf{k}s} \rangle = \sum_{n} u^{*}_{n,\bar{s}} v_{n,s} \tag{3.17}$$

where the summation over n is performed up to the filled states. The correlation function contains the information of the singlet order parameter, and it may be obtained from the following relation[96],

$$\Delta_{\mathbf{q}} = \sum_{\mathbf{k}} \frac{1}{2} \left[F_{\uparrow\downarrow}(\mathbf{k}, \mathbf{q}) - F_{\downarrow\uparrow}(\mathbf{k}, \mathbf{q}) \right]. \tag{3.18}$$

The order parameter from Eq. (3.18) is fed back to Eq. (3.15) until the change of each of the components of the density matrix reaches the convergence of 10^{-4}. Finally, at zero temperature limit, the ground state energy is computed by[96]

$$E_{\mathbf{q}} = \sum_{n} E_n + U\Delta^2_{\mathbf{q}}, \tag{3.19}$$

where we sum over all negative energies. Given the magnetization of the TI, we sweep over all possible $\mathbf{q}$ to obtain the minimum energy for finite $\mathbf{q}$ to determine the ground state energy of the FF pairing states, denoted by E_{FF}. In addition, we obtain BCS ground state energy by setting $\mathbf{q} = 0$, denoted by E_{BCS}. Then the favored supercodnucting ground state is determined by comparing E_{FF} and E_{BCS}. It is important to note that we only add superconducting pairing interaction in the metallic region to model the proximity effect. As a consequence, the corresponding energetics are not dependent on the superconducting state of the TI. More precisely, we examine the FF superconducting state of the parent superconductor, even if the parent superconductor originally favors the BCS ground state. We look for the FF phase induced in the parent superconductor due to the spin orbit coupling from the IPE.

Using the self-consistent calculation of the superconductivity described in Eqs. (3.13)-(3.19), we now present the numerical calculations of the ground state energy with finite momentum pairing. Fig. 3.3 (a) shows the energy contour plot as a function of the Zeeman field, m, and the momentum, $\mathbf{q}$, of the FF phase. As indicated by the blue line in Fig. 3.3 (a), We find that the local minimum of the energy with the non-zero

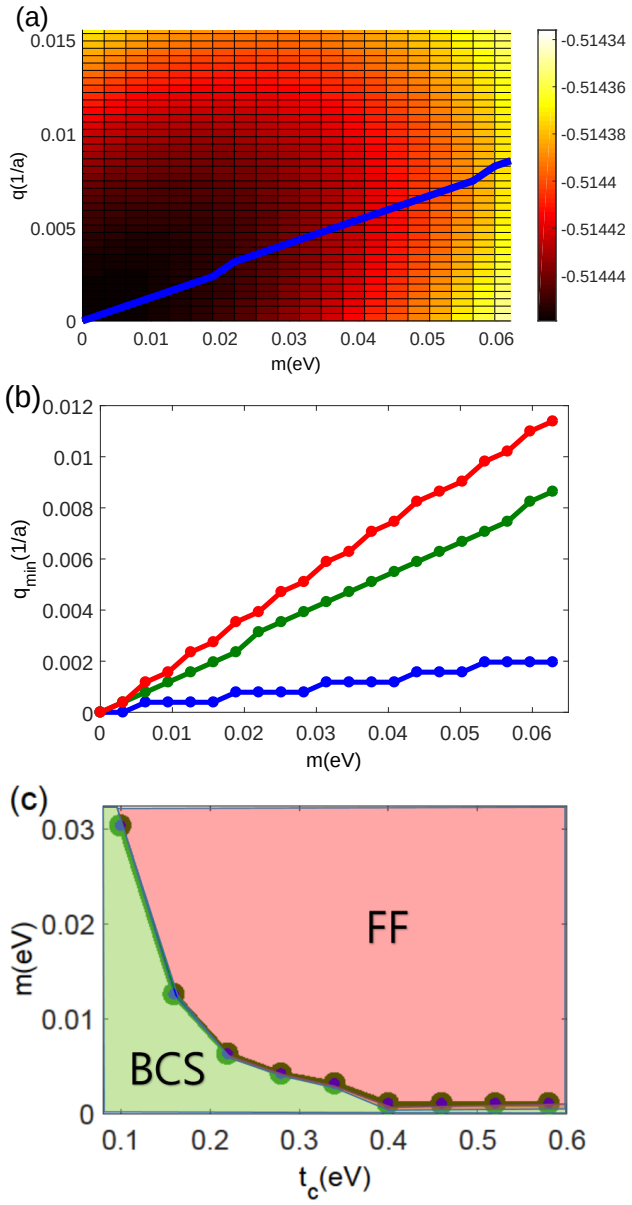

Figure 3.3: (a) The energy contour of the ground state energy as a function of q and m. The region with $q = 0$ corresponds to the BCS energy. As m increases, we find the minimum of the energy occurs at non-zero q which signals the FF ground state. The blue line shows the evolution of the location of the minimum as m increases. We find that q_{min} increases as m increases. (b) The calculation of q_{min} with various values of $t_c = 0.3, 0.6, 1eV$. We find a clear linear dependence of q_{min} respect to m. As t_c increases the slope of the line increases due to the enhanced IPE. (c) By sweeping all possible value of q_{min}, we determine the pairing of the ground state with different values of t_c and m. We find that the stronger t_c and m enhance the stability of the FF phase. Adapted from [2].

$\mathbf{q}$ exists at each Zeeman field, m. By tracking the location of the local minimum, $\mathbf{q}_{min}$, at each m, we find a linear relationship between m and $\mathbf{q}_{min}$, which shows the clear signature that the finite Zeeman field in TI is inducing a FF ground states. This proximity induced local minima can be better understood by repeating the same calculations for various values of the coupling strength between the TI and the superconductor. Fig. 3.3 (b) shows the dependence of $\mathbf{q}_{min}$ with the Zeeman field m with various value of t_c. We find that the slope of the $\mathbf{q}_{min}$ increases as t_c increases. The increase of the slope can be understood from the enhancement of the proximity effect due to the increase of t_c. From the calculation of $\mathbf{q}_{min}$, we conclude that the anisotropy of the Fermi surface due to the IPE favors the finite momentum pairing state. It is important to note that the clear linear dependence we find is limited in the weak Zeeman field limit. This linear dependence of the $\mathbf{q}_{min}$ has been similarly observed in other spin orbit coupled systems in the weak field limit[70].

As we find that the energy of the FF state can be lower than the BCS energy ground state, we now draw the region within parameter space where the FF state is stabilized. This is calculated by comparing the ground state energy of the FF state with all possible momentum $\mathbf{q}$ and that of the BCS state. By computing the difference of the energies in Fig. 3.3 (c), we find that the region of the parameter spaces where the FF phase is favored. As we can see from the dependence of the Zeeman field, m, and the coupling strength, t_c, we find that the area of FF phase increases as t_c increases and m increases. This trend is a consequence of the stronger anisotropy of the metallic bands resulting from the IPE with higher t_c and m. Interestingly, in both weak and strong coupling regime of t_c, we still find the stable FF phase around 10meV strength of the Zeeman field, which is an experimentally achievable value.

3.4.2 Multiple-layers of the superconductor

In the previous section, we found the stable FF phase in the single layer limit of the superconductor. In this section, we now consider the case where the 2D superconductor is thick enough that the normal bands have multiple Fermi surfaces. Unlike in the case of the single layer limit of 2D superconductor, the multi-layer superconductor may have a smaller region of the FF phase since the number of the bands, which originally favors the BCS superconductivity, is increased. Moreover, as shown in the section 3.3, the IPE is a short ranged effect where the strength of the spin-orbit coupling decays exponentially away from the interface between the TI and the superconductor. Hence, we expect the FF phase becomes more unstable as the thickness of the superconductor increases. In this section, we numerically calculate the thickness dependence of the stability of the FF phase. To do so, we consider multi-layer metallic Hamiltonian.

In order to consider the multilayer Hamiltonian, we introduce the Hamiltonian that connects two adjacent

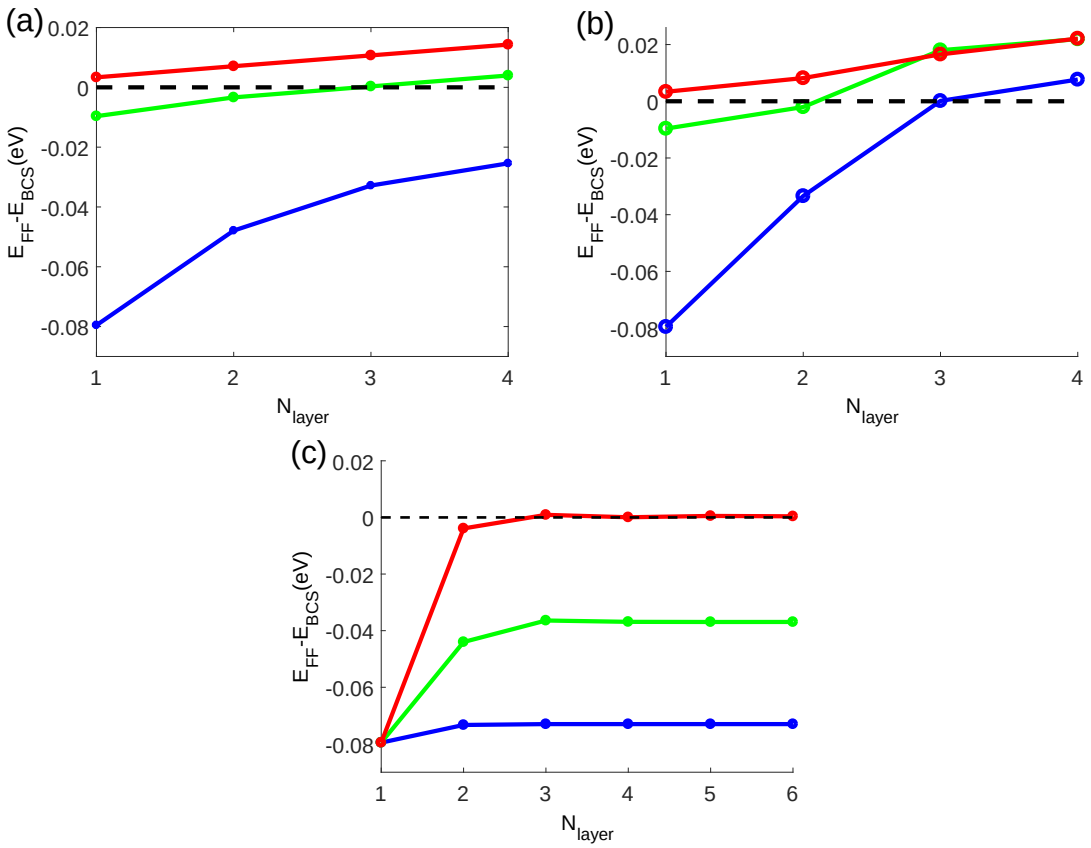

Figure 3.4: The evolution of the ground state energy difference between the FF phase and the BCS phase. The negative value indicates the FF phase is more energetically favored. (a) The energy difference when $t_c > t_m = (0.1eV)$. We find that the energy gain of having the FF phase linearly decreases as N_{Layer} increases. The different value of t_c sets the initial energy gain when $N_{Layer} = 1$. The red, the green and the blue indicates the value of $t_c = 0.3, 0.6, 1eV$ respectively. (b) The same plot when $t_c < t_m = (1eV)$. The linear dependence disappears in the small N_{Layer}, however the same trend still holds in large N_{Layer} (c) The calculation of the energy difference between the interface FF pairing and the BCS pairing. Unlike the homogeneous FF, we find that the energy difference saturates as N_{Layer} increases, indicating that the interface FF might still survive in large N_{Layer} limit. The red, the green and the blue indicates the value of $t_m = 0.1, 0.3, 0.6eV$ respectively. Adapted from [2].

metallic systems, $\hat{H}_m = t_m I_4$, where t_m is inter-layer hopping parameter. We also model the TI surface state by explicitly modelling bulk Hamiltonian, $H_{TI,bulk}$[95], possessing the same surface Hamiltonian as Eq. (3.2). Then we construct the multi-layer metallic Hamiltonian using the following construction:

$$\hat{H}_{3D} = \begin{pmatrix} \hat{H}_{M2} & \hat{H}_m & 0 & \cdots & \cdots & 0 \\ \hat{H}_m^\dagger & \hat{H}_{M2} & \hat{H}_m & \cdots & \cdots & 0 \\ 0 & \hat{H}_m^\dagger & \hat{H}_{M2} & \ddots & & \vdots \\ \vdots & \vdots & \ddots & \ddots & \hat{H}_m & \vdots \\ \vdots & \vdots & & \hat{H}_m^\dagger & \hat{H}_{M2} & \hat{H}_{couple} \\ 0 & 0 & \cdots & \cdots & \hat{H}_{couple}^\dagger & \hat{H}_{TI,bulk} \end{pmatrix}. \tag{3.20}$$

where $\hat{H}_{couple} = t_c I_4$, and $\hat{H}_m = t_m I_4$. $H_{M2} = H_M \otimes I_2$. I_4 is four dimensional identity matrix During the calculation of the multi-layer superconductivity, we model all the coordinates in the real space by numerically fourier transforming the Hamiltonian to consider the interface FF.

By comparing the ground state energies of the Hamiltonians which have the FF and the BCS pairing over the entire region of the superconductor, Fig 3.4 (a) shows the energy difference($\Delta E = E_{FF} - E_{BCS}$) between the FF and BCS as a function of the number of the superconductor layer, N_{layer}, where $t_c > t_m$. Although we expect $t_c < t_m$ regime is more experimentally relevant, this choice of parameters allows us to estimate the effect of the multiple superconducting layers using perturbation theory. Here we use the form of the FF order parameter that has the same momentum over the entire superconductor, which we refer it as the 'homogeneous FF'. We find that the energy gain of having the FF ground state quickly decays as N_{layer} increases. Fig. 3.4 (a) shows a steady decrease in ΔE and the full BCS pairing becomes more favored as N_{layer} increases. The critical thickness where the FF and BCS ground state energy meet equal is also dependent on the coupling strength, t_c, between the TI and the superconductor, and larger t_c can sustain FF superconductivity in more metallic layers. This can be understood from the enhancement of the IPE when t_c increases. Moreover, regardless of the value of t_c, we find that the same rate in the decrease of ΔE as N_{layer} increases. This is due to the fact that the energy loss of having the FF pairing in the additional layers of the superconductor is simply proportional to the number of the layers. As a result, the energetic cost of having the FF pairing in the spin-orbit free superconducting layers increases with N_{layer}, where we expect a linear relationship between ΔE and N_{layer}. Furthermore, Fig. 3.4 (b) shows ΔE when $t_c < t_m$. In this case, we cannot argue the multi-layer effect using the perturbation theory. Accordingly, we lose simple linear dependence of the energy as shown in Fig 3.4 (a) when N_{layer} is small. Nevertheless, the overall trend of decreasing ΔE as a function of N_{layer} still holds.

In addition to the homogeneous FF order parameter over the entire region of the superconductor(homogeneous FF), we now postulate an additional form of the FF order parameter in which the finite momentum of the cooper pairs only survives near the interface region(interface FF). The inferface FF is defined as the order parameter profile with the momentum of the cooper pair q that exists only within the first layer of the superconductor. The interface FF becomes more energetically favored than the homogeneous FF in the thick superconductor limit as the additional energy cost of having FF phase in the upper metallic region without spin-orbit coupling is no longer considered. This effect is numerically supported in Fig. 3.4 (c). The Fig. 3.4 (c) shows the energy difference as a function of the thickness and t_m, and we find that the energy difference saturates as N_{layer} becomes larger than two. As the interface FF does not distinguish the upper layers of the superconductor from the BCS superconductivity, the resulting energy difference saturates with increasing numbers of superconducting layers. Interface becomes energetically advantageous as the homogeneous FF costs a constant amount of energy as the thickness of the superconductor increases. In addition to the thickness dependence, the interface FF has additional dependence on t_m. As we increase the values of t_m, the energetic difference proportionally increases in the interface FF. This is due to the increased Josephson energy between the interface and the upper layer of the superconductor. In other words, there is a cost of energy associated with the large gradient of order parameter when the momentum of the order parameter rapidly decays. It is important to note that, in order to find the global minima of the ground state energy, the ground state energy of all the possible FF momenta in each layer must be compared. In this work, we postulate the interface FF and the homogenous FF as examples of the FF order parameter profile that might become more stable than the BCS pairing.

3.5 Transport measurement

3.5.1 Four terminal Josephson junction

In the previous sections, we analyzed the stability of the FF pairing. In this section, we now propose a Josephson junction transport and compare the transport signatures of the three different pairing scenarios: the conventional BCS phase, the homogeneous FF phase, and the interface FF phase. Fig 3.5 (a) shows the schematic figure of the transport configuration which consists of a Josephson junction between the TI-SC heterostructure and the conventional BCS superconductor separated by normal insulator. On the top of the superconductors we attach the four transport terminals through which current is injected or extracted. The two terminals are attached on the top of the two different superconductors so that the two junction can have a different phase of the superconducting order parameter by either applying the voltage bias or

external current, I_J. The other two contacts are attached on the top of the BCS superconductor to drive the current in the perpendicular direction(I_{per}) of the Josephson junction.

After establishing the setup of the Josephson junction, we now explain the manner in which current flows in this Josephson junction. Our setup utilizes the mismatch of the order parameter wave function on the interface between the BCS pairing and the FF pairing, this method has been similarly proposed to measure the LO state in the bulk doped inversion symmetric Weyl semi-metal[3]. We first consider the weak coupling regime of the junction where the normal insulator is thick enough so that the Josephson current between the BCS and the FF superconductor can be approximated as,

$$max(I_J) \approx t_j \int d^2x \Delta_{top}(x)^* \Delta_{bottom}(x), \tag{3.21}$$
$$I_J(\phi) \approx max(I_J) sin(\phi).$$

where t_j is the coupling strength between the junction. Δ_{top} and Δ_{bottom} is the order parameter wave function of the top and bottom superconductor respectively. The integration indicates the sum over the two dimensional junction region. As can be seen from Eq. (3.21), the Josephson current is strongly suppressed when there exists a spatial interference pattern in the inner product of the order parameters of the two superconductor. As a result, the intrinsic spatial oscillations of the FF order parameter(i.e. $\Delta_{bottom} \approx |\Delta| e^{iqx}$) strongly suppress I_J when it is coupled to BCS superconductor(i.e. $\Delta_{top} \approx |\Delta|$) in equilibrium. However, when I_{per} is applied to the BCS superconductor, the BCS Cooper pairs possess the finite net momentum, resulting in the form of the order parameter, $\Delta_{top} = |\Delta| e^{iq_{per}x}$. The current induced spatial oscillations of the order parameter can cancel the oscillatory component of the FF order parameter in Eq. (3.21) when $q_{per} = q$, and recover I_J. Due to this momentum mismatch between the two superconductors, the Josephson junction between the FF state and the BCS state have a maximum of $max(I_J)$ under the non-zero parallel current, I_{per}, while the junction made with the two BCS superconductor always have a maximum in the absence of the parallel current.

We now illustrate this idea discussed above by numerically calculating the Josephson current in the proposed device structure. In this calculation, we model the normal insulator barrier using a small coupling strength t_J between the superconductors. We also model I_{per} by adding the finite momentum ,q_{per}, in the order parameter of the BCS superconductor. The Josephson current can be calculated from the full energy spectrum of the bound state in the junction by using the following formula[96]

$$J(\phi) = \frac{\partial E_{ground}(\phi)}{\partial \phi} \tag{3.22}$$

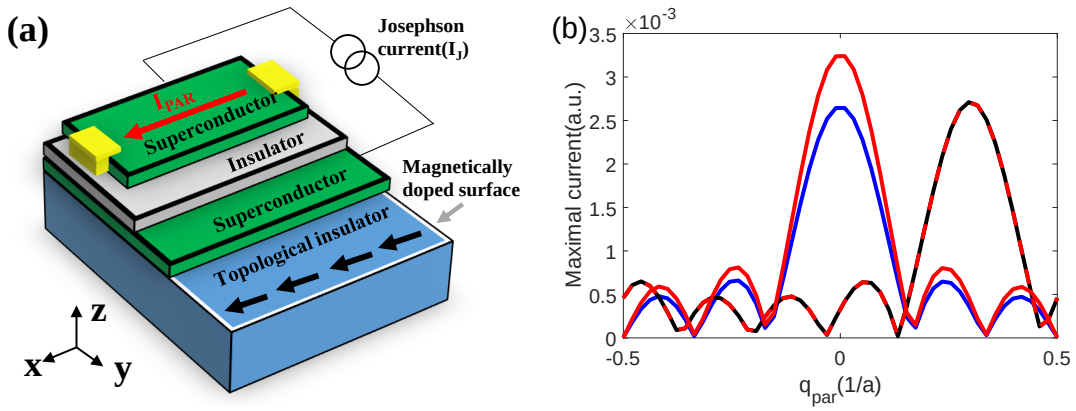

Figure 3.5: (a) The schematic figure of the Josephson junction setup. On the top of the magnetically doped TI-superconductor junction, the normal insulator barrier is deposited, and the another superconductor is placed on the top of the normal insulator. The four terminal current is placed on the top of the superconductors. The two are attached on the different superconductors to drive the Josephson current. The other two are attached on the top BCS superconductor to drive the current in a direction parallel to the FF momentum. (b) Numerically calculated Josephson current as a function of the transverse momentum q_{per}. The blue, the black, and the red lines represent the Josephson current in the BCS pairing, the homogeneous FF pairing and the interface FF pairing respectively. We find that the blue(BCS) line has the maximum located at the $q_{per} = 0$ and the black(homogenous FF) line has the maximum located at the $q_{per} = q = 0.3$. The red(interface FF) line which has the peak at the $q_{per} = 0$ are the interface FF phase with $N_{Layer} = 2$. Adapted from [2].

where ϕ is the phase difference between the two superconductors. E_{ground} is the ground state energy. By explicitly sweeping ϕ from 0 to 2π, we derive the amplitude of the Josephson current as given in Eq. (3.21). Fig. 3.5 (b) shows the amplitude of the numerically calculated Josephson current as a function of I_{per} in the case of the three different scenarios of the superconducting order parameter. First of all, the blue curve shows the current in the case of the BCS pairing. As explained above, we find that the maximum of the current occurs in equilibrium when $q_{per} = 0$ and the addition of the transverse current strongly suppresses the Josephson current as it introduces an additional spatial variation in the order parameter products. Unlike the case of the BCS superconductor, shown by the black lines, which shows the Josephson current in the BCS-FF case, has a maximum in the presence of non-zero parallel current which cancels the intrinsic spatial variation of the FF superconducting order parameter. As long as the FF state persists we find that this non-trivial Josephson current serves as an important signature that is distinguished from the conventional BCS pairing. Further, the red lines shows the transport of the interface FF pairing. Unlike the BCS and FF order parameter, we now find a crossover in the location of the maximum current layer increases. In the single layer limit, we find the maximum of the current occur in the same position as FF phase. However, as the N_{Layer} increases more than two, we find that the current pattern resembles the BCS phase, since the interface FF has identical order parameter to the BCS order parameter on the top. This shows that

the Josephson current is only sensitive to the form of the order parameter near the junction region and the interface FF shows the distinct signature of the FF phase only in the thin superconductor limit.

3.5.2 Y junction

Another useful experimental method to detect FF phase is Andreev interferometer[97]. Fig. 3.6 (a) shows the Andreev interferometer with the Y-junction with two arms separated by L_x in $\hat{x}$ direction placed on the top of the superconductor. In the presence of the magnetization vector, $\mathbf{m} = |m|(sin\theta, cos\theta)$ on the TI surface, our analysis shows that the FF phase with the momentum vector, $\mathbf{q} = |q|(cos\theta, sin\theta) \perp \mathbf{m}$, is induced. In this case, the superconducting order parameter at each contact has different phases due to the phase modulation resulting from the finite longitudinal separation with respect to the momentum of the FF phase, q. We parameterize the different phases by assigning the order parameters $|\Delta|e^{-i\mathbf{q}x_1}$ and $|\Delta|e^{-i\mathbf{q}x_2}$ at the upper and the lower contacts respectively, where x_1 and x_2 are the coordinates of the upper and lower contacts. The phase difference between the two contacts is given as $\Delta\phi = q(x_1 - x_2)cos\theta = |q|L_x cos\theta$. When the current flows through the Y-junction, the electrons injected from lower and the upper contacts undergo Andreev reflection process and reflected as holes. Due to the presence of the FF order parameter, the holes gain additional phases of either $\Delta e^{-iq_x x_1}$ or $\Delta e^{-iq_x x_2}$ depending on whether it is reflected from the upper or the lower contacts that comprise the Y-junction. The generation of this additional phase can be understood from an examination of the pairing Hamiltonian, $H_{pairing}(x) = \Delta e^{-iq_x x} c_x i\sigma_y c_x + h.c.$, at the interface between the contact, which annihilates a electron and create a hole with an additional phase of $\Delta e^{-iq_x x}$. Eventually, when the holes are collected to the central branch of the Y junction, the phase difference between different contacts generates an interference pattern as a function of $\Delta\phi \approx cos\theta$ and, most importantly, when $|q|L_x cos\theta = \pi$, destructive interference occurs and the conductance vanishes.

To illustrate the qualitative behavior of the Y-junction Andreev interferometer, we use the metallic Hamiltonian in Eq. (3.1) with assumed FF superconducting order. The conductance is obtained from Blonder-Tinkham-Klapwijk theory[98] with an assumed interface barrier height that is transparent [97].The outermost line (Green solid line) in Fig. 3.6b shows the conductance with no finite momentum in the superconducting system, or $\mathbf{q} = 0$. The conductance shows a uniform distribution whereas we observe non-uniform conductance oscillation for $Q > 0$. The innermost line (Red solid line) in Fig. 3.6 (b) shows $q_x = \pi/L_x$ where the phase difference between two arms is $q_x L_x = \pi \cos\theta$, and the conductance shows a destructive interference at $\theta = 0$ and π. Consequently, the signature of the conductance oscillation in Y-junction is a direct result of spatially varying nature of the order parameter. In addition, the Andreev interferometer is an optimal scheme for our proposal as one can adjust the angle of the finite momentum

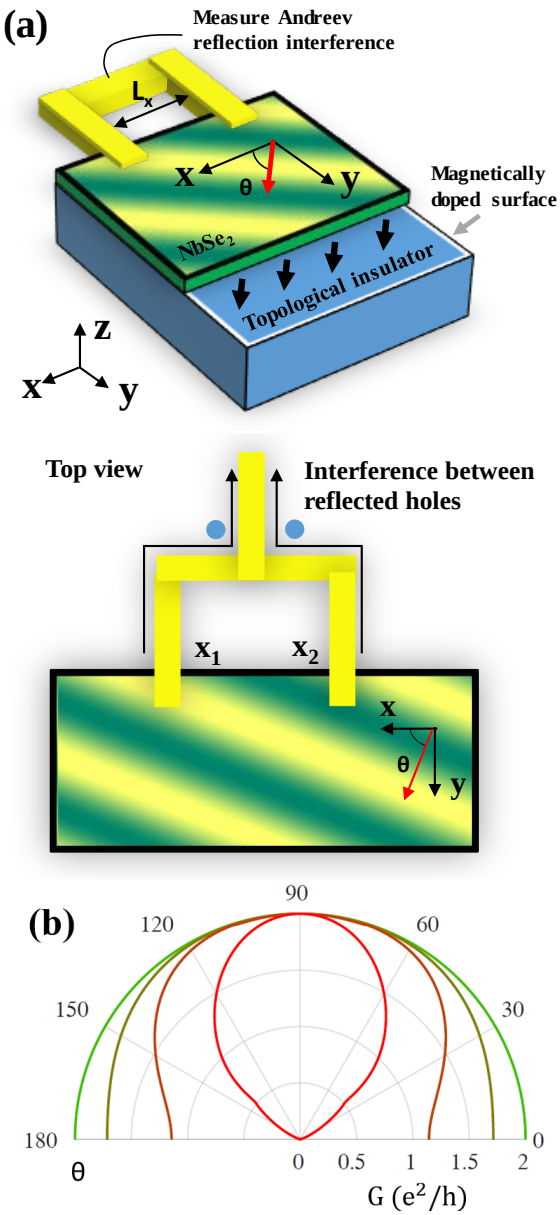

Figure 3.6: (a) A schematic of the Andreev interferometer using Y-junction method to measure the unconventional superconductivity. (b) A plot of conductance as a function of finite momentum angle, θ, of the FF phase. From the outermost to innermost, we plot the calculation results with different $\mathbf{q}$ where $|q| = 0,\ \pi/8,\ \pi/6, and\ \pi/4$, respectively. We use a value of $v_F = 6.61 \times 10^5$ m/s for the Fermi velocity, that has been extracted from the metal Hamiltonian parameter, and plot the conductance at the incident electron the energy of $E = 0.5\Delta$, where the Δ is superconducting gap. We set the barrier height at the interface of the metal arms and superconductor to be transparent. Adapted from [2].

(θ) before each transport measurements by applying in-plane magnetic field to adjust the orientation of the magnetic dopants rather than needing to fabricate different devices or multiple Y-junctions. However, it is important to note that that the minimum momentum shift required to observe a clear destructive

interference pattern is either $q = \pi/L_x$ or L_x and that this quantity needs to be chosen within the scope of the maximum Q that can be realized by the magnetic doping on the TI surface.

3.6 Conclusion

In conclusion, we have studied the stability of the FF phase in magnetically doped TI-BCS superconductor heterostructures. We find that the FF state can be more energetically favorable than the traditional BCS pairing. This is due to the anisotropy of the Fermi surface in the superconductor that arises from the IPE where the normal bands of the superconductor near the interface have an effective spin-orbit coupling and Zeeman field. We find that the IPE quickly decays as the coupled state moves farther away from the interface into the bulk of the superconductor. As a consequence, the FF state gains more energy as the thickness of the superconductor increases and the stability of the FF state quickly decays. Nevertheless, in the thick superconductor limit, we find the FF phase can survive at the interface of the proximity structure. We expect the FF pairing in our proposal can be experimentally measured through the four probe transport experiment utilizing a Josephson junction or through the Y-junction method.

Chapter 4

Unconventional superconductivity in inversion symmetric Weyl semimetal

[1]

4.1 Introduction

In the previous chapters of this thesis, we have found that the relativistic Dirac fermion on the surface of the 3D topological insulator harbors the unconventional superconducting states. This analysis can be further generalized to the relativistic quasi-particles in the three dimensions. In general, the three dimensional Dirac fermions can be found in the bulk of the topological semimetals. We now turn our attention to the unconventional superconductivity in the Weyl semimetal.

Intensive studies in the field of topological phases of matter has extended the scope of our understanding from fully gapped insulator to gapless semimetals[56, 99, 100]. An example of which is the Weyl semimetal (WSM), whose low energy excitations are described by three-dimensional Weyl fermions[56, 99]. The WSM is characterized by its non-degenerate band crossing points referred to as Weyl nodes, where the valence and conduction band touch. Weyl nodes are monopoles of the Berry curvature in momentum space[101, 56] and the Fermi surface (FS) enclosing the Weyl node is topologically non-trivial as it carries monopole charge (or Chern number). Weyl nodes with opposite monopole charge appear in pairs in the lattice[102, 103] and the pairs of Weyl nodes are responsible for emergent phenomena such as Fermi arcs[99, 104, 105] and unconventional electromagnetic responses such as negative magneto-resistance and chiral magnetic effect[106].

The unique physics of WSM motivates further research on one of the most striking differences between semimetals and insulators; the *intrinsic* superconducting phases in doped semimetal. Unconventional superconductivity has been shown to arise from the interplay between topologically non-trivial states and superconducting phases of doped WSM[107, 108, 109]. Specifically, as FS enclosing Weyl nodes must appear in even number[102, 103], doped WSM facilitates two types of possible superconducting pairings: inter-node

[1] Portions of this study were previously published as [3] and reprinted with permission (Copyright 2016 by American Physical Society).

and intra-node pairing. When Weyl nodes with opposite monopole charge are mapped to each other by inversion symmetry, the inter-node pairing exhibits nodal BCS pairing state whose electrical structure is in a close analogy with the ^{3}He-A phase[107, 110, 111]. On the other hand, the intra-node pairing forms finite momentum carrying superconducting states[107] known as the Fulde-Ferrell-Larkin-Ovchinnikov (FFLO) states[112, 113]. While both types of superconducting states are possible, different analysis methods yield different energetically preferred pairing states[107, 108]. Assuming even parity pairing (singlet) states in low-energy chiral basis, mean-field calculations show that FFLO pairing is favored[107]. On the contrary, when one considers odd parity pairing (triplet), a short- and long-range attractive interaction results in FFLO and BCS pairing states as ground states, respectively. In the weak-coupling regime, BCS states are energetically preferred, however, FFLO states may have lower energy in the absence of both inversion and time-reversal symmetry, due to the fact that FFLO states rely on low-energy chiral symmetry while electrons in the BCS states are connected either by inversion or time-reversal symmetry[108].

Although finding energetically preferred pairing is crucial to clarify microscopic details of the superconductivity, it is unclear how to determine a pairing scheme for a given doped WSM. In this regards, we propose a quantum transport method to elucidate the pairing states in doped WSM. More precisely, we focus our discussion on inversion symmetric doped WSM and on two possible unconventional superconducting states: FFLO and nodal BCS states. To identify two seemingly distinct superconducting states, we propose two complementary transport methods. we introduce a Josephson junction comprised of a doped WSM and a conventional s-wave superconductor in weak coupling regime to resolve the FFLO states. We find that the Josephson current is averaged out to be vanishingly small due to the spatially oscillating order parameter of FFLO states. By driving transverse supercurrent in s-wave superconductor, we show that non-equilibrium s-wave pairing states mimic FFLO states and the Josephson current is restored at finite transverse current, which serves as a signature for FFLO pairing in doped WSM.

4.2 System description

In Fig. (4.1), we consider a Josephson junction that consists of a doped WSM (H_L) weakly coupled with a conventional s-wave superconductor (H_R). When the system is in the superconducting regime, a Josphson current flows in longitudinal ($\hat{x}$) direction, as shown by the blue dashed arrow in Fig. (4.1), across the junction located at $x = x_0$. The doped inversion symmetric WSM system in this work has two Weyl nodes located at $\pm\mathbf{Q}$ in momentum space. Assuming inter-node pairing, a Cooper pair that shares a FS with momenta $\pm\mathbf{Q}+\mathbf{k}$ and $\pm\mathbf{Q}-\mathbf{k}$ forms an FFLO state[107]. Therefore, a net momentum of $\pm 2\mathbf{Q}$ is carried by

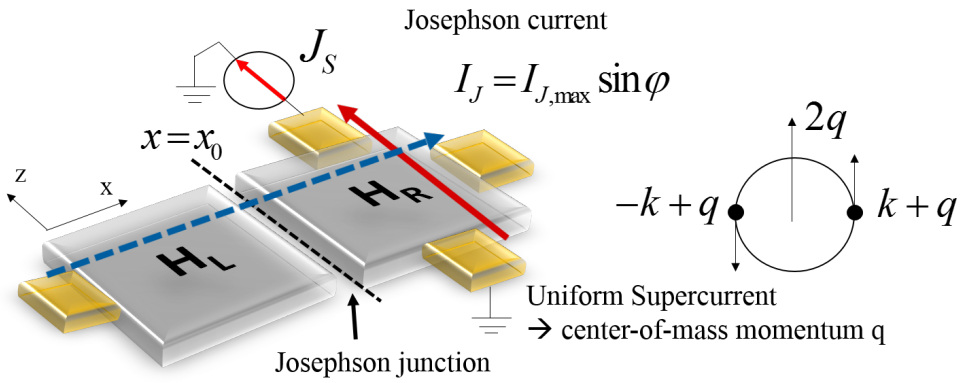

Figure 4.1: A schematic of the system. H_L is a WSM and H_R is an ordinary metal superconductor. A weak coupling between H_L and H_R is assumed. A Josephson current flows in $\hat{x}$ direction (blue dashed arrow) and a uniform supercurrent in $\hat{z}$ direction (red solid arrow) gives center-of-momentum q to the H_R system. Adapted from [3].

the pairing states and the order parameter of the FFLO states has a form $\Psi_L(\mathbf{r}) = \psi_L(e^{i2\mathbf{Q}\cdot\mathbf{r}} + e^{-i2\mathbf{Q}\cdot\mathbf{r}})$ in real space, where ψ_L is an amplitude of the order parameter[112, 113]. Assuming uniform BCS pairing for the s-wave superconductor, the superconducting order parameter is $\Psi_R(\mathbf{r}) = \psi_R$ and the total Josephson current may be determined as[114]

$$I_J \propto \mathrm{Im}\left[\psi_L\psi_R \int d^2\mathbf{r} e^{i(2\mathbf{Q}\cdot\mathbf{r}+\delta\varphi)} + e^{i(-2\mathbf{Q}\cdot\mathbf{r}+\delta\varphi)}\right], \tag{4.1}$$

where $\delta\varphi$ is relative phase difference of two superconducting systems, and the integral covers the entire interface of the Josephson junction. In Eq. (4.1), I_J vanishes as one integrates over $\mathbf{r}$ due to the spatially oscillating FFLO state order parameter. However, previous work[114] shows that one may effectively cancel the finite momentum $\mathbf{Q}$ by introducing external magnetic field and, as a result, the Josephson current is restored. Although the non-zero Josephson current under applied magnetic field can be utilized to identify FFLO states, the same proposal may not be applicable in the WSM. In the presence of a magnetic field, the low energy Hamiltonian of WSM leaves only 1D chiral mode in the lowest Landau level[115] and, therefore, the intra-node coupling cannot occur. To overcome this situation, we show that a driven supercurrent plays the role of the magnetic field.

In the presence of a uniform supercurrent of s-wave superconductor, as depicted in Fig. (4.1) by the red solid arrow, a Cooper pair aquires a finite center-of-mass momentum $\mathbf{q}$. Then electrons at $\mathbf{k}+\mathbf{q}$ and $-\mathbf{k}+\mathbf{q}$ constitute a Cooper pair with a net momentum of $2\mathbf{q}$. As a result, the s-wave pairing states under non-equilibrium effectively mimic finite-momentum carrying FFLO states with the order parameter[67, 53] $\Psi_R = \psi_R e^{i2\mathbf{q}\cdot\mathbf{r}}$. Especially, when the momentum $\mathbf{q}$ is parallel to and in a resonance with $\mathbf{Q}$ carried by

the FFLO states, the Josephson junction has a non-vanishing I_J, which may serve as a signature of FFLO states in doped WSM. In above scenario, a uniform transverse current, $\mathbf{J}_S$, is carried by Cooper pairs with finite net momentum $2\mathbf{q}$, as indicated by the red solid arrow in Fig. (4.1). $\mathbf{J}_S$ increases linearly as a function of $\mathbf{q}$ both in the conventional s-wave[116] and unconventional nodal superconductor[117] until $\mathbf{J}_S$ reaches a critical current, or the superconducting phase becomes unstable. However, we assume that $\mathbf{J}_S$ is small compared to the critical current, therefore, the supercurrent is proportional to $\mathbf{q}$ (see supplementary material for the calculation of J_S as a function of q). Therefore, we utilize $\mathbf{q}$ as a key parameter to describe non-equilibrium states of the superconductor system and plot our main results as a function of $\mathbf{q}$ instead of $\mathbf{J}_S$.

We begin by considering a model lattice Hamiltonian

$$H = H_L + H_R + H_T, \tag{4.2}$$

where H_L is a doped WSM system and H_R is a metallic s-wave system as depicted in Fig. (4.1). We assume both of the systems are in superconducting phase and they are weakly coupled by a tunneling Hamiltonian, H_T. We discretize the system in longitudinal ($\hat{x}$) direction in order to consider a Josephson junction at $x = x_0$ with the tunneling Hamiltonian

$$H_T = \sum_{\mathbf{k},\mathbf{p}} t_{\mathbf{k},\mathbf{p}} (c^\dagger_{\mathbf{k}}(x_0) c_{\mathbf{p}}(x_0) + h.c.), \tag{4.3}$$

where $c^\dagger_{\mathbf{k}}$ is electron creation operator of system H_L, $c_{\mathbf{p}}$ is annihilation operator of system H_R, $t_{\mathbf{k},\mathbf{p}}$ is a tunneling constant, and $\mathbf{k}$, $\mathbf{p} = (k_y, k_z)$ are momentum of transverse directions. Here, we assume that the tunneling constant is non-zero only at the interface ($x = x_0$).

For the doped WSM system, we choose a model Hamiltonian which breaks time reversal symmetry but preserves inversion symmetry. Near the Weyl node, we consider a minimal low-energy two-band model of the WSM[118]

$$\begin{aligned} H_w = \sum_{\mathbf{k}} \Big[& \left(M - 2 \sum_{\alpha=x,y,z} t_\alpha \cos k_\alpha \right) \sigma_z \\ & + 2\lambda \left(\sin k_x \sigma_x + \sin k_y \sigma_y \right) - \mu_L \mathbb{I} \Big], \end{aligned} \tag{4.4}$$

where $\sigma_{x,y,z}$ are the Pauli matrices for spin, $\mathbb{I}$ is the identity matrix, λ is a hopping term in $k_x - k_y$ plane, and μ_L is the chemical potential in the WSM. In this work, we use a lattice constant of $a = 1$ and set $\hbar = 1$. In Eq. (4.4), $t_{\alpha=x,y,z}$ is a mass term which determines the position of the Weyl nodes in momentum

space. The time-reversal breaking mass term $M = 2t_x + 2t_y + m$ separates Weyl nodes in the system and we set $m = 2t_z \cos Q$ so that two Weyl nodes are located at $\pm\mathbf{Q} = (0, 0, \pm Q)$ along the z axis with opposite monopole charge. Assuming FFLO pairing, we consider an attractive Hubbard type interaction. The mean-field approximation for the interaction Hamiltonian is

$$H_{FFLO} = \sum_{\mathbf{k}} [\Delta_{L1} c^{\dagger}_{\mathbf{k},\uparrow} c^{\dagger}_{-\mathbf{k}+2\mathbf{Q},\downarrow} + \Delta_{L2} c^{\dagger}_{\mathbf{k},\uparrow} c^{\dagger}_{-\mathbf{k}-2\mathbf{Q},\downarrow} + h.c.]. \tag{4.5}$$

where the first (second) term couples electrons in FS enclosing the Weyl node located at $k_z = +Q$ $(-Q)$ with a uniform pairing potential Δ_{L1} (Δ_{L2}). To see the finite size effect of the junction, we discretize the Hamiltonian in transverse $(\hat{z})$ direction. Therefore, the Hamiltonian of Eqs. (4.4) and (4.5) is discretized in transverse $(\hat{z})$ and longitudinal $(\hat{x})$ direction in real space. As a result, the Bogoliubov-de Gennes (BdG) Hamiltonian is

$$\begin{aligned} H_L = &\sum_{\mathbf{r},k_y} \mathbf{\Phi}^{\dagger}_{r,k_y} \begin{pmatrix} \tilde{H}_w(k_y) & \tilde{H}_{FFLO}(\mathbf{r}) \\ \tilde{H}^{\dagger}_{FFLO}(\mathbf{r}) & -\tilde{H}^{*}_{w}(-k_y) \end{pmatrix} \mathbf{\Phi}_{r,k_y} \\ &+ \sum_{\mathbf{r},\alpha,k_y} \left[\mathbf{\Phi}^{\dagger}_{r,k_y} \begin{pmatrix} \tilde{H}_{w,\alpha} & 0 \\ 0 & -\tilde{H}^{*}_{w,\alpha} \end{pmatrix} \mathbf{\Phi}_{r+\alpha,k_y} + \text{h.c.} \right], \end{aligned} \tag{4.6}$$

where $\mathbf{\Phi}_{r,k_y} = [c_{\mathbf{r},k_y,\uparrow}, c_{\mathbf{r},k_y,\downarrow}, c^{\dagger}_{\mathbf{r},-k_y,\uparrow}, c^{\dagger}_{\mathbf{r},-k_y,\downarrow}]^T$, $\mathbf{r} = (x, z)$, and $\alpha = \delta x, \delta z$. The individual components of discretized Hamiltonian are

$$\begin{aligned} &\tilde{H}_w(k_y) = [M - 2t_y \cos(k_y a)]\sigma_z + 2\lambda \sin(k_y a)\sigma_y - \mu_L \mathbb{I}, \\ &\tilde{H}_{w,\delta x} = -i\lambda\sigma_x - t_x\sigma_z, \ \tilde{H}_{w,\delta z} = -t_z\sigma_z, \\ &\tilde{H}_{FFLO}(\mathbf{r}) = 2\Delta_L \cos(2Qz) i\sigma_y, \end{aligned} \tag{4.7}$$

where $\tilde{H}_{w,\delta x}$ and $\tilde{H}_{w,\delta z}$ are the nearest neighbor hopping Hamiltonian in the $\hat{x}$ and $\hat{z}$ direction, respectively, and $\tilde{H}_{FFLO}(\mathbf{r})$ is the superconducting interaction Hamiltonian Fourier transformed to real space. Note that we assume identical pairing potential for each FS, $\Delta_{L1} = \Delta_{L2} = \Delta_L$, but following arguments are valid regardless of this assumption.

With the Weyl Hamiltonian defined, we consider a normal metal Hamiltonian defined as

$$H_m = \sum_{\mathbf{k}} (-t_m(\cos k_x + \cos k_y + \cos k_z) - \mu_R)\mathbb{I}, \tag{4.8}$$

where t_m is a hopping term and μ_R is the chemical potential. In our system, the Cooper pairs in the BCS

superconductor aquire $\mathbf{q} = q\hat{z}$ through the application of a uniform supercurrent[67, 53] in transverse ($\hat{z}$) direction, as indicated in red solid arrow in Fig. (4.1). Then the mean-field approximation to the interaction Hamiltonian is

$$H_{BCS} = \sum_{\mathbf{k}} [\Delta_R c^\dagger_{\mathbf{k}+\mathbf{q}\uparrow} c^\dagger_{-\mathbf{k}+\mathbf{q}\downarrow} + h.c.], \tag{4.9}$$

where Δ_R is a uniform BCS pairing potential. The BdG Hamiltonian is constructed for H_R in a similar manner to Eq. (4.6) and discretized in the transverse ($\hat{z}$) and longitudinal ($\hat{x}$) directions. Consequently,

$$\begin{aligned} H_R(q) = &\sum_{\mathbf{r},k_y} \mathbf{\Phi}^\dagger_{r,k_y} \begin{pmatrix} \tilde{H}_m(k_y) & \tilde{H}_{BCS}(\mathbf{r},q) \\ \tilde{H}^\dagger_{BCS}(\mathbf{r},q) & -\tilde{H}^*_m(-k_y) \end{pmatrix} \mathbf{\Phi}_{r,k_y} \\ &+ \sum_{\mathbf{r},\alpha,k_y} \left[\mathbf{\Phi}^\dagger_{r,k_y} \begin{pmatrix} \tilde{H}_{m,\alpha} & 0 \\ 0 & -\tilde{H}^*_{m,\alpha} \end{pmatrix} \mathbf{\Phi}_{r+\alpha,k_y} + \text{h.c.} \right], \end{aligned} \tag{4.10}$$

where the discretized Hamiltonians are

$$\begin{aligned} &\tilde{H}_m(k_y) = (-t_m \cos k_z - \mu_R)\mathbb{I}, \\ &\tilde{H}_{m,\delta x} = -(t_m/2)\mathbb{I},\ \tilde{H}_{m,\delta z} = -(t_m/2)\mathbb{I}, \\ &\tilde{H}_{BCS}(\mathbf{r},q) = \Delta_R e^{i2qz} i\sigma_y. \end{aligned} \tag{4.11}$$

Here, $\tilde{H}_{m,\delta x}$ and $\tilde{H}_{m,\delta z}$ are the nearest neighbor hopping Hamiltonian and $\tilde{H}_{BCS}(\mathbf{r},q)$ is the interaction Hamiltonian Fourier transformed to real space.

4.3 Probing FFLO state using Josephson current

Having defined lattice Hamiltonian for $H_{L/R}$, we may calculate the Josephson current between the doped WSM and s-wave superconductor. Assuming a weak coupling limit, the tunneling Hamiltonian H_T in Eq. (4.3) can be treated as a perturbation. From the Ginzburg-Landau theory, we may determine the Josephson current[114]

$$I_J = \text{Im}\left[t_c \int d\mathbf{r}^2_\parallel \Psi^\dagger_{BCS}(\mathbf{r}_\parallel) \Psi_{FFLO}(\mathbf{r}_\parallel) \right], \tag{4.12}$$

where t_c is a coupling constant, Ψ_{BCS} and Ψ_{FFLO} are order parameters of s-wave superconductor and doped WSM system, respectively. The integration in Eq. (4.12) is performed over the interface of the Jospehson junction $\mathbf{r}_\parallel = (x_0, y, z)$, whose longitudinal ($\hat{x}$) direction is fixed at the junction position $x = x_0$. Once we put two superconductors together, the order parameters may differ in phase by $\delta\varphi = \varphi_L - \varphi_R$. Taking account

the phase difference, the order parameters in Eq. (4.12) are rewritten as $\Psi_{FFLO} = \Psi_L(\mathbf{r}_\parallel)e^{i\varphi_L}$ and $\Psi_{BCS} = \Psi_R(\mathbf{r}_\parallel, q)e^{i\varphi_R}$, where Ψ_L and Ψ_R are the order parameters of doped WSM and s-wave superconductor, respectively. Note that the order parameters Ψ_L and Ψ_R are calculated in *isolated* system as the tunneling Hamiltonian is treated perturbatively. Then, Eq. (4.12) is rewritten as

$$\begin{aligned} I_J =& \mathrm{Im}\left[t_c \int d^2\mathbf{r}_\parallel \Psi_R^\dagger(\mathbf{r}_\parallel, q)\Psi_L(\mathbf{r}_\parallel)e^{i\delta\varphi}\right] \\ =& \mathrm{Im}\left[I_{J,max}(q)e^{i\varphi(q)}e^{i\delta\varphi}\right] \\ =& I_{J,max}(q)\sin(\varphi(q)+\delta\varphi), \end{aligned} \tag{4.13}$$

where $I_{J,max}$ and $\varphi(q) + \delta\varphi$ are the amplitude and phase of the Josephson current, I_J. We immediately notice that the Josephson current amplitude, $I_{J,max}$, is a function of momentum q. As it is shown in Eq. (4.7), the interaction Hamiltonian of doped WSM oscillates spatially which manifests as a spatial oscillation in the order parameter Ψ_L. As a result, $I_{J,max}$ is spatially averaged out and its magnitude vanishes for a sufficiently wide interface ($\gg 1/Q$) at $q = 0$. The situation, however, may be different when a Cooper pair in s-wave superconductor acquires center-of-mass momentum q by a driven current. The order parameter Ψ_R effectively mimics FFLO states with non-zero momentum q to cancel out the relative spatial variation and, at $q = \pm Q$, $I_{J,max}$ is restored. To evaluate $I_{J,max}$, we take a Fourier transform of both order parameters $\Psi_{L/R}$ in $\hat{y}$ direction

$$\begin{aligned} I_{J,max}(q) &= \left|t_c \int d^2\mathbf{r}_\parallel \Psi_R^\dagger(\mathbf{r}_\parallel, q)\Psi_L(\mathbf{r}_\parallel)\right| \\ &= \left|t_c \int dz \int \frac{dk_y}{2\pi}\Psi_R^\dagger(\mathbf{r}_0, k_y, q)\Psi_L(\mathbf{r}_0, k_y)\right|, \end{aligned} \tag{4.14}$$

where $\mathbf{r}_0 = (x_0, z)$. Then the Hamiltonians in Eqs. (4.6) and (4.10) are diagonalized and the order parameters $\Psi_L(\mathbf{r}, k) = \langle c_{\uparrow,\mathbf{r},k}c_{\downarrow,\mathbf{r},-k}\rangle_L$ and $\Psi_R(\mathbf{r}, k, q) = \langle c_{\uparrow,\mathbf{r},k}c_{\downarrow,\mathbf{r},-k}\rangle_R$ are evaluated. In Fig. (4.2), we plot $I_{J,max}$ calculated from Eq. (4.14). We see a clear peak in $I_{J,max}$ at $q = \pm Q$ where the momentum q in BCS superconductor cancels the momentum Q carried by FFLO states in WSM. The oscillations in $I_{J,max}$ are due to the finite size of the lattice having an insufficient sampling of k-space. The width of the peak is decreased as we increase the resolution of the momentum space by increasing the system size. The peak is ideally a delta function at $q = \pm Q$ if the junction size is large enough to satisfy $\Delta k = 2\pi/L_z \ll Q$. In the presence of weak disorder, the peak may be shifted as disorder renormalizes mass term of WSM Hamiltonian[119], but persist as the FFLO states discussed here is robust to impurity scattering[107]. Therefore, the Josephson current amplitude at non-zero transverse ($\hat{z}$) current ($q \neq 0$) may serve as a signature of FFLO states for

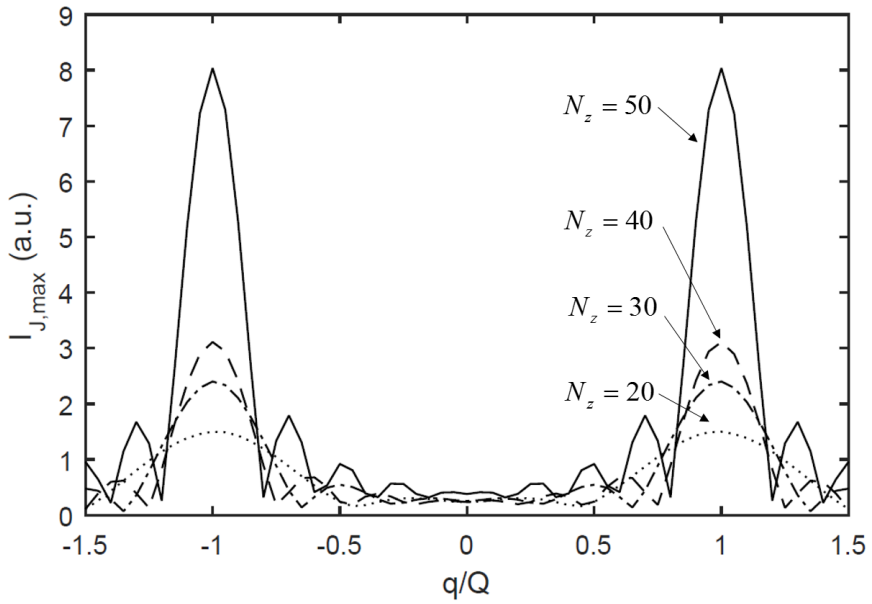

Figure 4.2: Plot of Josephson current maximum $I_{J,max}$ in Eq. (4.14) as a function of momentum, q, in the BCS superconductor as described by H_R. There are two clear peaks when the q matches with the $\pm Q$ in doped WSM described by H_L. The parameters $t_m = 1, \mu_R = 0$ are used for H_R and $t_x = 0.5,\ t_y = 0.5,\ t_z = 1.0,\ \lambda = 0.5,\ \mu_L/t = 0.2$, and $Q = 0.1\pi$ are used for H_L. The pairing potentials $\Delta_L/t = \Delta_R/t = 0.2$ are used and the number of points along the longitudinal direction ($\hat{x}$), $N_x = 10$, is fixed for both H_L and H_R. In order to see the finite size effect of the Josephson junction, we plot $N_z = 20$ to $N_z = 50$. Adapted from [3].

inversion symmetric doped WSM.

4.4 Conclusion

In summary, we study two complementary quantum transport methods to probe FFLO and nodal BCS states in superconducting phase of the inversion symmetric doped WSM. To identify FFLO states, we consider a Josephson junction consisting of a doped WSM and conventional s-wave superconductor. When the junction is in the weak coupling limit, the Josephson current is calculated from the order parameters in lattice Hamiltonian using Ginzburg-Landau theory. The order parameter of the doped WSM oscillates spatially due to the finite momentum, Q, carried by FFLO states that results a vanising Josephson current. By driving a uniform current in conventional s-wave superconductor, the order parameter of s-wave superconductor effectively mimics FFLO states carrying a net momentum q. When the modulated order parameter effectively cancels Q at $q = \pm Q$, a finite Josephson current is restored. Therefore, the peak in Josephson current in non-equilibrium serves as a direct signature of the presence of FFLO states in doped WSM.

Chapter 5

Disorder Induced Phase Transitions of Type-II Weyl Semimetal

[1]

5.1 Introduction

-

Disorder in solid state systems is an inevitable form of the interaction, and it limits the performace of the electronic devices. Therefore, it is important to understand the effect of the disorder in materials before considering future applications as an electronic device. In usual metallic systems, the disorder contributes to the scattering rate, and high enough disorder induces a metal-insulator transition, known as Anderson localization. This simple scenario may not be applied in considering topological materials, as disorder may renormalize the topological mass that alters the topological nature of the material[120, 121, 122, 123, 124, 125, 126]. This is due to the renomalization of the topological mass that determines the band topology. The effect of disorder within topological materials has been studied in a number of different contexts including time-reversal topological insulators[120, 121, 122, 123, 124, 125, 126], where it is shown that the symmetry preserving disorder may induce a transition between topological insulator and trivial insulator. Furthermore, symmetry preserving disorder may also induce a transition between the weak topological insulator to the strong topological insulator phases. Similarly, the effects of the disorder can be examined in the Weyl sememtals.

The most studied WSM are type-I WSM (WSM1), characterized by the presence of broken inversion or time-reversal symmetry, and type-II WSM (WSM2)[127, 21], which possess broken Lorentz invariance. Inversion broken WSM1, such as $TaAs$[128, 129], are characterized by the presence of disconnected Fermi arcs at the surface[130] that give rise to unconventional transport signatures such as quantum anomalous Hall (QAH) effect[131] and the chiral anomaly[132]. More recently, promising materials that may harbor experimental signatures of WSM2, such as $MoTe_2$ and WTe_2, have been proposed thereby bringing WSM2 closer

[1] Portions of this study were previously published as [4] and reprinted with permission (Copyright 2017 by American Physical Society).

to realization[133, 134, 135, 136]. WSM2 are characterized by an exotic hyperboloid Fermi surface, where the nodes are tilted in the BZ. Due to the tilted nodes, WSM2 exhibit transport properties that are distinct from the WSM1 including the absence of the chiral anomaly at certain magnetic field angles[137], magnetic break down resulting in a collapse of Landau levels[138], and anisotropy of the dynamical conductivity[139].

In this work, we show that WSM1 with small but non-zero tilt undergoes a quantum phase transition to WSM2 when charge and magnetic disorders are present. We illustrate this phase transition by calculating the topological mass renormalization that occurs within the first order Born approximation. We find that the topological mass is renormalized while the tilt of the Weyl cones in remains invariant. As a result, the Fermi velocity near the Weyl cone is also renormalized and leads to the possible phase transition between WSM1 and WSM2. Additionally, we confirm our results using numerical exact diagonalization of a three-dimensional tight binding model. To analyze the effect of the disorder self-energy contribution to the numerically obtained Green's function, we utilize the spectral function, which enables to understand the change of the band structure even in the presence of the disorder[140]. Furthermore, we find that the reverse transition from WSM2 to WSM1 is also possible depending on the value and sign of the topological mass. Our work reveals the rich phase diagram of WSM in the presence of disorder and will aid in the experimental characterization of WSM materials.

5.2 Tight binding model

-We begin by writing the Hamiltonian a Weyl fermion using the lowest order expansion of the momentum near the Weyl cone as,

$$H = \sum_{i,j} v_{i,j} k_i \sigma_j + \gamma_{tilt,i} k_i I_2 \tag{5.1}$$

where $v_{i,j}$ is a matrix which specifies the Fermi velocity, and $\sigma_i(I_2)$ is the i-th pauli matrix and I_2 is the 2×2 identity matrix. The second term, $\gamma_{tilt,i}$, tilts the cone in i-direction and whose presence the breaks Lorentz invariance[21]. The dispersion of the Hamiltonian in Eq. (5.1) is given as,

$$E = \gamma_{tilt,i} k_i + \sqrt{k_i v_{ij} v_{jk} k_k} \tag{5.2}$$

In this work, v is a diagonal matrix corresponding to the velocity in each direction. It should be noted that the choice of the velocity does not effect our conclusions. To consider the disorder effect, we rewrite the

Weyl Hamiltonian in the real space in lattice regularized form as,

$$H_W = H_0 + H_{tilt} \tag{5.3}$$

where H_0 is the minimal two band model of WSM1, which breaks the time-reversal symmetry[141], and may be written as

$$\begin{aligned} H_0 = t_x sin(k_x)\sigma_x + t_y sin(k_y)\sigma_y \\ +[m_0(2 - cos(k_x) - cos(k_y)) + (m_z - t_z cos(k_z))]\sigma_z. \end{aligned} \tag{5.4}$$

The second term in Eq. (5.3) is the tilt term, H_{tilt}, that breaks the Lorentz invariance can be generally written up to quadratic order in the lattice regularized form as,

$$H_{tilt} = a_{t,i} sin(k_i) I_2 + b_{t,i} cos(k_i) I_2 \tag{5.5}$$

Using Eq. (5.3), WSM2 is characterized by the choice of parameters in which the tilt within any direction dominates the Fermi velocity of H_0 near the cone, $|\gamma_{tilt,i}| > |v_i|$, where the individual tilts at the cones in the lattice Hamiltonian are given as $\gamma_{tilt} = (a_t cos(Q) \pm b_t sin(Q))$. In this model, the Weyl cones are located at $Q = (0, 0, \pm a cos(m_z/t_z))$ in the BZ and the Fermi velocity in each of the cones is given as $v_{x,y} = \frac{\partial E}{\partial k_{x,y}}|_{k=Q} = t_{x,y}$ and $v_z = t_z \frac{\partial E}{\partial k_z}|_{k=Q} = t_z sin(Q)$. m_0 gaps out the spectrum at X and Y points. Here, we choose the direction of the tilt to be in the $\hat{z}$-direction as the purpose of this work is to observe the phase transition resulting from the renormalized topological mass, m_z, in the z direction. As the goal of this work is to examine the effects of disorder on the resultant phases in WSM, a momentum space representation of the Hamiltonian is not useful as the inclusion of disorder forbids the use of a momentum space representation. Therefore, it is necesary to utilize the real space representation of the full Hamiltonian is given as,

$$\begin{aligned} H = \sum_{\delta=\hat{x},\hat{y},\hat{z}} c^\dagger_{(i,j,k)+\delta} h_\delta c_{i,j,k} + c^\dagger_{i,j,k}(2m_0\sigma_z + m_z\sigma_z)c_{i,j,k} \\ +h.c. \end{aligned} \tag{5.6}$$

where i, j, k are the coordinates corresponding to the $\hat{x}, \hat{y}, \hat{z}$ directions respectively, and $h_{(\hat{x},\hat{y})} = \frac{it_{x,y}}{2}\sigma_{x,y} - \frac{m_0}{2}\sigma_z$, $h_{\hat{z}} = -\frac{t_z}{2}\sigma_z + \frac{ia_t+b_t}{2}I_2$. In the remainder of this work, we place a tilde on the top of each parameter so as to indicate it has been normalized respect to t_z.

5.3 Phase in the clean limit

-In Fig. 5.1, we plot the phase diagram for the WSM as a function of the value of the topological mass and the tilt parameter. The phase diagram of the WSM in the clean limit is characterized by the locations of the Weyl nodes. When a non-zero m_z is present, the Weyl cones are separated in the BZ by the momentum vector $(0, 0, 2Q)$. As long as the nodes are well-separated in momentum space, the WSM phases are stable in the single particle picture. However, when the nodes with the opposite monopole charge meet one another at the same point in the BZ, they annihilate and produce a gap in the spectrum[142] resulting in an insulating phase. This transition is mathematically defined as the point in the BZ where Q is ill-defined, namely $\tilde{m}_z > 1$ and $\tilde{m}_z < -1$ as is shown in the boundary with the solid lines in Fig. 5.1. There are two distinct insulating phases: the NI phase ($\tilde{m}_z > 1$) and QAHI phase ($\tilde{m}_z < -1$). The QAHI phase can be thought as stacks of Chern insulators with a non-zero Hall conductance[141]. These two distinct phases of insulator can be heuristically understood by considering a slice of the Hamiltonian at each momentum in k_z. In this case, each slice looks like a gapped Dirac fermion except at the gapless nodes at the $(0, 0, \pm Q)$. At these points, there exists a non-zero Hall conductance in the interval of $k_z \in (-Q, Q)$, where the outside of the interval the WSM has the zero Hall conductance. As we decrease m_z, the Weyl cones shift in momentum space towards the $(0, 0, \pm\pi)$ and the region in momentum space with a non-zero Hall conductance extends. Finally, when the Weyl nodes annihilate in the momentum space at $(0, 0, \pm\pi)$ which occurs at $\tilde{m}_z = -1$, the gapped bulk is fully specified by the non-zero Hall conductance. In the opposite limit, where the nodes annihilate at $(0, 0, 0)$ for $\tilde{m}_z = 1$, the k_z region with zero Hall conductance extends. In this situation, when the nodes meet in the zero momentum space, the Hamiltonian is characterized by zero Hall conductance resulting in the NI phases.

In addition to the metal-insulator transitions, there exist WSM1-WSM2 transitions as we increase the m_z in the presence of non-zero γ_{tilt}. This phase transition occurs when the increased m_z lowers the Fermi velocity below the finite value of the tilt term, γ_{tilt}. This condition can be analytically written for our specific model as $v_f = \tilde{t}_z sin(Q) < \tilde{\gamma}_{tilt}$. In Fig. 5.1, we plot the full phase diagram of the WSM in the clean limit as a function of the value of $\tilde{\gamma}_{tilt}$ and $\tilde{m}_z$ showing the transitions between WSM1, WSM2, and insulator phases as calculated using the analysis presented.

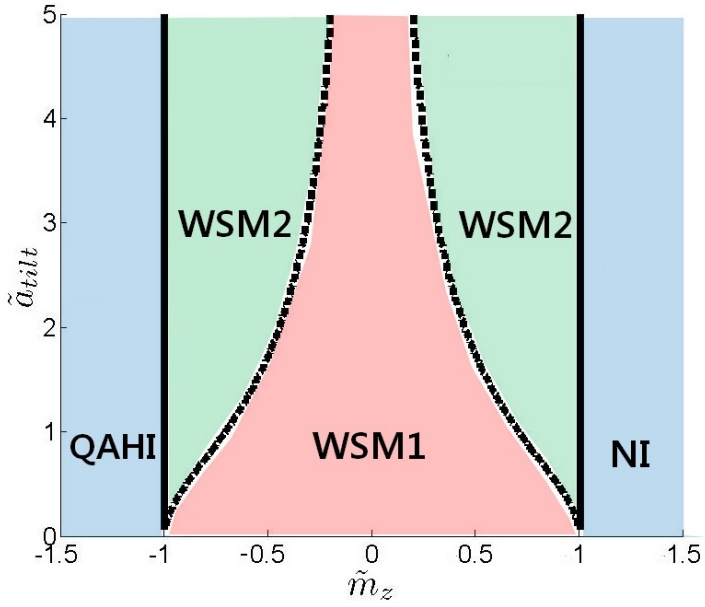

Figure 5.1: Plot of the phase diagram of the WSM in the clean limit. There are the two distinct insulating phase regions corresponding to different values of the topological mass: QAHI when $\tilde{m}_z < -1$ and trivial insulator for $\tilde{m}_z > 1$. In this phase diagram, we have ignored b_t, as the WSM2 transition occurs generally when $\tilde{b}_t > 1$. Moreover, this choice of the parameters excludes the hybrid WSM phase[143]. Adapted from [4].

5.4 Effect of disorder

-After establishing the phases of the WSM in the clean limit, we now consider the inclusion of the disorder, the form of which is given as,

$$H_{dis} = \sum_{r,s} \epsilon_{r,s} c^{\dagger}_{r,s} c_{r,s} \tag{5.7}$$

where r and s are the coordinate in the lattice and spinor index respectively. $\epsilon_{r,s}$ is a uniformly distributed random number in the range of $[-W/2, W/2]$ utilized to mimic the random on-site disorder potential to be added into Eq. (5.3). Note that this disorder configuration does not preserve time-reversal symmetry, therefore we are considering both charge and magnetic disorder. Within a given distribution of the disorder, we begin by specifying the correlation function of the disorder, whose average value zero, in the following form $\langle \epsilon_{i,s} \rangle = 0$. The two point correlation of the disorder energy is given as, $\langle \epsilon_{i_1,s_1} \epsilon_{i_2,s_2} \rangle = \frac{[\int_{-W/2}^{W/2} \epsilon^2 d\epsilon]}{W} \delta_{i_1,i_2} \delta_{s_1,s_2} = \frac{W^2}{12} \delta_{i_1,i_2} \delta_{s_1,s_2}$. To more clearly see the effect of the disorder, we calculate the disorder averaged self-energy term in Green's function, $\bar{G}$, that is given as,

$$\bar{G} = \frac{1}{E - H_W - \Sigma_{dis} + i\eta} = \langle \frac{1}{E - (H_W + H_{dis}) + i\eta} \rangle, \tag{5.8}$$

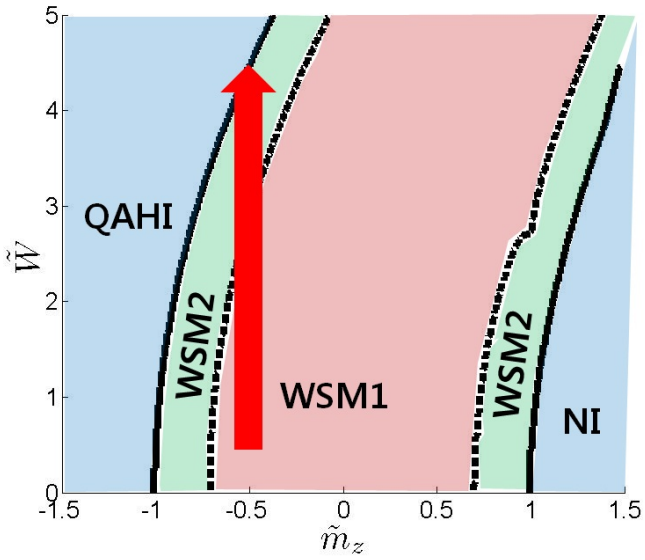

Figure 5.2: The phase diagram of the Weyl semimetal with the effect of disorder included as calculated from the first Born approximation with the parameters, $\tilde{t}_x = \tilde{t}_y = \tilde{a}_t = 1$. In this figure, we represent the different phases of WSM1, WSM2 and the insulating phase. We observe that, depending on the initial negative values of $\tilde{m}_z$, as we increase the disorder there exists a phase transition from WSM1 to WSM2 and finally to an insulating phase. However, we also note that for a range of values of positive $\tilde{m}_z$, we find that insulating metals may be driven through both the WSM2 and WSM1 phases with increasing disorder. Adapted from [4].

where $<>$ indicates the average expectation value over the random disorder configurations and η is the infinitesimal broadening term. To calculate the self energy, Σ_{dis}, we use the Dyson equation to dress the single particle Green's function given as,

$$\bar{G} = G_0 + G_0 \Sigma \bar{G} \tag{5.9}$$

where $G_0 = \frac{1}{E - H_W + i\eta}$ is the Green's function of the bare Hamiltonian without disorder. Then, applying the Born approximation, the correction of the self-energy term is equivalent to[144],

$$\begin{aligned} \Sigma &= \frac{[\int_{-W/2}^{W/2} \epsilon^2 d\epsilon]}{W} [I_2][< r_i | G_0 | r_i >] \\ &= \frac{W^2}{12} \int \frac{d^3k}{(2\pi)^3} \frac{1}{E - H + i\eta}. \end{aligned} \tag{5.10}$$

When we decompose the self-energy into its various directional contributions, these correspond to terms in

which the chemical potential and the topological mass near $E = 0$ are renormalized as[145, 121, 144],

$$\mu_{re} = \mu + lim_{k\to 0} Re(\Sigma_0), \tag{5.11}$$

$$m_{i,re} = m_i + lim_{k\to 0} Re(\Sigma_i). \tag{5.12}$$

Where Σ_i is the self-energy correction is decomposed into each of the i-th directional pauli matrices. We observe that $Re(\Sigma_{x,y})$ vanishes since the numerator of the Eq. (5.10) is an odd function of the momentum. Therefore, within the Born approximation, the value of the topological mass terms, m_x and m_y, are invariant even with the disorder included in our analysis. Using Eq. (5.10), Σ_z is derived as,

$$\Sigma_z \approx +W^2\alpha. \tag{5.13}$$

where the integral expression in the above equation, α, is derived from the evaluation of the Eq. (5.10) as,

$$\alpha = -\frac{1}{12}\int \frac{d^3k}{(2\pi)^3} m_0(2 - cos(k_x) - cos(k_y)) + (m_z - t_z cos(k_z)) \tag{5.14}$$

$$/|m_0(2 - cos(k_x) - cos(k_y)) + (m_z - t_z cos(k_z))|^2 + |t_x sin(k_x)|^2 + |t_y sin(k_y)|^2 - |a_t sin(k_z) + b_t cos(k_z)|^2$$

$$\approx \frac{-1}{48 m_0 \pi} log(|\frac{m_0^2\pi^4}{(m_z + \sqrt{m_z^2 - (a_t^2 + (b_t - t_z)^2)})(m_z + \sqrt{m_z^2 - (a_t^2 + (b_t + t_z)^2)})}|). \tag{5.15}$$

To obtain Eq. (5.15), we have kept terms only up to quadratic order of $k_{x,y}$ contributions of the integral. In similar manner as outlined in Eq. (5.11), a renormalization of the chemical potential also occurs when $b_{tilt,i} \neq 0$ since the b_{tilt} term is even function in the momentum space. However, the change of the chemical potential does not alter the phase of the WSM. We only focus on the renormalization of the topological mass.

In Eq. (5.15), we notice that the sign of α is always negative (of m_0), therefore, the disorder renormalizes the value of m_z to decreasing values as the magnitude of the disorder is increased as,

$$m_z \to m_z + \alpha W^2 \tag{5.16}$$

Furthermore, the Fermi velocity in z direction is also renormalized as

$$v_f = \tilde{t}_z sin(acos(m_z/t_z)) \tag{5.17}$$
$$\rightarrow \tilde{t}_z sin(acos((m_z + \alpha W^2)/t_z))$$

which results in the renormalization of the effective Fermi velocity in z direction. Therefore, while the tilt is invariant in the presence of the disorder, there is a decrease (increase) of the Fermi velocity when $\tilde{m}_z > 0 (\tilde{m}_z < 0)$. We find that when the effective Fermi velocity becomes smaller than the tilt at $\tilde{m}_z < 0$, WSM1 undergoes the disorder induced quantum phase transition to WSM2 and then to an insulating phase with increasing disorder, as shown in Fig. 5.2 indicated by the arrow. Additionally, the reverse transition from an insulating phase to WSM2 and finally to WSM1 with increasing disorder is possible if we start from $\tilde{m}_z \approx 1$. In addition to Anderson disorder, one may also consider the contribution arising from the presence of spin-flip disorder [146]. In this case, the self energy for the magnetic disorder, σ_z, gains an additional negative sign, which reverses the direction of the renormalization. For the detailed analysis on the origin of the negative sign, see J. Song et al.[146].

5.5 Numerical calculation

-While the first-order Born approximation offers an analytical insight of the disorder induced phase transition, to confirm the result from the Born approximation, we numerically investigate the disorder effect via exact diagonalization of the three-dimensional tight-binding Hamiltonian of Eq. (5.3). In the presence of the disorder, we calculate the momentum space spectral function to observe the phase transitions with increasing disorder. The spectral function calculation gives an estimate of the tilt and the topological mass with a finite broadening of the states due to the presence of the disorder[140]. As the value of the disorder increases, we use the largest value of the spectral function at a given k_z to identify the resultant change of the dispersion. The spectral function in the momentum space is defined as[147],

$$A(\omega, \mathbf{k}) = \sum_{i=1}^{2} \frac{|\phi_{n,i}(\mathbf{k})|^2}{\omega - E_n + i\eta} \tag{5.18}$$

Where η is the infinitesimal imaginary number and i is the band index of the eigenstate. E_n and $\phi_{n,i}(\mathbf{k})$ are the energy eigenvalue and the eigenstate of the Hamiltonian with disorder respectively. The spectral function is calculated using a system size of $8 \times 8 \times 60$ sites in the real space lattice. We numerically distinguish the WSM1, WSM2, and insulating phases by identifying the resultant changes of the dispersions and the tilt at

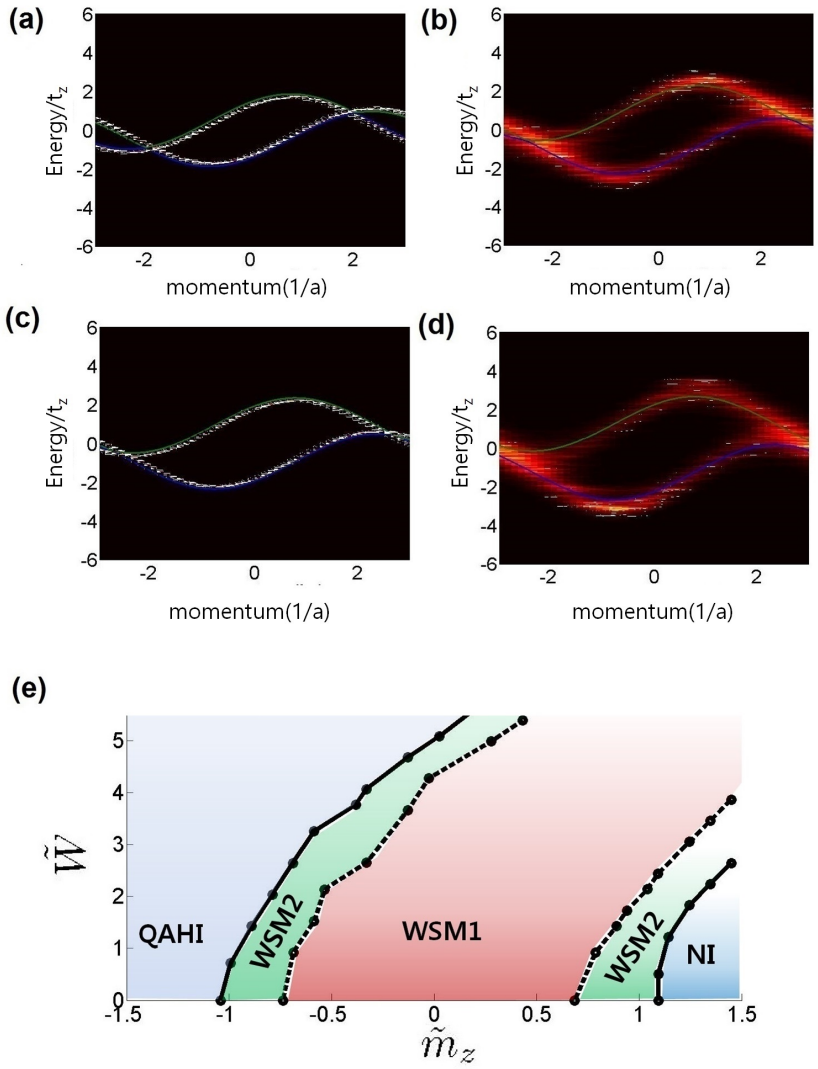

Figure 5.3: Spectral function and disorder induced phase diagram derived from exact diagonalization. In each of the plots at the top (a),(b),(c) and (d), we show the numerically calculated spectral function as a function of k_z. The plots (a),(b),(c), and (d) use the following parameters for $(\tilde{m_z}, \tilde{W})$: $(-0.27, 0), (-0.27, 3), (-0.78, 0), (-0.78, 4)$ respectively. We find that the system undergoes a phase transitions to WSM1-WSM2-QAHI, as predicted from the Born approximation. (e) The full phase diagram calculated from the exact diagonalization. This figure is generated with the parameters, $\tilde{t}_x = \tilde{t}_y = \tilde{a}_t = 1$. The parameters used in (a)-(d) are marked with different shapes on (e) respectively. Adapted from [4].

the cones, while the change of the tilt is calculated from the slopes of the dispersions at the cone. We identify the insulating phases when the spectral function contains a gapped dispersion, and, similarly, we identify the WSM2 phase when the resultant dispersion shows the characteristic tilted cones. Fig. 5.3 shows the disorder induced transition from the WSM1 to the WSM2 and, finally, to the insulating phase. To understand these different disorder induced transitions, we begin with Fig. 5.3 (a), which uses $(\tilde{m}_z, \tilde{W}) = (-0.27, 0)$, where we present the spectral function which contains degenerate crossings of two bands at $\mathbf{k} \approx (0, 0, \pm 2)$ where the Weyl nodes are located in momentum space along the $\hat{z}$-direction. The spectral function has no broadening as the corresponding phase and dispersion are calculated in the clean limit. We find that the two Weyl cones have no tilt, which indicates WSM1 phase. Gradual increase of W reduces the renormalized m_z according to Eq. (5.16), until γ_{tilt} dominates the Fermi velocity and resulting in WSM2 phase. Eventually, when $\tilde{W}$ reaches up to 3 in Fig. 5.3 (b), the calculated dispersion shows the tilted Weyl cones along $\hat{z}$ direction, therefore it signals the disorder induced phase transition from WSM1 to WSM2. In addition to the WSM1-WSM2 phase transition, Fig. 5.3 (c) and (d) show a transition from WSM2 phase to insulating phase. Fig. 5.3 (c), with the choice of the parameters $(\tilde{m}_z, \tilde{W}) = (-0.78, 0)$ shows WSM2 phase in the clean limit in which the spectral function has no broadening and shows the tilted Weyl cones. Again, the increase of W reduces the renormalized m_z until when the location of the nodes, $Q = \pm(acos(\tilde{m}_z)$, are ill-defined to gap out the dispersion. Fig. 5.3 (d) shows this transition, as the disorder, $\tilde{W}$, reaches the value of 4. Fig. 5.3 (d) shows the spectral function of the insulating phase which are fully gapped out. In result, the behavior of the transitions shown in the numerical calculation can be understood from the decrease of m_z and the resulting change of the Fermi velocity due to the disorder induced renormalization, in which it eventually shifts the full phase diagram to the positive m_z direction.

In Fig. 5.3 (e), we show the complete disorder induced phase diagram of the WSM as a function of $\tilde{W}$ and $\tilde{m}_z$ in which we derive by repeating the calculations with various values of m_z. The numerical phase diagram agrees in its behavior with the phase transitions predicted using the Born approximation in Fig. 5.2. The general trend, in which m_z reduces as the disorder increases, is similar to the previous study[145]. However, in contrast to the previous study, we find that there always exists a finite region of WSM2 phase before the WSM1 phase undergoes the transition to an insulating phase, when a_{tilt} is non-zero. This intermediate region of the WSM2 phase is guaranteed to exist because the Fermi velocity eventually vanishes and the tilt dominates before the insulating transition. Due to the WSM1-WSM2 transition, WSM1 phase near $\tilde{m}_z = -cos(atan(a_t))$ is unstable to the arbitrary weak disorder to the transition to the WSM2 phase. On the opposite side of the phase diagram where m_z is positive, WSM2 phase near $\tilde{m}_z = cos(atan(a_t))$ is unstable to the WSM1 phase transition as the renormalized m_z decreases the Fermi

velocity. On both sides of the phase boundaries, the WSM2 phase is unstable to the finite disorder, resulting the transitions to WSM1($\tilde{m}_z = cos(atan(a_t))$) and QAHI ($\tilde{m}_z = -1$), as the renormalized Fermi velocity and m_z is significantly modified. As the disorder increases large enough, Anderson localization can occur where the perturbation theory fails and the bulk gap collapses[145].

5.6 Conclusion

- In conclusion, we have studied the effect of disorder on the resultant phase diagram of WSM with a non-zero tilt to elucidate the boundaries of the different physical regimes as a function of disorder and topological mass. We have illustrated these various phase transitions both analytically, using the first Born approximation, and numerically, via exact diagonalization calculations. We find that the renormalization of the topological mass changes the effective Fermi velocity of the nodes reducing both the mass and resultant Fermi velocity with increasing values of disorder. The resulting change of the Fermi velocity leads to phase transitions between WSM1, WSM2, and insulator. Moreover, our results show that the disorder induced WSM2 phase always occurs before the metal-insulator transition of WSM1. Therefore, we assert that the WSM2 phase naturally occurs before the disorder induced transition between WSM1 and the insulating phases in the known WSM materials.

Chapter 6

Modular Anomalies in (2+1) and (3+1)-D Edge Theories

[1]

6.1 Introduction

Recent experimental observations of chiral anomaly in WSMs[128, 148, 149, 150] have gathered a great interests in both theory and experiment [151, 152, 153, 154, 155, 156, 157, 158, 159, 160]. The absence of $U(1)$ charge conservation in the presence of chiral anomaly indicates topological nature of the Weyl fermion[161, 162, 163], indicating that it can be only realized as a pair or surface of higher dimensional bulk in lattice. The chiral anomaly has been firstly proposed in the context high energy physics to explain the anomalous short life time in pion decay process, known as Adler-Bell-Jackiw anomaly[164, 165]. In the solid state systems, the chiral anomaly emerges as exotic transport effects, which have not been observed in conventional materials[11, 166]. The examples are nonlocal transport[151], chiral magnetic effect[154, 155, 156], chiral vortical effect[167], and angular dependence of the magenetoresistence[148, 168]. These effects manifests unique properties of the anomaly in the WSM.

Identifying the quantum anomaly and the non-trivial physical response is an important step for understanding the topological phases of matter. Indeed, the quantum anomaly and its response can be applied to characterize more general class of topological materials[18, 169, 8, 170, 171, 172]. The key idea is to examine quantum anomalies in non-interacting edge states, which indicate the presence of non-trivial topology in higher dimensional bulk. This is based on the observation that if the edge theory has a quantum anomaly that breaks a certain symmetry, then the edge theory cannot exists on its own dimension, but it must live on the edge of a higher dimensional system. Recent studies[173, 174, 175, 176, 177] have proposed that an analysis of the anomalies in gapless $(1+1)$-D theories can also indicate the presence of a topological phase in $(2+1)$-D dimensions.

A necessary step is to extend this method to higher space dimension. In this chapter, we extend concept

[1] Portions of this study were previously published as [5] and reprinted with permission (Copyright 2017 by American Physical Society).

of large gravitational anomaly under the modular transformations of gapless free fermion theories beyond $(1+1)$-D to examine higher dimensional edge theories. We show that the complex free fermions in both $(2+1)$-D Dirac and $(3+1)$-D chiral edge theories are modularly invariant. However, when an external magnetic field is coupled to the edge, the resultant Weyl modes show that a modular anomaly arises in the $(3+1)$-D edge theory indicating the presence of $(4+1)$-D quantum Hall effect.

6.2 Modular transformation in $(1+1)$-D

To begin, consider a relativistic conformal field theory (CFT) defined in a $(1+1)$-D compact space manifold $T^1 \times T^1$ where T^1 is a torus (a circle in 1D). On such a space, the theory can exhibit invariance at a classical level under modular transformations[178]. However, interesting cases arise when theories are not invariant under modular transformations resulting in the accumulation of an additional anomalous phase. The resultant anomaly is referred to as a large gravitational anomaly in the sense that it cannot be generated via continuous deformation of the original action[179, 173]. The modular group is defined as the group of linear fractional transformations of the upper half of the complex plane in which $\tau = L_0/L_1$ where L_0 and L_1 are the periods of the space and time coordinates respectively. τ transforms under the modular transformation:

$$\tau' = \frac{a\tau + b}{c\tau + d}, \tag{6.1}$$

where a, b, c, d are integers satisfying $ad - bc = 1$. The modular group is isomorphic to the projective special linear group $PSL(\mathbb{Z}, 2)$ [178]. In $(1+1)$-D, the generators of the group are $S : \tau \to -1/\tau$ and $T : \tau \to \tau + 1$. S and T act on the periods of each coordinate by $S : (L_0, L_1) \to (-L_1, L_0)$ and $T : (L_0, L_1) \to (L_0 + L_1, L_1)$. To generalize modular transformation to higher dimensions, we consider the group generated by two generators, which they act on the periods of each coordinate as, $S : (L_0, L_1, L_2) \to (L_1, L_2, L_0)$, $T : (L_0, L_1, L_2) \to (L_0 + L_1, L_1, L_2)$ in $(2+1)$-D, and $S : (L_0, L_1, L_2, L_3) \to (-L_1, L_2, L_3, L_0)$ and $T : (L_0, L_1, L_2, L_3) \to (L_0 + L_1, L_1, L_2, L_3)$ in $(3+1)$-D. In this case, the generalized modular transformation is then isomorphic to $PSL(\mathbb{Z}, d)$ (See Appendix A.5 in supplementary for the precise description of the modular transformation[180]). Under the S and T transformation, we can define the transformation matrices, A, for

example, in $(3+1)$-D as

$$A_S = \begin{pmatrix} 0 & -1 & 0 & 0 \\ 0 & 0 & 1 & 0 \\ 0 & 0 & 0 & 1 \\ 1 & 0 & 0 & 0 \end{pmatrix}, A_T = \begin{pmatrix} 1 & 1 & 0 & 0 \\ 0 & 1 & 0 & 0 \\ 0 & 0 & 1 & 0 \\ 0 & 0 & 0 & 1 \end{pmatrix}. \tag{6.2}$$

With these definitions, we consider the action of the modular group on the partition function in $(1+1)$-D[181], which is well-known to possess an anomaly. The most direct method to see the anomaly under the modular transformation is to calculate the partition function explicitly and apply the transformation. The partition function of $(1+1)$-D edge can be obtained in a well-regularized form as (For detailed calculation, see Appendix A.6 in supplementary[180])

$$\begin{aligned} Z_{\lambda_0\lambda_1} &= [e^{2\pi i(1/2-\lambda_0)(1/2-\lambda_1)} q^{(\lambda_1^2-\lambda_1+1/6)/2}] \\ &\times [(1-\omega)\prod_{n_1=1}^{\infty}(1-\omega q^{n_1})(1-\omega^{-1}q^{n_1})] \end{aligned} \tag{6.3}$$

where $\omega = q^{\lambda_1} e^{2\pi i \lambda_0}$, $q = e^{2\pi i \tau}$. $\lambda_0, \lambda_1 = 0(1/2)$ refers to the periodic (anti-periodic) boundary condition of the time and space coordinate directions respectively. By explicitly applying the modular transform, one derives the modular anomaly[174],

$$\begin{aligned} T[Z(\tau)_{\lambda_0\lambda_1}] &= e^{i\pi(\lambda_1^2-\lambda_1+1/6)} Z(\tau)_{\lambda_0'\lambda_1'} \\ S[Z(\tau)_{\lambda_0\lambda_1}] &= e^{i2\pi(\lambda_1-1/2)(\lambda_0-1/2))} Z(\tau)_{\lambda_0'\lambda_1'} \end{aligned} \tag{6.4}$$

λ' is the transformed boundary conditions under the modular transformation where $\lambda_\mu' = A_{\mu\nu}\lambda_\nu$. The sign of anomalous phase flips if the chirality of the $(1+1)$-D mode is reversed. Therefore, the combination of two edges of opposite chirality achieves modular invariance[176]. This result is consistent with the fact that two opposite chiral edges can be gapped out by adding mass term. However, it is also possible to achieve modular invariance with finite copies of the same chirality[173].

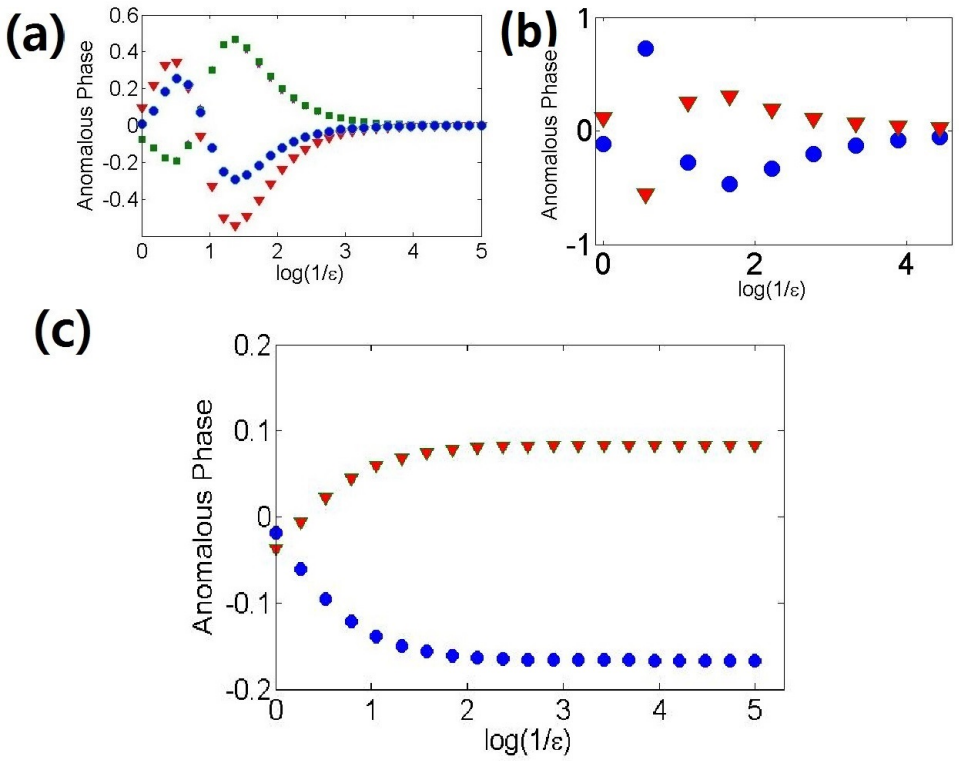

Figure 6.1: Calculation of numerical regularization scheme for: (a) T transformation of (2+1)-D chiral edge. (b)(3+1)-D (c)(3+1)-D with magnetic field. Each lines represent different values of boundary condition. In (a), blue circles, red triangles and green squares represent $(\lambda_1, \lambda_2) = (0,0), (0.5,0), (0.5,0.5)$ respectively. In (b), blue circles and red triangles represent $(\lambda_1, \lambda_2, \lambda_3) = (0,0,0), (0.5,0,0)$. In (c), blue circles and red triangles represent $(\lambda_1, \lambda_2, \lambda_3) = (0.5,0,0), (0,0,0)$. We include sufficient numbers of high energy states within each calculation of the energy cutoff until the anomalous phase value converges. In (a) and (b) all choices of boundary conditions converge to zero indicating modular invariance. When the magnetic field is inserted, the anomaly approaches to the value(1/6,-1/12) in accordance with Eq. (6.42) with $N_\phi = 1$. Details of the numerical calculation method are provided in Appendix A.8). Adapted from [5].

6.3 Method

Now we wish to elucidate higher dimensional gapless edges, thus we examine $(2+1)$-D and $(3+1)$-D edge theories where the action is given by

$$\mathcal{S} = \int d^d x \bar{\psi}(\partial_\tau + \sigma \cdot k)\psi \tag{6.5}$$

In contrast to $(1+1)$-D, we cannot simply perform the transformation of the partition function since an expression of the well-regularized partition function is not available. We can understand the failure of the regularization more clearly by applying the zeta function regularization method[182, 183] to higher dimensional edge theories. In given edge theory, the expression of the unregularized partition function contains a summation of the energy eigenvalues over all states. In $(2+1)$-D, we have $\sum_{k_x,k_y} \sqrt{k_x^2+k_y^2}$ and in $(3+1)$-D, $\sum_{k_x,k_y,k_z} \sqrt{k_x^2+k_y^2+k_z^2}$. When the sum is divergent, a successful zeta function regularization should utilize analytic continuation to assign a finite value to the divergent sum. Unfortunately, this is difficult since the Epstein-Hurwitz zeta (EZ) functions in $(3+1)$-D, $\zeta(\epsilon) = \sum_{n_1,n_2,n_3} ({n_1}^2+{n_2}^2+{n_3}^2)^{-\epsilon}$, and $(2+1)$-D, $\sum_{n_1,n_2} ({n_1}^2+{n_2}^2)^{-\epsilon}$, are meromorphic at $\epsilon = -1/2$[184], which forbids assigning a finite value to the summation of energy eigenvalues. To circumvent this issue, we instead focus on the change of path integral measure[9, 10]. The calculation of the change of the measure only requires EZ function at $\epsilon = 0$ and $\epsilon = -1$, which have well defined finite values (See Appendix A.7 in supplementary[180]).

To calculate the change of measure, we work on the Fourier transformed field basis:

$$\psi_{\boldsymbol{\lambda}}(\mathbf{x},\mathbf{s}) = \sum_{\mathbf{n},\mathbf{s}} a_{\mathbf{n},s} \Phi_{\mathbf{n}+\boldsymbol{\lambda}}(\mathbf{x}) \chi_{\mathbf{s}} \tag{6.6}$$

$\mathbf{n} = (n_0, n_1, n_2, n_3)$ are integers, which n_i refers the frequency of i-th direction in the Fourier transformed basis. $\boldsymbol{\lambda} = (\lambda_0, \lambda_1, \lambda_2, \lambda_3)$ are the boundary conditions, which $\lambda_i = 0(1/2)$ refers to the periodic (anti-periodic) boundary condition. We simplify the notations by defining $\widetilde{\mathbf{n}} = \mathbf{n} + \boldsymbol{\lambda}$. In other words,

$$\Phi_{(\widetilde{n}_0,\widetilde{n}_1,\widetilde{n}_2,\widetilde{n}_3)}(x) = e^{2\pi i(\sum_{i=0}^{4}(n_i+\lambda_i)x_i)} \tag{6.7}$$

and $\chi_{\mathbf{s}}(\mathbf{s}=\pm)$ is a two component spinor such that $\chi_+ = (1,0)^T$,$\chi_- = (0,1)^T$. By following the transformation rule in appendix A.5, we represent the change of coefficient a' under modular transformation

as,

$$a'_{\mathbf{n}',\mathbf{s}'} = \int d^d x \Phi^\dagger_{\mathbf{n}'+\boldsymbol{\lambda}'} \chi^\dagger_{\mathbf{s}} \psi_{\boldsymbol{\lambda}}(A^T x) \tag{6.8}$$
$$= \sum_{\mathbf{n},\mathbf{s}} [\int d^d x \Phi^\dagger_{\mathbf{n}'+\boldsymbol{\lambda}'}(\mathbf{x}) \Phi_{\mathbf{n}+\boldsymbol{\lambda}}(A^T \mathbf{x})][\chi^\dagger_{\mathbf{s}'} \chi_{\mathbf{s}}] a_{\mathbf{n},\mathbf{s}},$$

where A is the matrix representations of the generators. The above equation leads us to define the transformation matrix C between $a_{\mathbf{n},\mathbf{s}}$ and $a'_{\mathbf{n},\mathbf{s}}$.

$$C_{\mathbf{n}',\mathbf{n},\mathbf{s}',\mathbf{s}} = \int d^d x \Phi^\dagger_{\mathbf{n}'+\boldsymbol{\lambda}'}(\mathbf{x}) \Phi_{\mathbf{n}+\boldsymbol{\lambda}}(A^T \mathbf{x})[\chi^\dagger_{\mathbf{s}'} \chi_{\mathbf{s}}] \tag{6.9}$$

In terms of Fourier transformed field basis, the change of path integral measure is given by,

$$D\bar{\psi}' D\psi' = D\bar{a}' Da' = D\bar{a} Da \; det(C)^{-2} \tag{6.10}$$

We treat ψ and $\bar{\psi}$ independently, hence we obtain an additional contribution of -2 sign from the Grassman algebra. In $(3+1)$-D, each momentum mode Φ transforms under modular transformation by (Appendix A.5),

$$T[\Phi_{\tilde{n}_0,\tilde{n}_1,\tilde{n}_2,\tilde{n}_3}] = \Phi_{\tilde{n}_0+\tilde{n}_1,\tilde{n}_1,\tilde{n}_2,\tilde{n}_3}, \tag{6.11}$$
$$S[\Phi_{\tilde{n}_0,\tilde{n}_1,\tilde{n}_2,\tilde{n}_3}] = \Phi_{-\tilde{n}_1,\tilde{n}_2,\tilde{n}_3,\tilde{n}_0}.$$

To calculate $Det(C)$, we select a basis that diagonalizes C. We define the basis as linear combinations of modes under successive applications of T and S as,

$$|\theta, \overrightarrow{n}\rangle_{\boldsymbol{\lambda}} \eta_{s,\overrightarrow{\tilde{n}}} = \Phi_{\boldsymbol{\lambda}} \sum_{n_0=0}^{n_1-1} \sum_{j=-\infty}^{\infty} e^{2\pi i(\tilde{n}_0+n_1 j)\theta} T^j[\Phi_{n_0,\overrightarrow{n}}] \eta_{s,\overrightarrow{\tilde{n}}} \tag{6.12}$$
$$|\phi, \mathbf{n}\rangle_{\boldsymbol{\lambda}} \chi_s = \Phi_{\boldsymbol{\lambda}-1/2} \sum_{j=0}^{N-1} e^{2\pi i j\phi/N} S^j[\Phi_{\mathbf{n}+1/2}] \chi_s,$$

where $\overrightarrow{n}$ is the vector of the frequencies in spatial directions. N is the order of S such that Φ_{n_0,n_1,n_2,n_3} returns to the original mode under N application of S. In $(1+1), (2+1), (3+1)$-D, $N = 4, 3, 8$ respectively, except for modes Φ_{n_0,n_0,n_0} in $(2+1)$-D. $\theta \in [0,1)$ and $\phi \in \{-(\frac{N}{2}-1), -\frac{N-2}{2}, .., \frac{N}{2}\}$(In $(2+1)$-D,$\phi \in \{-1,0,1\}$). To avoid double counting of the basis for S, we restrict the momentum indices to $n_0, n_1 \geq 0$ in $(1+1)$-D, $n_0 \geq n_1 \geq n_2$ in $(2+1)$-D, and $n_0, n_1, n_2 \geq 0$ in $(3+1)$-D. η is the spinor which diagonalizes the Hamiltonian

simultaneously. Then the basis satisfies

$$T|\theta,\overrightarrow{n}\rangle_{\boldsymbol{\lambda}} = e^{-2\pi i\widetilde{n}_1\theta}|\theta,\overrightarrow{n}\rangle_{T[\boldsymbol{\lambda}]} \tag{6.13}$$
$$S|\phi,\mathbf{n}\rangle_{\boldsymbol{\lambda}} = e^{-2\pi i\phi/N}|\phi,\mathbf{n}\rangle_{S[\boldsymbol{\lambda}]}$$

In $(2+1)$-D, the C matrix, using the new basis for T and S, is a diagonal matrix given by

$$C^{2D}_{T,\{\theta,n_1,n_2,\theta',n_1',n_2'\}} = (e^{-2\pi i\widetilde{n}_1\theta})\delta(\theta-\theta')\delta_{\overrightarrow{n},\overrightarrow{n}'} \tag{6.14}$$
$$C^{2D}_{S,\{\phi,n_0,n_1,n_2,\phi',n_0',n_1',n_2'\}} = (e^{-2\pi i\phi/N})\delta_{\phi,\phi'}\delta_{\mathbf{n},\mathbf{n}'}.$$

To regulate the determinant of C, we use the Epstein-Hurwitz type zeta function regulator that has the same form as energy dispersion, $|p|^{-\epsilon}$, where ϵ, in this instance, is a scale which cuts off the high energy states.

In a similar manner with $(2+1)$-D, the modular transformations, S and T, of the transformation matrix, C, in $(3+1)$-D are given by(See Appendix A.7 in supplementary[180]),

$$C^{3D}_{T,\{\theta,n_1,n_2,n_3,\theta',n_1',n_2',n_3'\}} = (e^{-2\pi i\widetilde{n}_1\theta})\delta(\theta-\theta')\delta_{\overrightarrow{n},\overrightarrow{n}'}. \tag{6.15}$$
$$C^{3D}_{S,\{\phi,n_0,n_1,n_2,n_3,\phi',n_0',n_1',n_2',n_3'\}} = (e^{-2\pi i\phi/N})\delta_{\phi,\phi'}\delta_{\mathbf{n},\mathbf{n}'}.$$

By regulating the determinants above matrices with zeta function regularization method, we can derive the expression of the anomaly.

6.4 T transformation

In this section, we show that the anomalous phases under T transformation cancel out in both $(2+1)$-D and $(3+1)$-D. We begin by reproducing the modular anomaly of $(1+1)$-D chiral edge. The basis which diagonalizes the transformation matrix, C, under the T transformation is given according to Eq. (6.12).

$$|\theta,n_1\rangle_{\lambda_0,\lambda_1} = \Phi_{\lambda_0,\lambda_1}\sum_{n_0=0}^{n_1-1}\sum_{j=-\infty}^{\infty} e^{2\pi i(\widetilde{n}_0+n_1 j)\theta}T^j[\Phi_{n_0,n_1}], \tag{6.16}$$

where $\theta \in [0,1)$. Application of the T transformation to $|\theta, n_1\rangle_{\lambda_0,\lambda_1}$ is given as,

$$\begin{aligned} & T|\theta, n_1\rangle_{\lambda_0,\lambda_1} \\ &= T[\Phi_{\lambda_0,\lambda_1} \sum_{n_0=0}^{n_1-1} \sum_{j=-\infty}^{\infty} e^{2\pi i(\widetilde{n}_0+n_1 j)\theta} T^j[\Phi_{n_0,n_1}]] \\ &= \sum_{n_0=0}^{n_1-1} \sum_{j=-\infty}^{\infty} e^{2\pi i(\widetilde{n}_0+n_1 j)\theta} \Phi_{(n_0+n_1)+jn_1+(\lambda_0+\lambda_1),n_1+\lambda_1} \\ &= e^{-2\pi i(n_1+\lambda_1)\theta}|\theta, n_1\rangle_{\lambda_0+\lambda_1,\lambda_1}. \end{aligned} \tag{6.17}$$

As a result, the newly selected basis diagonalizes C_T^{1D} matrix resulting in Eq. (6.12), namely

$$C^{1D}_{T,\{\theta,n_1,\theta',n_1'\}} = (e^{-2\pi i(n_1+\lambda)\theta})\delta(\theta-\theta')\delta_{n_1,n_1'}. \tag{6.18}$$

After the diagonalization of C_T^{1D} matrix, the determinant is given as the product of the diagonal entries. We divide the partition function of the path integral form into the anomalous divergent contribution, Z_A, and the regular contribution, Z_R, with the total partition function, $Z_{total} = Z_A Z_R$. In the calculation of the total partition function, we note that the anomalous contribution, Z_A, is the path integral of the negative dispersion modes only. The regular contribution to the total partition function, Z_R is invariant under the T transformation, $Z_{R,\lambda}(\tau+1) = \prod_{n_1=0}^{\infty}(1-e^{(2i\pi\tau(n_1+\lambda_1)+2i\pi(\lambda_0+\lambda_1))}) = Z_{R,\lambda'}$ indicating that the contribution to the modular anomaly under the T transformation comes entirely from Z_A. In other words, the regularized form of the total partition function transforms under the T transformation as

$$\begin{aligned} Z_{total,\lambda}(\tau+1) &= [Z_{A,\lambda}(\tau+1)][Z_{R,\lambda}(\tau+1)] \\ &= [{C_T^{1D}}^{-2} Z_{A,\lambda'}(\tau)][Z_{R,\lambda'}(\tau)]. \end{aligned} \tag{6.19}$$

Therefore, we regularize the change of the measure of Z_A, which restricts the C matrix to the negative momentums. Then, the anomalous phase of C_T^{1D} is given by

$$\begin{aligned} arg(det(C_T^{1D})) &= -2\pi[\int_0^1 d\theta\theta][\sum_{n_1=-\infty}^{-1}(n_1+\lambda)] \\ &= -\pi\frac{1}{2}(\lambda^2-\lambda+1/6). \end{aligned} \tag{6.20}$$

The above anomalous phase reproduces the known modular anomaly in (1+1)-D under the T transformation.

To extend the calculation beyond $(1+1)$-D, we use the matrices given by Eq. (6.14) and Eq. (6.15) to extend to $(2+1)$-D and $(3+1)$-D respectively. With the addition of the requisite extra dimensional momentum indices, we can write the phases of $det(C)$ in the same form as of Eq. (6.20) for both $(2+1)$-D and $(3+1)$-D cases as,

$$arg(det(C_T^{2D})) = -2\pi \sum_{n_1,n_2\in\mathbb{Z}} \int_0^1 d\theta\theta(n_1+\lambda_1) \tag{6.21}$$
$$= -\pi \sum_{n_1,n_2\in\mathbb{Z}} (n_1+\lambda_1) = -\sum_{n_1,n_2=-\infty}^{\infty} \frac{L_x^2}{8\pi}\frac{\partial}{\partial\lambda_1}(F_2)^2.$$

and

$$arg(det(C_T^{3D})) = -2\pi \sum_{n_1,n_2,n_3\in\mathbb{Z}} \int_0^1 d\theta\theta(n_1+\lambda_1) \tag{6.22}$$
$$= -\pi \sum_{n_1,n_2,n_3\in\mathbb{Z}} (n_1+\lambda_1) = -\sum_{n_1,n_2,n_3=-\infty}^{\infty} \frac{L_x^2}{8\pi}\frac{\partial}{\partial\lambda_1}(F_3)^2,$$

where $F_2 = 2\pi\sqrt{\widetilde{n_1}^2/L_x^2 + \widetilde{n_2}^2/L_y^2}$ is the dispersion in $(2+1)$-D and $F_3 = 2\pi\sqrt{\widetilde{n_1}^2/L_x^2 + \widetilde{n_2}^2/L_y^2 + \widetilde{n_3}^2/L_z^2}$ is the dispersion in $(3+1)$-D. In order to evaluate the above summations, we must define the following Epstein-Zeta functions in which we use the variable ϵ to denote the scale that cuts off the high energy states:

$$E_2(\epsilon, c_1, c_2, a_1, a_2) \tag{6.23}$$
$$\equiv \sum_{n_1,n_2=0}^{\infty} (a_1(n_1+c_1)^2 + a_2(n_2+c_2)^2)^{-\epsilon},$$

$$G_2(\epsilon, c_1, c_2, a_1, a_2) \tag{6.24}$$
$$\equiv \sum_{n_1,n_2=-\infty}^{\infty} (a_1(n_1+c_1)^2 + a_2(n_2+c_2)^2)^{-\epsilon},$$

$$E_3(\epsilon, c_1, c_2, c_3, a_1, a_2, a_3) \equiv \tag{6.25}$$
$$\sum_{n_1,n_2,n_3=0}^{\infty} (a_1(n_1+c_1)^2 + a_2(n_2+c_2)^2 + a_3(n_3+c_3)^2)^{-\epsilon},$$

$$G_3(\epsilon, c_1, c_2, c_3, a_1, a_2, a_3) \equiv \tag{6.26}$$
$$\sum_{n_1,n_2,n_3=-\infty}^{\infty} (a_1(n_1+c_1)^2 + a_2(n_2+c_2)^2 + a_3(n_3+c_3)^2)^{-\epsilon},$$

$$G_3(\epsilon, c_1, c_2, c_3, a_1, a_2, a_3) \equiv \tag{6.27}$$
$$\sum_{n_1,n_2=0,n_3=-\infty}^{\infty} (a_1(n_1+c_1)^2 + a_2(n_2+c_2)^2 + a_3(n_3+c_3)^2)^{-\epsilon}.$$

We substitute previous summations over the dispersion relations, F, into the newly defined Zeta function expressions to obtain the anomalous phase resulting from the application of the T-transform in higher dimensions as

$$arg(det(C_T^{2D})) \tag{6.28}$$
$$= -\frac{\pi}{2} L_x^2 \frac{\partial}{\partial \lambda_1} G_2(-1, \lambda_1, \lambda_2, 1/L_x^2, 1/L_y^2)$$

in $(2+1)$-D and

$$arg(det(C_T^{3D})) \tag{6.29}$$
$$= -\frac{\pi}{2} L_x^2 \frac{\partial}{\partial \lambda_1} G_3(-1, \lambda_1, \lambda_2, \lambda_3, 1/L_x^2, 1/L_y^2, 1/L_z^2)$$

in $(3+1)$-D. The expression of the above zeta function, G_3, is well-defined and vanishes at $\epsilon = -1$. We find that the resulting anomalous phases are zero which indicates the absence of the anomaly under the T transformation(For calculation of the value of the zeta function, see Appendix A.7 in supplementary[180]).

6.5 S transformation

After establishing the the absence of the anomaly under the T transformation, we now prove the absence of the modular anomaly in $(2+1)$-D and $(3+1)$-D under the S transformation. We again start from the modular anomaly of a $(1+1)$-D edge. According to Eq. (6.12), the basis that diagonalizes the C matrix is

given by

$$|\phi, n_0, n_1\rangle_{\lambda_0,\lambda_1} \tag{6.30}$$
$$= \Phi_{\lambda_0-1/2,\lambda_1-1/2}(\Phi_{n_0+1/2,n_1+1/2} + e^{2\pi i\phi/4}\Phi_{-n_1+1/2,n_0+1/2}$$
$$+e^{2\pi i2\phi/4}\Phi_{-n_0+1/2,-n_1+1/2} + e^{2\pi i3\phi/4}\Phi_{n_1+1/2,-n_0+1/2})$$

Where $\phi \in \{-1, 0, 1, 2\}$. The application of the S transformation to $|\phi, n_0, n_1\rangle$ is given as,

$$S|\phi, n_0, n_1\rangle_{\lambda_0,\lambda_1} \tag{6.31}$$
$$= \Phi_{-\lambda_1,\lambda_0}(\Phi_{-n_1,n_0} + e^{2\pi i\phi/4}\Phi_{-n_0,-n_1}$$
$$+e^{2\pi i2\phi/4}\Phi_{n_1,-n_0} + e^{2\pi i3\phi/4}\Phi_{n_0,n_1})$$
$$= e^{-2\pi i\phi/4}|\phi, n_0, n_1\rangle_{-\lambda_1,\lambda_0}$$

The C matrix is then a diagonal matrix given by the expression,

$$C^{1D}_{S,\{\phi,n_0,n_1,\phi',n_0',n_1'\}} = (e^{-2\pi i\phi/N})\delta_{\phi,\phi'}\delta_{n_0,n_0'}\delta_{n_1,n_1'}. \tag{6.32}$$

As the determinant of diagonal matrix is the product of the diagonal entries, we have the unregulated phase of the C matrix under the S-transform

$$arg(det(C^{1D}_S)) = \tag{6.33}$$
$$-2\pi[\sum_{\phi=-1,0,1,2} \phi/4][\sum_{n_0=0}^{\infty} 1][\sum_{n_1=0}^{\infty} 1]$$

We regularize the above sum by attaching the following regulator.

$$-2\pi \sum_{\phi=-1,0,1,2} \phi/4 \sum_{n_0=0}^{\infty}(n_0+\lambda_0)^0 \sum_{n_1=0}^{\infty}(n_1+\lambda_1)^0 \tag{6.34}$$
$$= -\pi\zeta(0,\lambda_0)\zeta(0,\lambda_1) = -\pi(1/2-\lambda_0)(1/2-\lambda_1)$$

The above expression of the anomalous phase again reproduces the modular anomaly of the S transformation.

To extend the calculation into higher dimensions, we use the matrices given by Eq. (6.14) and (6.15).

Using these, we write the phase of $det(C_S)$ in $(2+1)$-D and $(3+1)$-D as,

$$arg(det(C_S^{2D})) = -4\pi[\sum_{\phi=-1,0,1} \phi/3][\sum_{n_0 \geq n_1 \geq n_2} 1] \tag{6.35}$$

$$\begin{aligned} &arg(det(C_S^{3D})) \\ &= -4\pi[\sum_{\phi=-3,-2,..,4} \phi/8][\sum_{n_0,n_1,n_2=0,n_3=-\infty}^{\infty} 1] \end{aligned} \tag{6.36}$$

Without requiring the complete summation of the modes, we immediately see that $arg(det(C_S^{2D})) = 0$ from the summation of ϕ. To calculate C_S^{3D}, we again connect the EZ zeta function to expression of the C matrix,

$$\begin{aligned} &arg(det(C_S^{3D})) \\ &= -2\pi \sum_{n_0=0}^{\infty} \sum_{n_1,n_2=0,n_3=-\infty}^{\infty} (n_0+\lambda_0)^0 (F_3)^0, \end{aligned} \tag{6.37}$$

The connection between the determinant of the transformation matrix, $det(C_S^{3D})$, and the EZ zeta function is given by

$$\begin{aligned} &arg(det(C_S^{3D})) \\ &= -2\pi(1/2-\lambda_0) g_3(0,\lambda_1,\lambda_2,\lambda_3,a_1,a_2,a_3), \end{aligned} \tag{6.38}$$

Again, the zeta function g_3 vanishes at $\epsilon = 0$. Therefore, we find that the modular anomaly under the S transformation is absent. By showing that the free fermions in both $(2+1)$-D and $(3+1)$-D have no anomaly under S and T transformation, we conclude that the free fermions are modular anomaly free.

Beyond analytical calculations to confirm our result numerically, we calculate the Casmir energy of the $(2+1)$-D and $(3+1)$-D edge theory. In the numerical calculation, we explicitly calculate the partition function by summing up the Boltzmann weights of all the possible states with a given high energy cutoff. By comparing the numerical values of the partition functions before and after the modular transformation, we calculate the anomalous phase(For detailed implementation of the algorithm, see Appendix A.8 in supplementary[180]). Fig. 6.1 (a) and (b) show the numerically calculated anomalous phase as a function of the high energy cut off scale. As we include more high energy states, we find the anomalous phases in Fig. 6.1 (a) and (b) converges to zero which indicates the absence of the modular anomaly in $(2+1)$-D and $(3+1)$-D edge theories.

Unlike the zeta function regularization of the entire partition function, the explicit numerical summation of Boltzmann weights does not distinguish higher dimensional partition functions from slices of $(1+1)$-D partition functions where each $(1+1)$-D partition function has a specific transverse momentum. While each slice of the partition function is regularizable using the zeta function, our numerical calculation regularizes the slices one by one individually.

The cancellation of the modular anomaly is not surprising as one may represent a gapless theory in $(2+1)$-D on a lattice indicating that a higher dimensional bulk is not required to regularize a $(2+1)$-D theory. Further, this indicates that $(2+1)$-D gapless theory can be generically gapped out by breaking time-reversal symmetry. Nonetheless, by adding symmetry constraints, a modular anomaly can be found[177] in $(2+1)$-D. In contrast to $(2+1)$-D, the Nielsen-Ninomiya (NN) theorem in $(3+1)$-D suggests that the chiral edge of even dimension cannot be written without the aid of bulk theory[13]. Therefore, it is natural to expect an anomalous contribution in even dimensions even without symmetry projection. Thus, in the next section, we show that the chiral fermion in $(3+1)$-D shows a modular anomaly(mixed modular anomaly) when $U(1)$ gauge field is coupled to it.

6.6 Mixed modular anomaly

While chiral free fermions in $(3+1)$-D are modular anomaly free, attaching a background $U(1)$ gauge field changes the situation. Consider the chiral edge under a uniform magnetic field pointing out-of-plane in the z-direction thereby breaking the periodicity of the in-plane x and y coordinates. Therefore, the full modular transformation that is isomorphic to $PSL(\mathbb{Z},4)$ is no longer a good symmetry of the action, Eq. (6.5). However, we can still safely consider $PSL(\mathbb{Z},2)$ acting on both z and the time component as a subgroup of the original $PSL(\mathbb{Z},4)$. We write the Hamiltonian for this situation as,

$$H = (\overrightarrow{k} - \overrightarrow{A}) \cdot \overrightarrow{\sigma}, \tag{6.39}$$

with magnetic vector potential A written in the Landau gauge, $A = (0, -Bx, 0)$. This Hamiltonian has two types of solutions. $E_{W(D)}$ is gapless(gapped) Landau level(LL).

$$E_W(k_3) = k_z, E_D(n, k_3) = \pm\sqrt{Bn + k_3^2}, \tag{6.40}$$

where $k_3 = 2\pi(n_3 + \lambda_3)/L_z$ and n is an positive integer. We can write the unregularized partition function to be

$$Z_{\lambda_0,\lambda_3} = [\prod_{k_3}(1 - e^{2\pi i\lambda_0 - \beta E_W(k_z)}) \tag{6.41}$$
$$\times \prod_{n,k_z}(1 - e^{2\pi i\lambda_0 + \beta E_D(n,k_z)})(1 - e^{2\pi i\lambda_0 - \beta E_D(n,k_z)})]^{N_\phi},$$

where N_ϕ is the level degeneracy and $\omega = q^{\lambda_3}e^{2\pi i\lambda_0}$. After regularization, we find that the chiral modes contribute to the anomaly while gapped landau levels do not contribute as they are massive (For explicit calculations of massive mode, see Appendix A.9 in supplementary[180]). This reflects the fact that the regularized Casimir energy has no contribution from gapped states. Therefore, the modular transforms of the partition function of a $(3+1)$-D edge theory coupled to a $U(1)$ gauge field are

$$T[Z_{\boldsymbol{\lambda}}] = e^{iN_\phi\pi(\lambda_3^2 - \lambda_3 + 1/6)}Z_{\boldsymbol{\lambda}'} \tag{6.42}$$
$$S[Z_{\boldsymbol{\lambda}}] = e^{iN_\phi 2\pi(\lambda_3 - 1/2)(\lambda_0 - 1/2))}Z_{\boldsymbol{\lambda}'}$$

and clearly contain a modular anomaly that is proportional to N_ϕ, which counts the number of $(1+1)$-D chiral modes. To confirm, we again look at the numerical calculation of the Casmir energy in Fig. 6.1(c) where we find that the anomalous phase value under T transformation reproduces the transformation rules given in Eq. (6.42). Thus, the $(3+1)$-D chiral edge, when coupled to a background gauge field, contains a modular anomaly. In contrast to $(1+1)$-D, $(3+1)$-D chiral edge has charge pumping but only in conjunction with the magnetic field, in analogy to the chiral anomaly[11]. Therefore, we conclude the presence of modular anomaly when $N_\phi \neq 0$, is a direct manifestation of quantum Hall effect of $(4+1)$-D.

6.7 Conclusion

In conclusion, we have generalized modular transformation in $(1+1)$-D CFT to higher dimensional edge theory with use of $PSL(\mathbb{Z}, d)$ group supported by numerical calculations of the Casmir energies. We have shown the gapless free fermion theories in $(2+1)$-D and $(3+1)$-D are modular invariant. We find a modular anomaly in $(3+1)$-D when the edge theory is coupled to a $U(1)$ gauge field resulting in a $(4+1)$-D quantum Hall effect.

Appendix A

Calculational Details

A.1 The correlation function of the s-wave order parameter for 2D surface model

In this section, we describe how the induced order parameter in 2D surface state model of the TI is calculated. Within the phenomonological model for the induced order parameter, we consider the 8×8 2D BdG Hamiltonian defined in Eq. (2.10) in the main text. The particle operator is defined as $\Phi_{\mathbf{k}} = [\Psi_{\mathbf{k}}, \Psi^*_{-\mathbf{k}}]^T$ where $\Psi = [c_{t,\uparrow}(\mathbf{k}), c_{t,\downarrow}(\mathbf{k}), c_{b,\uparrow}(\mathbf{k}), c_{b,\downarrow}(\mathbf{k})]$. We diagonalize the Hamiltonian in Eq. (2.10) and obtain eigenfunctions, U, and eigenvalues, D, which satisfies $\hat{H}_{\mathrm{BdG}}U = UD$. Then we define the quasi-particle operator $\Gamma_{\mathbf{k}} = U^\dagger \Phi_{\mathbf{k}}$ from $\Phi^\dagger_{\mathbf{k}} \hat{H}_{\mathrm{surf}} \Phi_{\mathbf{k}} = \Phi^\dagger_{\mathbf{k}} U (U^\dagger \hat{H}_{\mathrm{surf}} U) U^\dagger \Phi_{\mathbf{k}} = \Gamma^\dagger_{\mathbf{k}} D \Gamma_{\mathbf{k}}$, where $\Gamma_{\mathbf{k}} = [\gamma_{1,\mathbf{k}}, \ldots, \gamma_{8,\mathbf{k}}]^T$ with the quasi-particle spectrum index ranging from $1, 2, \cdots, 8$. The particle operator may be written as Bogoliubov quasi-particle operators, namely, $\Phi_{\mathbf{k}} = U\Gamma_{\mathbf{k}}$, where each element is expressed as $[\Phi_{\mathbf{k}}]_i = \sum_j [U]_{ij} [\Gamma_{\mathbf{k}}]_j$. For example, the electron annihilation operator of the top surface is

$$c_{t,\uparrow}(\mathbf{k}) = [\Phi_{\mathbf{k}}]_1 = \sum_i [U]_{1i} [\Gamma]_i = \sum_i u_{1i} \gamma_{i,\mathbf{k}}, \tag{A.1}$$

where we define $u_{ij} = [U]_{ij}$. As a result, we may write the correlation function of the top surface as

$$F_t^{\uparrow\downarrow}(\mathbf{k}) = \langle c_{t,\uparrow}(\mathbf{k}) c_{t,\downarrow}(-\mathbf{k}) \rangle = \sum_{i,j} u_{1i} u^\dagger_{6j} \langle \gamma^\dagger_{j,\mathbf{k}} \gamma_{i,\mathbf{k}} \rangle = \sum_i u_{1i} u^\dagger_{6i} \langle \gamma^\dagger_{i,\mathbf{k}} \gamma_{i,\mathbf{k}} \rangle = \sum_i u_{1i} u^\dagger_{6i} f(E_{i,\mathbf{k}}) = [U \cdot f(D) \cdot U^\dagger]_{16}, \tag{A.2}$$

where $f(E)$ is Fermi-Dirac distribution at energy E, and we utilize the quasi-particle operator properties: $\gamma^\dagger_i \gamma_j + \gamma^\dagger_j \gamma_i = \delta_{ij}$ and $\langle \gamma^\dagger_i \gamma_i \rangle = f(E_i)$. Finally, the correlation function of the s-wave order parameter at the top surface is defined as

$$F_{S,t}(\mathbf{k}) = F_t^{\uparrow\downarrow}(\mathbf{k}) - F_t^{\downarrow\uparrow}(\mathbf{k}) = [U \cdot f(D) \cdot U^\dagger]_{16} - [U \cdot f(D) \cdot U^\dagger]_{25}. \tag{A.3}$$

The correlation function of the bottom surface is determined similarily.

A.2 Numerical evaluation of the Chern number in a 2D square lattice

In this section, we describe how the Chern number is calculated in a 2D square lattice. We begin with the generic Hamiltonian having its eigenfucntion of the nth band, $|n(\mathbf{k}_l)\rangle$, where the momentum is defined in a square lattice Brillouin zone as

$$\mathbf{k} = (k_{j_x}, k_{j_y}),\ k_{j_{x/y}} = \frac{2\pi j_{x/y}}{N_{x/y}}, \tag{A.4}$$

with the momentum index $j_{x/y} = 0, \cdots, N_{x/y} - 1$ and $l = 1, \cdots, N_x N_y$. Note that the eigenfunction is periodic in momentum space and satisfies $|n(\mathbf{k}_l)\rangle = |n(\mathbf{k}_l + N_i \hat{e}_i)\rangle$, where $\hat{e}_i$ is a vector in the $i = (x, y)$ direction. To compute the field strength through a lattice plaquette, we first define a link variable[57] that corresponds to the Berry connection in reciprocal space in the continuum as

$$U_i(\mathbf{k}_l) = \langle n(\mathbf{k}_l) | n(\mathbf{k}_l + \hat{e}_i)\rangle / \mathcal{N}_i(\mathbf{k}_l), \tag{A.5}$$

assuming that $\mathcal{N}_i(\mathbf{k}_l) = |\langle n(\mathbf{k}_l) | n(\mathbf{k}_l + \hat{e}_i)\rangle|$ is well-defined. Then the field strength is evaluated as[57]

$$\tilde{C}_{xy}(\mathbf{k}_l) = \ln U_x(\mathbf{k}_l) U_y(\mathbf{k}_l + \hat{x}) U_x(\mathbf{k}_l + \hat{y})^{-1} U_y(\mathbf{k}_l)^{-1}, \tag{A.6}$$

which satisfies $-\pi < \tilde{C}_{xy}(\mathbf{k}_l)/i \leq \pi$ due to the logarithm applied to the link variables. By summing over all the plaquettes, we obtain the Chern number of nth band as

$$\tilde{c}_n = \frac{1}{2\pi i} \sum_l \tilde{C}_{xy}(\mathbf{k}_l). \tag{A.7}$$

A.3 3D TI induced order parameter calculation

In this section, we describe how the induced order parameter of the 3D TI model is calculated. In order to self-consistently solve the system of equations, we diagonalize the BdG Hamiltonian to determine the spectrum of the proximity-coupled system. To simplify this procedure, the Bogoliubov transform is taken

on Eq. (2.31) to form the eigenvalue equation

$$\hat{H}_{\mathrm{BdG}}(\mathbf{k},z)\begin{bmatrix} u_{\mathbf{k},z,n} & -v^*_{\mathbf{k},z,n} \\ v_{\mathbf{k},z,n} & u^*_{\mathbf{k},z,n}\end{bmatrix} = \begin{bmatrix} E_n & 0 \\ 0 & -E_n\end{bmatrix}\begin{bmatrix} u_{\mathbf{k},z,n} & -v^*_{\mathbf{k},z,n} \\ v_{\mathbf{k},z,n} & u^*_{\mathbf{k},z,n}\end{bmatrix}, \tag{A.8}$$

where we suppress spin and orbital index for simplicity and the energy eigenvalues E_n correspond to the eigenvector $\psi_{n,\mathbf{k},z} = \{u_{\mathbf{k},z,n}, v_{\mathbf{k},z,n}\}^T$. Then a pair correlation function is defined and may be computed numerically from this diagonalization procedure as following:

$$F^{s,s'}_{\alpha,\alpha'}(\mathbf{k},z) = \langle c_{\mathbf{k},z,\alpha,\sigma} c_{-\mathbf{k},z,\alpha',\sigma'}\rangle = \sum_n u^{\alpha,s}_{\mathbf{k},z,n}(v^{\alpha',s'}_{\mathbf{k},z,n})^*[1-2f(E_n)], \tag{A.9}$$

where α, α' are orbital index, s, s' are spin index, $f(E)$ is Fermi-Dirac distribution. We note that the selection of a temperature in our system is of little relevance to the simulations so long as it is smaller than the size of the superconducting gap. Threfore, we set the temperature to $T = 0$ K.

In this work, we consider Hubbard type on-site interaction for spin-singlet pairing. To consider relevant electron-electron pairing, we consider an on-site interaction for spin-singlet pairing channel:

$$\hat{H}_{\mathrm{int}} = -\sum_{\mathbf{r},\alpha,\alpha',s,\bar{s}} V_{\mathbf{r}} n_{\mathbf{r},\alpha,s} n_{\mathbf{r},\alpha',\bar{s}}, \tag{A.10}$$

where $V_{\mathbf{r}} > 0$ represents interaction strength, $n_{\mathbf{r},\alpha,s} = c^\dagger_{\mathbf{r},\alpha,s} c_{\mathbf{r},\alpha,s}$ is the density operator to describe the occupation number on α orbital with spin state $s(\neq \bar{s})$ at site $\mathbf{r}$. Assuming a constant interaction strength, $V_{\mathbf{r}} = V > 0$, the mean field decomposition of the spin-singlet pairing Hamiltonian in Eq. (A.10) results in

$$\hat{H}^{\mathrm{MF}}_{\mathrm{int}} = -V\sum_{\mathbf{r},\alpha,\alpha'}\left\{\Delta_{S,\alpha\alpha'}(\mathbf{r}) c^\dagger_{\mathbf{r},\alpha',\downarrow} c^\dagger_{\mathbf{r},\alpha,\uparrow} - \Delta_{S,\alpha\alpha'}(\mathbf{r}) c^\dagger_{\mathbf{r},\alpha,\uparrow} c^\dagger_{\mathbf{r},\alpha',\downarrow} + h.c. - F^{\uparrow,\downarrow}_{\alpha,\alpha'}(F^{\uparrow,\downarrow}_{\alpha,\alpha'})^\dagger - F^{\downarrow,\uparrow}_{\alpha',\alpha}(F^{\downarrow,\uparrow}_{\alpha',\alpha})^\dagger\right\}, \tag{A.11}$$

where we define the pair correlation function in real space as

$$F^{s,s'}_{\alpha,\alpha'}(\mathbf{r},\mathbf{r}') = \langle c_{\mathbf{r},\alpha,\sigma} c_{\mathbf{r}',\alpha',\sigma'}\rangle, \tag{A.12}$$

and a spin-singlet order parameter in real space,

$$\Delta_{S,\alpha\alpha'}(\mathbf{r}) = \frac{1}{2}[F^{\uparrow,\downarrow}_{\alpha,\alpha'}(\mathbf{r},\mathbf{r}) - F^{\downarrow,\uparrow}_{\alpha',\alpha}(\mathbf{r},\mathbf{r})]. \tag{A.13}$$

We perform a Fourier transform of Eq. (A.11) to momentum space in $\hat{x}$ and $\hat{y}$ direction. As a result, we

obtain

$$\hat{H}_{\text{int}}^{\text{MF}} = -V \sum_{\mathbf{k},z,\alpha} \left\{ \Delta_{S,\alpha}(z) c^{\dagger}_{-\mathbf{k},z,\alpha,\downarrow} c^{\dagger}_{\mathbf{k},z,\alpha,\uparrow} + \Delta_{S,\alpha,\bar{\alpha}}(z) c^{\dagger}_{-\mathbf{k},z,\bar{\alpha},\downarrow} c^{\dagger}_{\mathbf{k},z,\alpha,\uparrow} + h.c. \right\}, \tag{A.14}$$

where we drop the constant term from Eq. (A.11). Then the intra-orbital singlet order parameter is defined as

$$\Delta_{S,\alpha}(z) = \frac{1}{2} \sum_{\mathbf{k}} [F^{\uparrow,\downarrow}_{\alpha,\alpha}(\mathbf{k},z) - F^{\downarrow,\uparrow}_{\alpha,\alpha}(\mathbf{k},z)], \tag{A.15}$$

and the inter-orbital singlet order parameter is defined as

$$\Delta_{S,\alpha\bar{\alpha}}(z) = \frac{1}{4} \sum_{\mathbf{k}} [F^{\uparrow,\downarrow}_{\alpha,\bar{\alpha}}(\mathbf{k},z) - F^{\downarrow,\uparrow}_{\bar{\alpha},\alpha}(\mathbf{k},z) + F^{\uparrow,\downarrow}_{\bar{\alpha},\alpha}(\mathbf{k},z) - F^{\downarrow,\uparrow}_{\alpha,\bar{\alpha}}(\mathbf{k},z)], \tag{A.16}$$

where $\bar{\alpha} \neq \alpha$, and each of the Fourier transformed pair correlation functions are computed numerically using Eq. (A.9). Note that Eqs. (A.15) and (A.16) are even under momentum exchange and odd under spin exchange.

A.4 Momentum-space mapping of order parameter in 3D heterostructure

A wealth of information can be gathered from analyzing the momentum resolution we have in our self-consistent 3D simulation by defining the momentum-resolved intra-orbital s-wave order parameter

$$\Delta_S^{\text{intra}}(\mathbf{k},z) = \frac{1}{2}[F^{\uparrow,\downarrow}_{A,A}(\mathbf{k},z) - F^{\downarrow,\uparrow}_{A,A}(\mathbf{k},z) + F^{\uparrow,\downarrow}_{B,B}(\mathbf{k},z) - F^{\downarrow,\uparrow}_{B,B}(\mathbf{k},z)]. \tag{A.17}$$

We first consider these features when time-reversal symmetry is preserved with $m_z = 0$ in Figs. A.1 (a-b). In Fig. A.1(a), we plot the band structure of the top-most layer of a 4-unit-cell TI without proximity coupling or superconductivity. The $\hat{y}$ and $\hat{z}$ directional spin texture are illustrated as the horizontal and vertical vector components, respectively, of the superimposed arrows, whose length is proportional to the relative magnitude of the individual components. In the surface band structure, we can clearly observe both the hybridization gap and the spin-momentum locking of the topologically non-trivial surface bands. The bulk states are spin-degenerate, therefore, we see no net spin texture in bulk bands. The chemical potential indicated by the solid, horizontal line shows that both bulk and surface states are available for pairing at the Fermi surface. By noting the intersection of the chemical potential with the energy bands of the non-superconducting TI, we can identify the bulk and surface components of the s-wave order parameter of the

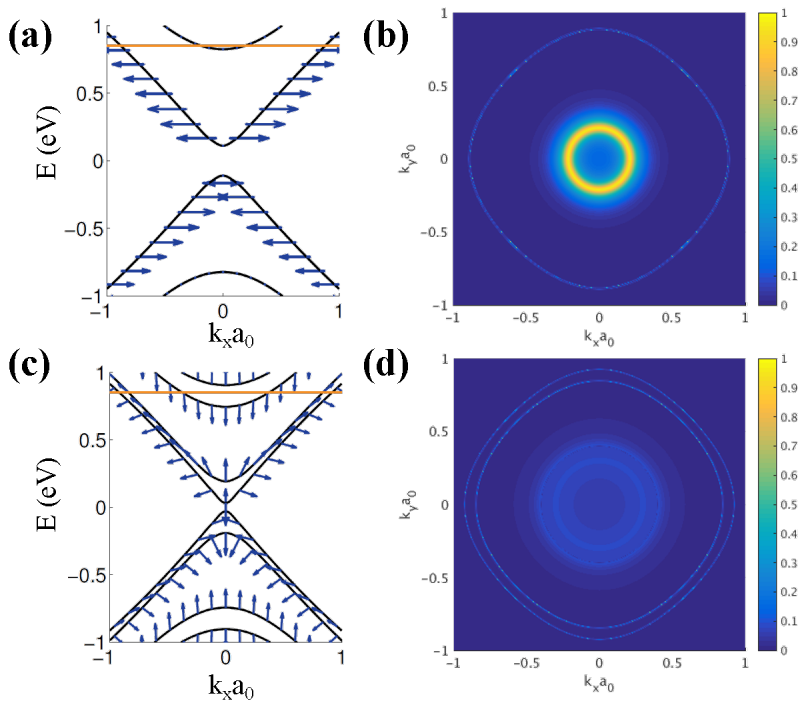

Figure A.1: (a) Band structure of the top surface ($z = 14$) of a non-superconducting 4-unit-cell TI at $m_z = 0$ and $k_y = 0$ with the chemical potential of 850 meV as indicated by the solid line. Spin is indicated with blue arrows, and for visual clarity, the horizontal axis for the arrows corresponds to the $\hat{y}$-component of spin, while the vertical axis is for $\hat{z}$-component of spin. (b) The magnitude of the momentum resolved s-wave order parameter magnitude $|\Delta_S^{\text{intra}}(\mathbf{k}, z = 14)|$ defined in Eq. (A.17). The result displays a clear bulk contribution in the Brillouin zone center and a surface state contribution in the outer ring. (c) Band structure of the top surface of a non-superconducting 4-unit-cell TI at m_z= 80 meV and $k_y = 0$ with the chemical potential of 850 meV as indicated by the solid line. We observe that the spin-degenerate bulk states split due to the presence of the magnetization. In the surface states, the Zeeman energy instead cants the spin out of the plane into the $\pm\hat{z}$-direction. (d) The bulk contribution to the s-wave component of the order parameter is strongly suppressed due to the presence of $\hat{z}$-directed magnetism while the surface contribution is resilient as the canted spins still have a significant in-plane projection that allows for persistent s-wave pairing.

proximity-coupled heterostructure in Fig. A.1(b). The large contribution in the inner ring corresponds to the bulk component of s-wave pairing. Similarly, the large outer ring in $\Delta_S^{\text{intra}}(\mathbf{k}, z = 14)$ corresponds to the wave vectors associated with the surface states and their associated s-wave contribution. This knowledge allows us to unambiguously identify the surface and bulk contributions analyzed in the main text. Specifically, we separate surface states contribution from bulk states contribution by computing Eq. (A.15) using the correlation function obtained at momentum space points that satisfy $|\mathbf{k}| > |\mathbf{k}_c|$. In this work, we set the momentum cut-off as $|\mathbf{k}_c a| = 0.6$ in the determination of the s-wave order parameters for bulk and surface states.

With the physics of the order parameter understood when time-reversal symmetry is preserved, Figs. A.1 (c-d) now show the effects of Zeeman energy on the resulting superconducting order parameter when $m_z = 80$

meV, which explicitly breaks time-reversal symmetry. The effect of Zeeman energy is evident in the non-superconducting TI surface band structure, shown in Fig. A.1(c). When $m_z > 0$, we observe that the spin-degenerate bulk bands split with spin oriented completely in the $\hat{z}$ direction with the up-spin states are pushed to higher energies and the down-spin states to lower. In the surface bands, we see a qualitatively different picture. Because of the initial in-plane spin configuration of the hybridized surface bands, $m_z > 0$ has the effect of canting the spin texture towards the $\pm\hat{z}$, or, out-of-plane direction. This canted spin texture is characteristic of the Zeeman splitting of surface bands that has been observed experimentally in the presence of magnetically ordered impurities in TI samples[44]. Due to the hybridization of the surface state wave functions in the system, the surface bands also split in energy with the energy change dictated by the sign of z-directed cant: up-canted spins rise in energy and down-canted spins lower. The presence of magnetism has immediate consequences to the different components of the superconducting order parameter. In Fig. A.1(d), we observe that because the up- and down-spin states in the bulk are no longer present at opposing momenta, the bulk contribution to s-wave pairing is strongly suppressed. The surfaces states however, still have strong s-wave pairing despite the Zeeman splitting from the magnetism. Due to the fact that the spins of the surface states are only canted, a projection of spin is still anti-parallel across the Brillouin zone and s-wave pairing is still energetically favorable. This results in a persisting magnitude of the s-wave order parameter in the surface states despite the energetic separation of surface bands.

A.5 General Properties of the Modular Transformation

In this section, we consider the general properties of the modular transformation, A, on the d-dimensional torus, T^d, written as

$$\hat{L}'_\mu = A_{\mu\nu}\hat{L}_\nu, \tag{A.18}$$

where $A \in PSL(d, \mathbb{Z})$ and $\hat{L}_\mu$ is the period of the torus along the μ-th direction. The period of the torus is a vector within the torus of which a separate coordinate vector, $\mathbf{x}$, satisfies

$$\mathbf{x} = \mathbf{x} + n_\mu \hat{L}_\mu \tag{A.19}$$

where n_μ is a integer. In $(1+1)$-D, we can express $\hat{L}_\mu$ utilizing simple complex coordinates, however, in $(2+1)$-D and $(3+1)$-D, we must express the period in quaternion coordinates. A vector, $\mathbf{x}$, on the torus

may be parameterized using $x_\mu \in [0,1)$ as,

$$\mathbf{x} = x_\mu \hat{L}_\mu. \tag{A.20}$$

As we are interested in the modular transformations within (2+1)-D and (3+1)-D systems, it is important to identify the relevant generators within the relevant $PSL(d,\mathbb{Z})$ group. Therefore, we identify the generators of the group $PSL(3,\mathbb{Z})$ that are given by[185]

$$S = \begin{pmatrix} 0 & 1 & 0 \\ 0 & 0 & 1 \\ 1 & 0 & 0 \end{pmatrix}, T = \begin{pmatrix} 1 & 1 & 0 \\ 0 & 1 & 0 \\ 0 & 0 & 1 \end{pmatrix} \tag{A.21}$$

and the generators of the group $PSL(4,\mathbb{Z})$ are given by

$$S = \begin{pmatrix} 0 & -1 & 0 & 0 \\ 0 & 0 & 1 & 0 \\ 0 & 0 & 0 & 1 \\ 1 & 0 & 0 & 0 \end{pmatrix}, T = \begin{pmatrix} 1 & 1 & 0 & 0 \\ 0 & 1 & 0 & 0 \\ 0 & 0 & 1 & 0 \\ 0 & 0 & 0 & 1 \end{pmatrix}. \tag{A.22}$$

By applying the matrices shown in Eq. (A.21) and Eq. (A.22) on Eq. (A.18), we see that the generators S and T act on the modular parameter in the same manner as that of the modular transformation in higher dimensions, namely: $S : (L_0, L_1, L_2, L_3) \to (-L_1, L_2, L_3, L_0)$ and $T : (L_0, L_1, L_2, L_3) \to (L_0 + L_1, L_1, L_2, L_3)$.(In $(2+1)$-D, $S : (L_0, L_1, L_2) \to (L_1, L_2, L_0)$ and $T : (L_0, L_1, L_2) \to (L_0 + L_1, L_1, L_2)$)

We now explore action of the modular transform by imposing that the coordinate vector $\mathbf{x}$ is invariant under the following transformation,

$$\mathbf{x} = x_\mu \hat{L}_\mu = x_\mu A^{-1}_{\mu\nu} \hat{L}'_\nu, \tag{A.23}$$

This allows one to show that the components of the coordinate vector, $\mathbf{x}$, transform as

$$x'_\mu = (A^{-1})^T_{\mu\nu} x_\nu. \tag{A.24}$$

Meanwhile, derivatives transform as,

$$\partial_\mu = \frac{\partial x'_\nu}{\partial x_\mu} \frac{\partial}{\partial'_\nu} = A^{-1}_{\mu\nu} \partial'_\nu. \tag{A.25}$$

and the various fermionic fields transform via,

$$\psi'_{\lambda'}(x') := \psi_{\lambda}(x). \tag{A.26}$$

It then follows that we may write the transformed fermionic fields as,

$$\psi'_{\lambda'}(x) = \psi_{\lambda}(A^{T}_{\mu\nu}x). \tag{A.27}$$

It is necessary to define the relevant boundary conditions for the corresponding fermionic fields. In $(2+1)$-D, the corresponding boundary conditions, $\lambda_{2D} = (\lambda_0, \lambda_1, \lambda_2)$, and $(3+1)$-D, $\lambda_{3D} = (\lambda_0, \lambda_1, \lambda_2, \lambda_3)$, may be defined as,

$$\psi_{\lambda}(x_\nu \hat{L}_\nu + \hat{L}_\mu) = e^{2\pi i \lambda_\mu}\psi_{\lambda}(x_\nu \hat{L}_\nu). \tag{A.28}$$

By using Eq. (A.26) and Eq. (A.28), we find the modular transformation of the boundary conditions to be,

$$\begin{aligned} e^{2\pi i \lambda_\mu}\psi_{\lambda}(x_\nu \hat{L}_\nu) = \psi_{\lambda}(x_\nu \hat{L}_\nu + \hat{L}_\mu) \\ = \psi'_{\lambda'}(x'_\nu \hat{L'}_\nu + (A^{-1})^{T}_{\rho\mu}\hat{L'}_\rho) = e^{2\pi i \lambda'_\rho (A^{-1})^{T}_{\rho\mu}}\psi'_{\lambda'}(x'_\nu \hat{L'}). \end{aligned} \tag{A.29}$$

By equating the two phases on the left and right hand sides of Eq. (A.29), the boundary conditions transform as,

$$\lambda'_\mu = A_{\mu\nu}\lambda_\nu. \tag{A.30}$$

Finally, we must consider the how the Lagrangian transforms under the modular transformation. This can be accomplished through,

$$\mathcal{L}[\psi_\lambda(x), L^{-1}_\mu \partial_\mu \psi_\lambda(x)] = \mathcal{L}[\psi'_{\lambda'}(x'), L^{-1}_\mu A^{-1}_{\mu\nu}\partial'_\nu \psi'_{\lambda'}(x')]. \tag{A.31}$$

A.6 Calculation of the Partition Function in $(1+1)$-D

We begin the calculation of the partition function in $(1+1)$-D by writing the unregularized partition function of the $(1+1)$-D action. For a chiral $(1+1)$-D edge with the dispersion $E(k) = k$, the temperature $\beta = \frac{1}{T}$

and the length L in x direction, we have the action that may be defined as,

$$\begin{aligned} & S_{\lambda_0,\lambda_1}[\bar{\psi}_\lambda, \psi_\lambda] \\ &= -\beta L \int_0^1 dx \int_0^1 d\tau [\bar{\psi}(\tau,x)_\lambda (\partial_\tau/\beta + (-i\partial_x/L))\psi_\lambda(\tau,x)] \\ &= -\int_0^1 dx \int_0^1 d\tau \bar{\psi}(\tau,x)_\lambda (L\partial_\tau - i\beta\partial_x)\psi(\tau,x)_\lambda, \end{aligned} \tag{A.32}$$

where $\lambda_{0,1}$ denotes the boundary condition of the fermionic field ψ_λ as either periodic or anti-periodic respectively. Under a modular transformation, $A_{\mu\nu}$, the action transforms as shown in Eq. (A.31),

$$\begin{aligned} S_{\lambda_0,\lambda_1}[\bar{\psi},\psi] &= -\int_0^1 dx \int_0^1 d\tau \bar{\psi}_\lambda(\tau,x)[L(A_{22}\partial_\tau - A_{12}\partial_x) - i\beta(A_{11}\partial_x - A_{21}\partial_\tau)]\psi(\tau,x)_\lambda \\ &= -\int_0^1 dx \int_0^1 d\tau \bar{\psi}_\lambda(\tau,x)(L_1\partial_\tau - L_0\partial_x)\psi_\lambda(\tau,x), \end{aligned} \tag{A.33}$$

where $L_0 = A_{11}i\beta + A_{12}L$ and $L_1 = A_{21}i\beta + A_{22}L$ are the periods of the torus, as defined in Appendix A. After the Fourier transformation along the time and the space directions, the action becomes

$$S_{\lambda_0,\lambda_1}[\bar{a},a] = -\sum_{n_0,n_1} \bar{a}_{n_0,n_1}(2\pi L_1(n_0+\lambda_0) - 2\pi L_0(n_1+\lambda_1))a_{n_0,n_1}. \tag{A.34}$$

GIven the action, it is then a simple task to find the corresponding partition function that is given as,

$$\begin{aligned} Z_{\lambda_0,\lambda_1} &= \prod_{n_0,n_1=-\infty}^{\infty} \frac{1}{L_1}(2\pi i L_1(n_0+\lambda_0) - 2\pi i Ł_0(n_1+\lambda_1)) \\ &= \prod_{n_0,n_1=-\infty}^{\infty} (2\pi i(n_0+\lambda_0) - 2\pi i\tau(n_1+\lambda_1)), \end{aligned} \tag{A.35}$$

where $\tau = \frac{L_0}{L_1}$. The factor $\frac{1}{L_1}$ comes from the normalization factor of the path integral integrand. Using the Matsubara summation formula, we obtain a more simplified expression for the partition function,

$$Z_{\lambda_0\lambda_1} = \prod_{n_1=-\infty}^{\infty} (1 - e^{2i\pi\tau(n_1+\lambda_1)+2i\pi\lambda_0}). \tag{A.36}$$

With the definition of the partition function, we now regularize the partition function as

$$Z_{\lambda_0\lambda_1} = \prod_{n_1=-\infty}^{\infty}(1-e^{2i\pi\tau(n_1+\lambda_1)+2i\pi\lambda_0}) \tag{A.37}$$

$$= \prod_{n_1=-\infty}^{-1} -(1-e^{-2i\pi\tau(n_1+\lambda_1)-2i\pi\lambda_0})e^{2i\pi\tau(n_1+\lambda_1)+2i\pi\lambda_0}\prod_{n_1=0}^{\infty}(1-e^{2i\pi\tau(n_1+\lambda_1)+2i\pi\lambda_0}) \tag{A.38}$$

$$= [e^{-2\pi i(1/2-\lambda_0)\sum_{n_1=-\infty}^{-1}1}e^{2\pi i\tau\sum_{n_1=-\infty}^{-1}(n_1+\lambda_1)}][(1-\omega)\prod_{n_1=1}^{\infty}(1-\omega q^{n_1})(1-\omega^{-1}q^{n_1})], \tag{A.39}$$

where $q = e^{2\pi i\tau}$, $\omega = e^{2\pi i\lambda_0}q^{\lambda_1}$. In order to complete the proof, we use the Hurwitz zeta function that is defined as,

$$\zeta(-1,\lambda_1) = \sum_{n_1=0}^{\infty}(n_1+\lambda_1) = \frac{-1}{2}({\lambda_1}^2-\lambda_1+1/6) \tag{A.40}$$

$$\zeta(0,\lambda_1) = \sum_{n_1=0}^{\infty}(n_1+\lambda_1)^0 = (1/2-\lambda_1). \tag{A.41}$$

By using the following identities, we change the above summations from those over positive integers to a summation covering negative integers so as to complete the above summations by using following identities:

$$\sum_{n_1=-\infty}^{-1}(n_1+\lambda_1) = -\sum_{n_1=0}^{\infty}(n_1+1-\lambda_1) = -\zeta(-1,1-\lambda_1) = \frac{1}{2}({\lambda_1}^2-\lambda_1+1/6) \tag{A.42}$$

and,

$$\sum_{n_1=-\infty}^{-1}(n_1+\lambda_1)^0 = \sum_{n_1=0}^{\infty}(n_1+1-\lambda_1)^0 = \zeta(0,1-\lambda_1) = -(1/2-\lambda_1). \tag{A.43}$$

By substituting the above summations into the expression of the partition function found in (A.37), the final form of the $(1+1)$-D regularized partition function is given by

$$Z = [e^{2\pi i(1/2-\lambda_0)(1/2-\lambda_1)}q^{(\lambda_1^2-\lambda_1+1/6)/2}][(1-\omega)\prod_{n_1=1}^{\infty}(1-\omega q^{n_1})(1-\omega^{-1}q^{n_1})]. \tag{A.44}$$

A.7 Assigning the Determinant of the C Matrix

A.7.1 1.C matrix under the T transformation

To evaluate the expression of the zeta functions defined in the main text, we use following recursion equation[184],

$$E_N(\epsilon, c_1...c_N, a_1, ..a,_N) = \frac{1}{\Gamma(\epsilon)}\sum_{m=0}^{\infty}\frac{(-1)^m}{m!}a_1^m\zeta(-2m, c_1)\Gamma(\epsilon+m)E_{N-1}(\epsilon+m, c_2...c_N, a_2, ..a_N) \quad (A.45)$$
$$+\frac{1}{2}\sqrt{\frac{\pi}{a_1}}\frac{\Gamma(\epsilon-\frac{1}{2})}{\Gamma(\epsilon)}E_{N-1}(\epsilon-\frac{1}{2}, c_2, ...c_N, a_2, ..., a_N)$$
$$+\sqrt{\frac{\pi}{a_1}}\frac{cos(2\pi c_1)}{\Gamma(\epsilon)}\sum_{n_1=1}^{\infty}\sum_{n_2,n_3..n_N=0}^{\infty}\int_0^{\infty}t^{\epsilon-3/2}exp[-\frac{\pi^2 n_1^2}{a_1 t}-t\sum_{j=1}^{N}a_j^2(n_j+c_j)^2]dt.$$

In (A.45), the gamma function $\Gamma(n)$ is given by $\Gamma(n) = (n-1)!$ when n is positive integer and the function is divergent at $n = 0, -1, -2...$ We additionally make use of the the gamma function identity $\Gamma(x+1) = x\Gamma(x)$ when evaluating the recursion relationship. In order to make (A.45) more tractable, we break the right hand side of the equation into distinct terms and label each of the terms as E_A, E_B, and E_C. The first of these terms, A, is given by

$$E_A = \zeta(0, c_1)E_{N-1}(\epsilon+0, c_2, ..c_N, a_2, ..., a_N) - \frac{\Gamma(\epsilon+1)}{\Gamma(\epsilon)}a_1\zeta(-2, c_1)E_{N-1}(\epsilon+1, c_2...c_N, a_2, ..., a_N)+$$
$$+\frac{1}{\Gamma(\epsilon)}\sum_{m=2}^{\infty}\frac{(-1)^m\Gamma(\epsilon+m)}{m!}a_1^m\zeta(-2m, c_1)E_{N-1}(\epsilon+m, c_2...c_N, a_2, ..., a_N), \quad (A.46)$$

where we have expanded out the $m = 0$ and $m = 1$ terms for clarity. We notice that we may immediately eliminate the last term in the (A.7.1) due to the divergent denominator. The second of these terms is E_B that is defined as

$$E_B = \frac{1}{2}\sqrt{\frac{\pi}{a_1}}\frac{\Gamma(\epsilon-\frac{1}{2})}{\Gamma(\epsilon)}E_{N-1}(\epsilon-\frac{1}{2}, c_2, ...c_N, a_2, ..., a_N).$$

It is clear that E_B vanishes by inspection as the denominator is divergent while the numerator remains finite. The integral expression of E_C can be rewritten from its form in (A.45) to a more simplified form as,

$$E_C = \int_0^\infty dt t^{\epsilon-3/2} exp[-\frac{\pi^2 n_1^2}{a_1 t} - t\sum_{j=1}^{N} a_j^2(n_j+c_j)^2] \tag{A.47}$$

$$= \sqrt{\pi}\frac{e^{-2\sqrt{\frac{\pi^2 n_1^2}{a_1}\sum_{j=1}^{N} a_j^2(n_j+c_j)^2}}}{\sqrt{\frac{\pi^2 n_1^2}{a_1}}}. \tag{A.48}$$

when $\epsilon = 0$ and in which E_C becomes

$$= \sqrt{\pi}\frac{\left(1+2\sqrt{\frac{\pi^2 n_1^2}{a_1}}\sqrt{\sum_{j=1}^{N} a_j^2(n_j+c_j)^2}\right) e^{-2\sqrt{\frac{\pi^2 n_1^2}{a_1}}\sqrt{\sum_{j=1}^{N} a_j^2(n_j+c_j)^2}}}{2(\frac{\pi^2 n_1^2}{a_1})^{3/2}}, \tag{A.49}$$

when $\epsilon = -1$. In the previous expressions for E_C we observe that the integral expressions are exponentially decaying, therefore the entire numerator of C is finite thereby resulting in a vanishing contribution from E_C.

Therefore, we conclude that when $\epsilon = -1, 0$,

$$E_N(\epsilon, c_1 ... c_N, a_1, .., a_N) = A \tag{A.50}$$

$$= \zeta(0, c_1) E_{N-1}(\epsilon+0, c_2, ... c_N, a_2, ..., a_N) - \frac{\Gamma(\epsilon+1)}{\Gamma(\epsilon)} a_1 \zeta(-2, c_1) E_{N-1}(\epsilon+1, c_2 ... c_N, a_2, ..., a_N).$$

The final recursion relation in Eq. (A.50) is evaluated for the $(2+1)$-D case ($N = 2$) at $\epsilon = -1$ and $\epsilon = 0$ in conjunction with the expression $E_1(\epsilon, c_1, a_1) = a_1^{-\epsilon}\zeta(2\epsilon, c_1)$, taken from its definition, to find that for the $(2+1)$-D case,

$$E_2(-1, \lambda_1, \lambda_2, a_1, a_2) = a_2\zeta(0, \lambda_1)\zeta(-2, \lambda_2) + a_1\zeta(-2, \lambda_1)\zeta(0, \lambda_2)$$

$$= -\frac{1}{3}(\lambda_1 - \frac{1}{2})(\lambda_2 - \frac{1}{2})[a_1\lambda_1(1-\lambda_1) + a_2\lambda_2(1-\lambda_2)], \tag{A.51}$$

$$E_2(0, \lambda_1, \lambda_2, a_1, a_2) = \zeta(0, \lambda_1)\zeta(0, \lambda_2) = (1/2 - \lambda_1)(1/2 - \lambda_2). \tag{A.52}$$

For the $(3+1)$-D case, we substitute in the expression of E_2 to the recursion relation of Eq. (A.50) to find

that

$$
\begin{aligned}
&E_3(-1,\lambda_1,\lambda_2,\lambda_3,a_1,a_2,a_3)\\
&=\zeta(0,\lambda_1)E_2(-1,\lambda_2,\lambda_3,a_2,a_3)+a_1\zeta(-2,\lambda_1)E_2(0,\lambda_2,\lambda_3,a_2,a_3)\\
&\quad -a_1\frac{1}{3}\lambda_1(\lambda_1-1)(\lambda_1-1/2)(1/2-\lambda_2)(1/2-\lambda_3)\\
&=\frac{1}{3}(\lambda_1-\frac{1}{2})(\lambda_2-\frac{1}{2})(\lambda_3-\frac{1}{2})[a_1\lambda_1(1-\lambda_1)+a_2\lambda_2(1-\lambda_2)+a_3\lambda_3(1-\lambda_3)],
\end{aligned}
\tag{A.53}
$$

$$
\begin{aligned}
&E_3(0,\lambda_1,\lambda_2,\lambda_3,a_1,a_2,a_3)\\
&=\zeta(0,\lambda_1)E_2(0,\lambda_2,\lambda_3,a_2,a_3)=(1/2-\lambda_1)(1/2-\lambda_2)(1/2-\lambda_3).
\end{aligned}
\tag{A.54}
$$

To complete the calculation of the C matrix under T-transform, we must calculate G, corresponding to the summation over all complex numbers $\mathbb{Z}$, from the expression of the recursion relation, E, as the zeta function contained within E is defined as the summation over positive integers. To accomplish this, we use the following identity[184],

$$
\begin{aligned}
&G_1(\epsilon,\lambda)\equiv\sum_{n=-\infty}^{n=\infty}((n+\lambda)^2)^{-\epsilon}=(\sum_{n=-\infty}^{n=-1}+\sum_{n=0}^{n=\infty})((n+\lambda)^2)^{-\epsilon}\\
&=\sum_{n=0}^{n=\infty}((n+1-\lambda)^2)^{-\epsilon}+\sum_{n=0}^{n=\infty}((n+\lambda)^2)^{-\epsilon}=E_1(\epsilon,\lambda)+E_1(\epsilon,1-\lambda).
\end{aligned}
\tag{A.55}
$$

When considering the $(2+1)$-D version of Eq. (A.55), we learn that

$$
\begin{aligned}
G_2(\epsilon,\lambda_1,\lambda_2)&=E_2(\epsilon,\lambda_1,\lambda_2)+E_2(\epsilon,1-\lambda_1,\lambda_2)\\
&\quad +E_2(\epsilon,\lambda_1,1-\lambda_2)+E_2(\epsilon,1-\lambda_1,1-\lambda_2).
\end{aligned}
\tag{A.56}
$$

Finally, for the $(3+1)$-D version of Eq. (A.55), the result may be written as

$$
\begin{aligned}
G_3(\epsilon,\lambda_1,\lambda_2,\lambda_3)&=E_3(\epsilon,\lambda_1,\lambda_2,\lambda_3)+E_3(\epsilon,1-\lambda_1,\lambda_2,\lambda_3)\\
&\quad +E_3(\epsilon,\lambda_1,1-\lambda_2,\lambda_3)+E_3(\epsilon,\lambda_1,\lambda_2,1-\lambda_3)\\
&\quad +E_3(\epsilon,\lambda_1,1-\lambda_2,1-\lambda_3)+E_3(\epsilon,1-\lambda_1,\lambda_2,1-\lambda_3)\\
&\quad +E_3(\epsilon,1-\lambda_1,1-\lambda_2,\lambda_3)+E_3(\epsilon,1-\lambda_1,1-\lambda_2,1-\lambda_3)
\end{aligned}
\tag{A.57}
$$

Nonetheless, when $\epsilon=0$ or $\epsilon=-1$, then the calculated expressions of the Epstein-Zeta functions in Eq.

(A.51) and Eq. (A.53), namely E_2 and E_3, may be simplified to satisfy

$$E_2(\epsilon, \lambda_1, \lambda_2) = -E_2(\epsilon, 1-\lambda_1, \lambda_2) = -E_2(\epsilon, \lambda_1, 1-\lambda_2), \tag{A.58}$$

and

$$\begin{aligned} E_3(\epsilon, \lambda_1, \lambda_2, \lambda_3) &= -E_3(\epsilon, 1-\lambda_1, \lambda_2, \lambda_3) \\ = -E_3(\epsilon, \lambda_1, 1-\lambda_2, \lambda_3) &= -E_3(\epsilon, \lambda_1, \lambda_2, 1-\lambda_3), \end{aligned} \tag{A.59}$$

which yields the final sum over the complex numbers

$$G_2(\epsilon, \lambda_1, \lambda_2) = G_3(\epsilon, \lambda_1, \lambda_2, \lambda_3) = 0. \tag{A.60}$$

Finally, using (A.60) and substituting the result into Eq. (28) and Eq. (29), we find that the contributions to the modular anomaly from the T modular transformation in $(2+1)$-D is

$$arg(det(C_T^{2D})) = 0, \tag{A.61}$$

meanwhile, in $(3+1)$-D, the contribution is

$$arg(det(C_T^{3D})) = 0. \tag{A.62}$$

A.7.2 2.C matrix under the S transformation

We derive the expression of g_3 from the expansion method used in Eq. (A.55), we find

$$\begin{aligned} & g_3(0, \lambda_1, \lambda_2, \lambda_3, a_1, a_2, a_3) \\ &= E_3(0, \lambda_1, \lambda_2, \lambda_3, a_1, a_2, a_3) + E_3(0, 1-\lambda_1, \lambda_2, \lambda_3, a_1, a_2, a_3) \\ &+ E_3(0, \lambda_1, 1-\lambda_2, \lambda_3, a_1, a_2, a_3) + E_3(0, 1-\lambda_1, 1-\lambda_2, \lambda_3, a_1, a_2, a_3) = 0. \end{aligned} \tag{A.63}$$

As a result, the contribution of Eq. (38) vanishes and we conclude that the contributions to the modular anomaly resulting from the S transformation in $(2+1)$-D to be

$$arg(det(C_S^{2D})) = 0, \tag{A.64}$$

and in $(3+1)$-D

$$arg(det(C_S^{3D})) = 0. \tag{A.65}$$

A.8 Numerical Calculation of the Casimir Energy

Within this section, we introduce a numerical regularization scheme to calculate the Casimir energy in order to place our analytical regularization contained within the main text on a solid foundation. We start from the action of $(2+1)$-D theory given as

$$\begin{aligned} S_{\lambda_0\lambda_1\lambda_2}[\bar{\psi},\psi] &= -\beta L_x L_y \int_0^1\int_0^1\int_0^1 dxdyd\tau\bar{\psi}_\lambda[\sigma_0\partial_\tau/\beta - i\sigma_x\partial_x/L_x - i\sigma_y\partial_y/L_y]\psi_\lambda \\ &= -\int_0^1\int_0^1\int_0^1 dxdyd\tau\bar{\psi}_\lambda(\sigma_0 L_x L_y, i\sigma_x\beta L_y, i\sigma_y\beta L_x)(\partial_\tau,-\partial_x,-\partial_y)^T\psi_\lambda. \end{aligned} \tag{A.66}$$

Under a modular transform $A_{\mu\nu}$ defined in Eq. (A.31), we have

$$\begin{aligned} & S_{\lambda_0\lambda_1\lambda_2}[\bar{\psi}_\lambda,\psi_\lambda] \\ &= -\int_0^1\int_0^1\int_0^1 dxdyd\tau\bar{\psi}_\lambda(\sigma_0 L_x L_y, i\sigma_x\beta L_y, i\sigma_y\beta L_x)A^{-1}(\partial_\tau,-\partial_x,-\partial_y)^T\psi_\lambda. \\ &= -\int_0^1\int_0^1\int_0^1 dxdyd\tau\bar{\psi}_\lambda(L_3\partial_\tau - L_1\partial_x - L_2\partial_y)\psi_\lambda, \end{aligned} \tag{A.67}$$

The partition function of Eq. (A.67), after having been diagonalized, is given as

$$\begin{aligned} & Z_{\lambda_0\lambda_1\lambda_2} \\ &= \prod_{n_0,n_1,n_2=-\infty}^{\infty} \det[\frac{1}{L_3}(2\pi i L_3(n_0+\lambda_0) - 2\pi i L_1(n_1+\lambda_1) - 2\pi i L_2(n_2+\lambda_2))] \\ &= \prod_{n_1,n_2=-\infty}^{\infty} \det[I_2 - \exp(i2\pi[z_1(n_1+\lambda_1) + z_2(n_2+\lambda_2)] + \lambda_0)] \\ &= \prod_{n_1,n_2=-\infty}^{\infty} (1 - e^{2i\pi(z_{10}\widetilde{n}_1 + z_{20}\widetilde{n}_2 + \lambda_0) + 2\pi E(n_1,n_2)})(1 - e^{2i\pi(z_{10}\widetilde{n}_1 + z_{20}\widetilde{n}_2 + \lambda_0) - 2\pi E(n_1,n_2)}), \end{aligned} \tag{A.68}$$

where $z_i \equiv z_{i0}I_2 + i\sum_{j=1}^2 z_{ij}\sigma_j \equiv \frac{L_i}{L_3}$, $\widetilde{n}_i = n_i + \lambda_i$ and $E_2(n_1,n_2) = \sqrt{\sum_{i=1,2,3}[z_{1i}\widetilde{n}_1 + z_{2i}\widetilde{n}_2]^2}$, and I_2 is the $2x2$ identity matrix.

In $(3+1)$-D, we just add z-directional momentum. Similarly, we have

$$Z_{\lambda_0,\lambda_1,\lambda_2,\lambda_3} = \prod_{n_1,n_2,n_3=-\infty}^{\infty} (1 - e^{2i\pi(\lambda_0+z_{10}\widetilde{n}_1+z_{20}\widetilde{n}_2+z_{30}\widetilde{n}_3)+2\pi E_3(n_1,n_2,n_3)}) \times(1 - e^{2i\pi(\lambda_0+z_{10}\widetilde{n}_1+z_{20}\widetilde{n}_2+z_{30}\widetilde{n}_3)-2\pi E_3(n_1,n_2,n_3)}) \tag{A.69}$$

where $E_3(n_1,n_2,n_3) = \sqrt{\sum_{i=1,2,3}[z_{1i}\widetilde{n}_1 + z_{2i}\widetilde{n}_2 + z_{3i}\widetilde{n}_3]^2}$.

In $(2+1)$-D and $(3+1)$-D, we extract the divergent part of the partition function so that we may use numerical regularization to find the anomalous contribution. In $(2+1)$-D, the divergent part is represented as

$$F_2^A = \sum_{n_1,n_2} 2i\pi(z_{10}n_1 + z_{20}n_2) + 2\pi E_2(n_1,n_2) \tag{A.70}$$

and, in $(3+1)$-D, the contribution is

$$F_3^A = \sum_{n_1,n_2,n_3} 2i\pi(z_{10}n_1 + z_{20}n_2 + z_{30}n_3) + 2\pi E_3(n_1,n_2,n_3). \tag{A.71}$$

In general, we can evaluate the sum of a divergent function, $F^A = \sum_{\mathbf{m}} f_A(\mathbf{m})$, using following identity

$$F^A = \lim_{\epsilon\to 0} -\frac{\partial}{\partial\epsilon}\sum_{\mathbf{m}} e^{-f_A\epsilon}, \tag{A.72}$$

that may be numerically evaluated using $\sum_{\mathbf{m}} e^{-f_A(\mathbf{m})\epsilon}$. Therefore, from the numerical regularization, we extract the value of $O(\epsilon)$ by fitting the curve as a function of ϵ to evaluate F_A. From Eq. (A.72), we find that the coefficient of $O(\epsilon)$ is the regularized Casimir energy. Nonetheless, as this quantity diverges when $\epsilon \to 0$, it has poles of different orders in the expansion of $1/\epsilon$. For the sake of numerical stability, we need to subtract the divergent part of the partition function by calculating the analytical form of the poles. To calculate the divergent part analytically, we use the Euler-Maclaurin formula to change the sum $\sum_{\mathbf{m}} e^{-f_A\epsilon}$ to a integral. The Euler-Maclaurin formula states that we can express a sum, $\sum_{i=m+1}^{n} f(i)$, by

$$\sum_{i=m+1}^{n} f(i) = \int_m^n dx f(x) + B_1(f(n) - f(m)) + \sum_{k=1}^{p} \frac{B_{2k}}{(2k)!}(f^{(2k-1)}(n) - f^{(2k-1)}(m)) + R. \tag{A.73}$$

where B_n is the n-th Bernoulli number($B_1 = 1/2$) and R is an error term which becomes smaller in higher

p-th order approximations. Consider (2+1)-D, all other terms except the integral can contribute the positive orders of ϵ. The pole only comes from the integral.

$$\begin{aligned}
&\sum_{n_1,n_2=-\infty}^{\infty} e^{-2\pi(i(z_{10}n_1+z_{20}n_2)+E_2(n_1,n_2))\epsilon} \\
&= \sum_{n_2=-\infty}^{\infty}\int_{-\infty}^{\infty} dx e^{-2\pi(i(z_{10}x+z_{20}n_2)+E_2(x,n_2))\epsilon} \\
&= \int_{-\infty}^{\infty} dxdy e^{-2\pi(i(z_{10}x+z_{20}y)+E_2(x,y))\epsilon} \\
&= \frac{1}{\epsilon^2}\int_{-\infty}^{\infty} dxdy e^{-2\pi(i(z_{10}x+z_{20}y)+E_2(x,y))}.
\end{aligned} \tag{A.74}$$

Finally, in $(2+1)$-D, the integral expression which contributes to the pole is given by

$$S_{2D} = \frac{1}{\epsilon^2}\int_{-\infty}^{\infty}\int_{-\infty}^{\infty} dxdy e^{-2\pi(E_2(x,y)+i(z_{10}x+z_{20}y))}. \tag{A.75}$$

The above numerical regularization procedure may then be repeated with by adding in an additional coordinate so that, in $(3+1)$-D, we have

$$S_{3D} = \frac{1}{\epsilon^3}\int_{-\infty}^{\infty}\int_{-\infty}^{\infty}\int_{-\infty}^{\infty} dxdydz e^{-2\pi(E_3(x,y,z)+i(z_{10}x+z_{20}y+z_{30}z))}. \tag{A.76}$$

We calculate the integral part to evaluate the pole. In general, the expression for the integral in $(d+1)$-D is given by

$$\begin{aligned}
&\frac{1}{\epsilon^d}\int_{-\infty}^{\infty} d^d x e^{-2\pi(E_d(\mathbf{x})+i\sum_{j=1}^{d} z_{j0}x_j)} \\
&= \frac{1}{\epsilon^d}[\frac{1}{\sqrt{det(V)}}\int_{-\infty}^{\infty} d^d x' e^{-2\pi(\sum_{i=1}^{d}(x_i')^2+i\sum_{j,k=1}^{d} z_{j0}w_{kj}x_k')}],
\end{aligned} \tag{A.77}$$

where $x_i' = \sum_{j=1}^{d} z_{ji}x_j$ and w_{ij} is the matrix component of the inverse matrix of z_{ij} when i,j are positive

integers. We change to the polar coordinate to solve the above integral expression.

$$
\tag{A.78}
$$

$$
= \frac{1}{\epsilon^d \sqrt{det(V)}} \int_0^\infty dr \int_0^\pi d\theta S_{d-2} r^{d-1} sin^{d-2}\theta e^{-2\pi r(1+i|\sum_{j,k,l} z_{j0} w_{kj} w_{kl} z_{l0}| cos\theta)} \tag{A.79}
$$

$$
= \frac{1}{\epsilon^d \sqrt{det(V)}} \int_0^\infty dr \int_0^\pi d\theta S_{d-2} r^{d-1} sin^{d-2}\theta e^{-2\pi r(1+i\sqrt{b^T V^{-1} b} cos\theta)} \tag{A.80}
$$

$$
= \frac{1}{(2\pi\epsilon)^d \sqrt{det(V)}} S_{d-2}\Gamma(d) \int_0^\pi d\theta \frac{sin^{d-2}\theta}{(1+i\sqrt{b^T V^{-1} b} cos\theta)^d} \tag{A.81}
$$

$$
= \frac{1}{(2\pi\epsilon)^d \sqrt{det(V)}} S_{d-2}\Gamma(d) \int_{-1}^1 dx \frac{(1-x^2)^{(d-3)/2}}{(1+i\sqrt{b^T V^{-1} b} x)^d}, \tag{A.82}
$$

where $V_{ij} = \sum_{k=1}^d z_{ik} z_{jk}$ and $b_i = z_{i0}$. When $d = 2$, we find

$$
= \frac{1}{(2\pi\epsilon)^d \sqrt{det(V)}} S_{d-2}\Gamma(d) \frac{\pi}{(1+b^T V^{-1} b)^{3/2}} \tag{A.83}
$$

$$
= \frac{1}{2\pi\epsilon^2 \sqrt{det(V)}(1+b^T V^{-1} b)^{3/2}}, \tag{A.84}
$$

and when $d = 3$, we find

$$
= \frac{1}{(2\pi\epsilon)^d} S_{d-2}\Gamma(d) \frac{2}{\sqrt{det(V)}(1+b^T V^{-1} b)^2} \tag{A.85}
$$

$$
= \frac{1}{\pi^2\epsilon^3 \sqrt{det(V)}(1+b^T V^{-1} b)^2} \tag{A.86}
$$

When a magnetic field is coupled to $(3+1)$-D edge, as seen in Eq. (41) in the main text, the divergent part of the unregularized free energy is given as,

$$
F_A = \sum_{n_z<0} 2\pi \frac{N_\phi \beta}{L_z}(n_z + \lambda_3) + \sum_{n_z=-\infty, n=1}^{\infty} 2\pi \frac{N_\phi \beta}{L_z} \sqrt{(n_z+\lambda_3)^2 + \alpha n}. \tag{A.87}
$$

where $\alpha = B_{field}(\frac{L_z}{2\pi})^2$, B_{field} is the magnetic field and N_ϕ is the Landau level degeneracy. We again write the expression of $\sum_{\mathbf{m}} e^{-f_A(\mathbf{m})\epsilon}$ as done in the case of the free fermions in $(2+1)$-D and $(3+1)$-D to calculate the divergent component. The first term results in the exponential expression

$$
S_1 = \sum_{n_z<0} e^{-2\pi\epsilon \frac{N_\phi \beta}{L_z}(n_z+\lambda_3)}, \tag{A.88}
$$

while the second term gives

$$S_2 = \sum_{n_z,n} e^{-2\pi\epsilon\frac{N_\phi\beta}{L_z}\sqrt{(n_z+\lambda_3)^2+\alpha n}}. \tag{A.89}$$

We change both S_1 and S_2 to integral forms and get the expressions of the poles.

$$Integral_1 = \int_{-\infty}^{-1} dx e^{-2\pi\epsilon\frac{N_\phi\beta}{L_z}(x+\lambda_3)} = -\frac{1}{2\pi\epsilon\frac{N_\phi\beta}{L_z}} e^{-2\pi\epsilon\frac{N_\phi\beta}{L_z}(\lambda_3-1)}, \tag{A.90}$$

$$Integral_2 = \int_{-\infty}^{\infty} dx \int_0^{\infty} dy e^{-2\pi\epsilon\frac{N_\phi\beta}{L_z}\sqrt{x^2+\alpha y}} = \frac{8}{\alpha(2\pi\epsilon N_\phi\frac{\beta}{L_z})^3}. \tag{A.91}$$

A.9 Regularization of gapped Landau level

Starting from the partition function of Eq. (41) in the main text, we find the divergent part of the free energy of gapped Landau levels is given by

$$F_{A,D} = \sum_{n_3=-\infty}^{\infty}\sum_{n=0}^{\infty}(Bn + B + (\frac{2\pi(n_3+\lambda_3)}{L_z})^2)^{1/2}. \tag{A.92}$$

By using the Hurwitz-Zeta function, defined by

$$\zeta_H(\epsilon, a) \equiv \sum_{n=0}^{\infty}(n+a)^{-\epsilon}. \tag{A.93}$$

We can rewrite the above divergent contribution to the partition function as,

$$F_{A,Dirac} = \sum_{n_3=-\infty}^{\infty}\sqrt{B}\zeta_H(-1/2, (2\pi(n_3+\lambda_3)/L_z)^2/B + 1). \tag{A.94}$$

Using the following Hurwitz-Zeta function identity[184],

$$\zeta_H(\epsilon, x+y) = \sum_{k=0}^{\infty}\frac{\Gamma(\epsilon+k)}{\Gamma(\epsilon)\Gamma(k+1)}\zeta_H(\epsilon+k, x)(-y)^k, \tag{A.95}$$

We may represent the divergent contribution as

$$\zeta_H(-1/2, 1+\frac{(2\pi(n_3+\lambda_3)/L_z)^2}{B}) \tag{A.96}$$
$$=\sum_{k=0}^{\infty}\frac{\Gamma(k-1/2)}{\Gamma(-1/2)\Gamma(k+1)}\zeta(-1/2+k,1)(-\frac{(2\pi(n_3+\lambda_3)/L_z)^2}{B})^k.$$

Then, we rewrite the divergent part of the partition function of the gapped Landau levels as,

$$F_{A,D}=\sum_{n_3=-\infty}^{\infty}\sum_{k=0}^{\infty}\frac{B^{1/2-k}\Gamma(k-1/2)}{\Gamma(-1/2)\Gamma(k+1)}\zeta(-1/2+k,1)(-(\frac{2\pi}{L_z})^2)^k(n_3+\lambda_3)^{2k} \tag{A.97}$$
$$=\sum_{k=0}^{\infty}\frac{B^{1/2-k}\Gamma(k-1/2)}{\Gamma(-1/2)\Gamma(k+1)}\zeta(-1/2+k,1)(-(\frac{2\pi}{L_z})^2)^k[\sum_{n_3=-\infty}^{\infty}(n_3+\lambda_3)^{2k}]$$

From Eq. (A.55), we find that

$$\sum_{n_3=-\infty}^{\infty}(n_3+\lambda_3)^{2k}=G_1(-k,\lambda_3)=E_1(-k,\lambda_3)+E_1(-k,1-\lambda_3) \tag{A.98}$$
$$=\zeta_H(-2k,\lambda_3)+\zeta_H(-2k,1-\lambda_3)=-\frac{B_{2k+1}(\lambda_3)+B_{2k+1}(1-\lambda_3)}{2k+1}=0.$$

Therefore, we conclude that the divergent part of the partition function is regularized to be zero.

References

[1] Y. Kim, T. M. Philip, M. J. Park, and M. J. Gilbert, "Topological superconductivity in an ultrathin, magnetically-doped topological insulator proximity coupled to a conventional superconductor," *Phys. Rev. B*, vol. 94, p. 235434, Dec 2016.

[2] M. J. Park, J. Yang, Y. Kim, and M. J. Gilbert, "Fulde-ferrell states in inverse proximity-coupled magnetically doped topological heterostructures," *Phys. Rev. B*, vol. 96, p. 064518, Aug 2017.

[3] Y. Kim, M. J. Park, and M. J. Gilbert, "Probing unconventional superconductivity in inversion-symmetric doped weyl semimetal," *Phys. Rev. B*, vol. 93, p. 214511, Jun 2016.

[4] M. J. Park, B. Basa, and M. J. Gilbert, "Disorder-induced phase transitions of type-ii weyl semimetals," *Phys. Rev. B*, vol. 95, p. 094201, Mar 2017.

[5] M. J. Park, C. Fang, B. A. Bernevig, and M. J. Gilbert, "Modular anomalies in $(2+1)$- and $(3+1)$-dimensional edge theories," *Phys. Rev. B*, vol. 95, p. 235130, Jun 2017.

[6] K. v. Klitzing, G. Dorda, and M. Pepper *Phys. Rev. Lett*, vol. 45, p. 494, 1980.

[7] K. von Klitzing, "The quantized hall effect," *Rev. Mod. Phys.*, vol. 58, pp. 519–531, Jul 1986.

[8] R. B. Laughlin *Phys. Rev. B*, vol. 23, p. 5632, 1981.

[9] K. Fujikawa *Phys. Rev. Lett.*, vol. 42, p. 1195, 1979.

[10] K. Fujikawa *Phys. Rev. D*, vol. 21, p. 2848, 1980.

[11] H. Nielsen and M. Ninomiya *Phys. Lett. B*, vol. 130, p. 389, 1983.

[12] S. Adler *Phys. Rev.*, vol. 5, p. 177, 1969.

[13] H. Nielsen and M. Ninomiya *Phys. Lett. B*, vol. 105, p. 219, 1981.

[14] F. D. M. Haldane, "Model for a quantum hall effect without landau levels: Condensed-matter realization of the "parity anomaly"," *Phys. Rev. Lett.*, vol. 61, pp. 2015–2018, Oct 1988.

[15] D. J. Thouless, M. Kohmoto, M. P. Nightingale, and M. den Nijs, "Quantized hall conductance in a two-dimensional periodic potential," *Phys. Rev. Lett.*, vol. 49, pp. 405–408, Aug 1982.

[16] C. L. Kane and E. J. Mele, "Quantum spin hall effect in graphene," *Phys. Rev. Lett.*, vol. 95, p. 226801, Nov 2005.

[17] B. A. Bernevig and S.-C. Zhang, "Quantum spin hall effect," *Phys. Rev. Lett.*, vol. 96, p. 106802, Mar 2006.

[18] L. Fu, C. L. Kane, and E. J. Mele, "Topological insulators in three dimensions," *Phys. Rev. Lett.*, vol. 98, p. 106803, Mar 2007.

[19] S. Murakami *New Journal of Physics*, vol. 9, no. 9, p. 356, 2007.

[20] M. Z. Hasan, S.-Y. Xu, I. Belopolski, and S.-M. Huang, "Discovery of weyl fermion semimetals and topological fermi arc states," *Annual Review of Condensed Matter Physics*, vol. 8, no. 1, pp. 289–309, 2017.

[21] A. A. Soluyanov, D. Gresch, Z. Wang, Q. Wu, M. Troyer, X. Dai, and B. A. Bernevig *Nature*, vol. 527, p. 495, 2015.

[22] A. A. Burkov and L. Balents, "Weyl semimetal in a topological insulator multilayer," *Phys. Rev. Lett.*, vol. 107, p. 127205, Sep 2011.

[23] A. P. Schnyder, S. Ryu, A. Furusaki, and A. W. W. Ludwig, "Classification of topological insulators and superconductors in three spatial dimensions," *Phys. Rev. B*, vol. 78, p. 195125, Nov 2008.

[24] A. Kitaev, "Periodic table for topological insulators and superconductors," *AIP Conf. Proc.*, vol. 1134, p. 22, 2008.

[25] L. Fu and C. L. Kane, "Superconducting proximity effect and majorana fermions at the surface of a topological insulator," *Phys. Rev. Lett.*, vol. 100, p. 096407, Mar 2008.

[26] R. M. Lutchyn, J. D. Sau, and S. Das Sarma, "Majorana Fermions and a Topological Phase Transition in Semiconductor-Superconductor Heterostructures," *Phys. Rev. Lett.*, vol. 105, p. 077001, aug 2010.

[27] V. Mourik, K. Zuo, S. M. Frolov, S. R. Plissard, E. P. a. M. Bakkers, and L. P. Kouwenhoven, "Signatures of Majorana Fermions in Hybrid Superconductor-Semiconductor Nanowire Devices," *Science*, vol. 336, pp. 1003–1007, may 2012.

[28] S. Nadj-Perge, I. K. Drozdov, J. Li, H. Chen, S. Jeon, J. Seo, A. H. MacDonald, B. A. Bernevig, and A. Yazdani, "Observation of Majorana fermions in ferromagnetic atomic chains on a superconductor," *Science*, vol. 346, pp. 602–607, oct 2014.

[29] J. Jang, D. G. Ferguson, V. Vakaryuk, R. Budakian, S. B. Chung, P. M. Goldbart, and Y. Maeno, "Observation of half-height magnetization steps in Sr2RuO4.," *Science*, vol. 331, pp. 186–8, jan 2011.

[30] C. Kallin and A. J. Berlinsky, "Is Sr 2 RuO 4 a chiral p-wave superconductor?," *J. Phys. Condens. Matter*, vol. 21, p. 164210, apr 2009.

[31] C. Kallin, "Chiral p-wave order in Sr 2 RuO 4," *Reports Prog. Phys.*, vol. 75, p. 042501, apr 2012.

[32] Y. S. Hor, A. J. Williams, J. G. Checkelsky, P. Roushan, J. Seo, Q. Xu, H. W. Zandbergen, A. Yazdani, N. P. Ong, and R. J. Cava, "Superconductivity in <math display="inline"> <msub> <mi>Cu</mi> <mi>x</mi> </msub> <msub> <mi>Bi</mi> <mn>2</mn> </msub> <msub> <mi>Se</mi> <mn>3</mn> </msub> </math> and its Implications for Pairing in the Undoped Topological Insulator," *Phys. Rev. Lett.*, vol. 104, p. 057001, feb 2010.

[33] L. Fu and E. Berg, "Odd-Parity Topological Superconductors: Theory and Application to CuxBi2Se3," *Phys. Rev. Lett.*, vol. 105, p. 097001, aug 2010.

[34] F. F. Tafti, T. Fujii, A. Juneau-Fecteau, S. René de Cotret, N. Doiron-Leyraud, A. Asamitsu, and L. Taillefer, "Superconductivity in the noncentrosymmetric half-Heusler compound LuPtBi: A candidate for topological superconductivity," *Phys. Rev. B*, vol. 87, p. 184504, may 2013.

[35] J. D. Sau, R. M. Lutchyn, S. Tewari, and S. Das Sarma, "Generic New Platform for Topological Quantum Computation Using Semiconductor Heterostructures," *Phys. Rev. Lett.*, vol. 104, p. 040502, jan 2010.

[36] S. Nadj-Perge, I. K. Drozdov, B. A. Bernevig, and A. Yazdani, "Proposal for realizing Majorana fermions in chains of magnetic atoms on a superconductor," *Phys. Rev. B*, vol. 88, p. 020407, jul 2013.

[37] Y. Oreg, G. Refael, and F. von Oppen, "Helical Liquids and Majorana Bound States in Quantum Wires," *Phys. Rev. Lett.*, vol. 105, p. 177002, oct 2010.

[38] Y. Tanaka and T. Yanagisawa, "Chiral state in three-gap superconductors," *Solid State Commun.*, vol. 150, pp. 1980–1982, nov 2010.

[39] H.-H. Hung, P. Ghaemi, T. L. Hughes, and M. J. Gilbert, "Vortex lattices in the superconducting phases of doped topological insulators and heterostructures," *Phys. Rev. B*, vol. 87, p. 035401, jan 2013.

[40] V. A. Kul'bachinskii, A. Y. Kaminskii, K. Kindo, Y. Narumi, K. Suga, P. Lostak, and P. Svanda, "Low-temperature ferromagnetism in a new diluted magnetic semiconductor Bi2x FexTe3," *J. Exp. Theor. Phys. Lett.*, vol. 73, pp. 352–356, apr 2001.

[41] J. S. Dyck, P. Hájek, P. Lošt'ák, and C. Uher, "Diluted magnetic semiconductors based on Sb 2 x V x Te 3 (0.01 <˜ x <˜ 0 . 0 3)," *Phys. Rev. B*, vol. 65, p. 115212, mar 2002.

[42] Y. S. Hor, P. Roushan, H. Beidenkopf, J. Seo, D. Qu, J. G. Checkelsky, L. A. Wray, D. Hsieh, Y. Xia, S.-Y. Xu, D. Qian, M. Z. Hasan, N. P. Ong, A. Yazdani, and R. J. Cava, "Development of ferromagnetism in the doped topological insulator Bi 2 x Mn x Te 3," *Phys. Rev. B*, vol. 81, p. 195203, may 2010.

[43] R. Yu, W. Zhang, H.-J. Zhang, S.-C. Zhang, X. Dai, and Z. Fang, "Quantized anomalous Hall effect in magnetic topological insulators.," *Science*, vol. 329, pp. 61–4, jul 2010.

[44] S.-Y. Xu, M. Neupane, C. Liu, D. Zhang, A. Richardella, L. Andrew Wray, N. Alidoust, M. Leandersson, T. Balasubramanian, J. Sánchez-Barriga, O. Rader, G. Landolt, B. Slomski, J. Hugo Dil, J. Osterwalder, T.-R. Chang, H.-T. Jeng, H. Lin, A. Bansil, N. Samarth, and M. Zahid Hasan, "Hedgehog spin texture and Berry's phase tuning in a magnetic topological insulator," *Nat. Phys.*, vol. 8, pp. 616–622, jun 2012.

[45] H. Jiang, Z. Qiao, H. Liu, and Q. Niu, "Quantum anomalous Hall effect with tunable Chern number in magnetic topological insulator film," *Phys. Rev. B*, vol. 85, p. 045445, jan 2012.

[46] Y. Zhang, K. He, C.-Z. Chang, C.-L. Song, L.-L. Wang, X. Chen, J.-F. Jia, Z. Fang, X. Dai, W.-Y. Shan, S.-Q. Shen, Q. Niu, X.-L. Qi, S.-C. Zhang, X.-C. Ma, and Q.-K. Xue, "Crossover of the three-dimensional topological insulator bi2se3 to the two-dimensional limit," *Nat Phys*, vol. 6, pp. 584–588, Aug 2010.

[47] Q. Liu, C.-X. Liu, C. Xu, X.-L. Qi, and S.-C. Zhang, "Magnetic Impurities on the Surface of a Topological Insulator," *Phys. Rev. Lett.*, vol. 102, p. 156603, apr 2009.

[48] G. Rosenberg and M. Franz, "Surface magnetic ordering in topological insulators with bulk magnetic dopants," *Phys. Rev. B*, vol. 85, p. 195119, may 2012.

[49] W. Qin and Z. Zhang, "Persistent Ferromagnetism and Topological Phase Transition at the Interface of a Superconductor and a Topological Insulator," *Phys. Rev. Lett.*, vol. 113, p. 266806, dec 2014.

[50] T. Thonhauser, "Theory of Orbital Magnetization in Solids," *Int. J. Mod. Phys. B*, vol. 25, pp. 1429–1458, apr 2011.

[51] A. Volkov, P. Magne, B. van Wees, and T. Klapwijk, "Proximity and josephson effects in superconductor-two-dimensional electron gas planar junctions," *Physica C: Superconductivity*, vol. 242, no. 3, pp. 261 – 266, 1995.

[52] S.-Y. Xu, N. Alidoust, I. Belopolski, A. Richardella, C. Liu, M. Neupane, G. Bian, S.-H. Huang, R. Sankar, C. Fang, B. Dellabetta, W. Dai, Q. Li, M. J. Gilbert, F. Chou, N. Samarth, and M. Z. Hasan, "Momentum-space imaging of cooper pairing in a half-dirac-gas topological superconductor," *Nat Phys*, vol. 10, pp. 943–950, Dec 2014. Article.

[53] M. Tinkham, *Introduction to Superconductivity*. McGraw-Hill Inc., 1996.

[54] T. D. Stanescu, J. D. Sau, R. M. Lutchyn, and S. Das Sarma, "Proximity effect at the superconductortopological insulator interface," *Phys. Rev. B*, vol. 81, p. 241310, jun 2010.

[55] A. M. Black-Schaffer, "Self-consistent superconducting proximity effect at the quantum spin hall edge," *Phys. Rev. B*, vol. 83, p. 060504, Feb 2011.

[56] S. Murakami, "Phase transition between the quantum spin hall and insulator phases in 3d: emergence of a topological gapless phase," *New Journal of Physics*, vol. 9, no. 9, p. 356, 2007.

[57] T. Fukui, Y. Hatsugai, and H. Suzuki, "Chern numbers in discretized brillouin zone: Efficient method of computing (spin) hall conductances," *Journal of the Physical Society of Japan*, vol. 74, no. 6, pp. 1674–1677, 2005.

[58] Y. Tanaka, T. Yokoyama, and N. Nagaosa, "Manipulation of the majorana fermion, andreev reflection, and josephson current on topological insulators," *Phys. Rev. Lett.*, vol. 103, p. 107002, Sep 2009.

[59] B. A. Bernevig, *Topological insulators and topological superconductors*. Princeton, 2013.

[60] A. A. Zyuzin and A. A. Burkov, "Thin topological insulator film in a perpendicular magnetic field," *Phys. Rev. B*, vol. 83, p. 195413, may 2011.

[61] C.-K. Chiu, M. J. Gilbert, and T. L. Hughes, "Vortex lines in topological insulator-superconductor heterostructures," *Phys. Rev. B*, vol. 84, p. 144507, Oct 2011.

[62] H. Zhang, C.-X. Liu, X.-L. Qi, X. Dai, Z. Fang, and S.-C. Zhang, "Topological insulators in bi2se3, bi2te3 and sb2te3 with a single dirac cone on the surface," *Nat Phys*, vol. 5, pp. 438–442, Jun 2009.

[63] C.-K. Chiu, "Nontrivial surface topological physics from strong and weak topological insulators and superconductors," *arXiv:1410.1117*.

[64] S. Datta, *Quantum Transport: Atom to Transistor*. , Cambridge University Press, 2005.

[65] W.-Y. Shan, H.-Z. Lu, and S.-Q. Shen, "Effective continuous model for surface states and thin films of three-dimensional topological insulators," *New Journal of Physics*, vol. 12, no. 4, p. 043048, 2010.

[66] M. H. Berntsen, O. Götberg, B. M. Wojek, and O. Tjernberg, "Direct observation of decoupled dirac states at the interface between topological and normal insulators," *Phys. Rev. B*, vol. 88, p. 195132, Nov 2013.

[67] P. D. Gennes, *Superconductivity of Metals and Alloys*. W. A. Benjamin, New York, 1966.

[68] Y. Zhang, K. He, C.-Z. Chang, C.-L. Song, L.-L. Wang, X. Chen, J.-F. Jia, Z. Fang, X. Dai, W.-Y. Shan, S.-Q. Shen, Q. Niu, X.-L. Qi, S.-C. Zhang, X.-C. Ma, and Q.-K. Xue, "Crossover of the three-dimensional topological insulator bi2se3 to the two-dimensional limit," *Nature Physics*, vol. 6, pp. 584 EP –, Jun 2010.

[69] G. Zwicknagl, S. Jahns, and P. Fulde, "Critical magnetic field of ultra-thin superconducting films and interfaces," *Journal of the Physical Society of Japan*, vol. 86, no. 8, p. 083701, 2017.

[70] Z. Zheng, M. Gong, Y. Zhang, X. Zou, C. Zhang, and G. Guo, "Fflo superfluids in 2d spin-orbit coupled fermi gases," *Scientific Reports*, vol. 4, pp. 6535 EP –, Oct 2014. Article.

[71] H. Hu and X.-J. Liu, "Fuldeferrell superfluidity in ultracold fermi gases with rashba spinorbit coupling," *New Journal of Physics*, vol. 15, no. 9, p. 093037, 2013.

[72] W. Zhang and W. Yi, "Topological fuldeferrelllarkinovchinnikov states in spinorbit-coupled fermi gases," *Nature communications*, vol. 4, p. 2711, 2013.

[73] Z. Zheng, M. Gong, X. Zou, C. Zhang, and G. Guo, "Route to observable fulde-ferrell-larkin-ovchinnikov phases in three-dimensional spin-orbit-coupled degenerate fermi gases," *Phys. Rev. A*, vol. 87, p. 031602, Mar 2013.

[74] G. Y. Cho, J. H. Bardarson, Y.-M. Lu, and J. E. Moore *Phys. Rev. B*, vol. 86, p. 214514, 2012.

[75] H. Wei, S.-P. Chao, and V. Aji, "Odd-parity superconductivity in weyl semimetals," *Phys. Rev. B*, vol. 89, p. 014506, Jan 2014.

[76] P. Fulde and R. A. Ferrell, "Superconductivity in a strong spin-exchange field," *Phys. Rev.*, vol. 135, pp. A550–A563, Aug 1964.

[77] A. I. larkin and Y. N. Ovchinnikov, "Nonuniform state of superconductors," *Zh. Eksp. Teor. Fiz.*, vol. 47, pp. 1136–1146, 1964. [Sov. Phys. JETP20,762(1965)].

[78] Y.-a. Liao, A. S. C. Rittner, T. Paprotta, W. Li, G. B. Partridge, R. G. Hulet, S. K. Baur, and E. J. Mueller, "Spin-imbalance in a one-dimensional fermi gas," *Nature*, vol. 467, pp. 567–569, Sep 2010.

[79] S. Hart, H. Ren, M. Kosowsky, G. Ben-Shach, P. Leubner, C. Brune, H. Buhmann, L. W. Molenkamp, B. I. Halperin, and A. Yacoby, "Controlled finite momentum pairing and spatially varying order parameter in proximitized hgte quantum wells," *Nat Phys*, vol. advance online publication, Sep 2016. Article.

[80] J.-P. Xu, M.-X. Wang, Z. L. Liu, J.-F. Ge, X. Yang, C. Liu, Z. A. Xu, D. Guan, C. L. Gao, D. Qian, Y. Liu, Q.-H. Wang, F.-C. Zhang, Q.-K. Xue, and J.-F. Jia, "Experimental detection of a majorana mode in the core of a magnetic vortex inside a topological insulator-superconductor $bi_2te_3/nbse_2$ heterostructure," *Phys. Rev. Lett.*, vol. 114, p. 017001, Jan 2015.

[81] P. Zareapour, A. Hayat, S. Y. F. Zhao, M. Kreshchuk, A. Jain, D. C. Kwok, N. Lee, S.-W. Cheong, Z. Xu, A. Yang, G. D. Gu, S. Jia, R. J. Cava, and K. S. Burch, "Proximity-induced high-temperature superconductivity in the topological insulators bi2se3 and bi2te3," *Nature Communications*, vol. 3, pp. 1056 EP –, Sep 2012. Article.

[82] F. Yang, F. Qu, J. Shen, Y. Ding, J. Chen, Z. Ji, G. Liu, J. Fan, C. Yang, L. Fu, and L. Lu, "Proximity-effect-induced superconducting phase in the topological insulator bi_2se_3," *Phys. Rev. B*, vol. 86, p. 134504, Oct 2012.

[83] S.-Y. Xu, C. Liu, A. Richardella, I. Belopolski, N. Alidoust, M. Neupane, G. Bian, N. Samarth, and M. Z. Hasan, "Fermi-level electronic structure of a topological-insulator/cuprate-superconductor based heterostructure in the superconducting proximity effect regime," *Phys. Rev. B*, vol. 90, p. 085128, Aug 2014.

[84] D. Zhang, J. Wang, A. M. DaSilva, J. S. Lee, H. R. Gutierrez, M. H. W. Chan, J. Jain, and N. Samarth, "Superconducting proximity effect and possible evidence for pearl vortices in a candidate topological insulator," *Phys. Rev. B*, vol. 84, p. 165120, Oct 2011.

[85] M.-X. Wang, C. Liu, J.-P. Xu, F. Yang, L. Miao, M.-Y. Yao, C. L. Gao, C. Shen, X. Ma, X. Chen, Z.-A. Xu, Y. Liu, S.-C. Zhang, D. Qian, J.-F. Jia, and Q.-K. Xue, "The coexistence of superconductivity and topological order in the bi2se3 thin films," *Science*, vol. 336, no. 6077, pp. 52–55, 2012.

[86] I. Sochnikov, A. J. Bestwick, J. R. Williams, T. M. Lippman, I. R. Fisher, D. Goldhaber-Gordon, J. R. Kirtley, and K. A. Moler, "Direct measurement of current-phase relations in superconductor/topological insulator/superconductor junctions," *Nano Letters*, vol. 13, no. 7, pp. 3086–3092, 2013. PMID: 23795666.

[87] S. Cho, B. Dellabetta, A. Yang, J. Schneeloch, Z. Xu, T. Valla, G. Gu, M. J. Gilbert, and N. Mason, "Symmetry protected josephson supercurrents in three-dimensional topological insulators," *Nature Communications*, vol. 4, pp. 1689 EP –, Apr 2013. Article.

[88] M.-X. Wang, P. Li, J.-P. Xu, Z.-L. Liu, J.-F. Ge, G.-Y. Wang, X. Yang, Z.-A. Xu, S.-H. Ji, C. L. Gao, D. Qian, W. Luo, C. Liu, and J.-F. Jia, "Interface structure of a topological insulator/superconductor heterostructure," *New Journal of Physics*, vol. 16, no. 12, p. 123043, 2014.

[89] C.-Z. Chang, J. Zhang, X. Feng, J. Shen, Z. Zhang, M. Guo, K. Li, Y. Ou, P. Wei, L.-L. Wang, Z.-Q. Ji, Y. Feng, S. Ji, X. Chen, J. Jia, X. Dai, Z. Fang, S.-C. Zhang, K. He, Y. Wang, L. Lu, X.-C. Ma, and Q.-K. Xue, "Experimental observation of the quantum anomalous hall effect in a magnetic topological insulator," *Science*, vol. 340, no. 6129, pp. 167–170, 2013.

[90] Y. L. Chen, J.-H. Chu, J. G. Analytis, Z. K. Liu, K. Igarashi, H.-H. Kuo, X. L. Qi, S. K. Mo, R. G. Moore, D. H. Lu, M. Hashimoto, T. Sasagawa, S. C. Zhang, I. R. Fisher, Z. Hussain, and Z. X. Shen, "Massive dirac fermion on the surface of a magnetically doped topological insulator," *Science*, vol. 329, no. 5992, pp. 659–662, 2010.

[91] T. Shoman, A. Takayama, T. Sato, S. Souma, T. Takahashi, T. Oguchi, K. Segawa, and Y. Ando, "Topological proximity effect in a topological insulator hybrid," *Nature Communications*, vol. 6, pp. 6547 EP –, Mar 2015. Article.

[92] D. S. Inosov, V. B. Zabolotnyy, D. V. Evtushinsky, A. A. Kordyuk, B. Bchner, R. Follath, H. Berger, and S. V. Borisenko, "Fermi surface nesting in several transition metal dichalcogenides," *New Journal of Physics*, vol. 10, no. 12, p. 125027, 2008.

[93] D. J. Rahn, S. Hellmann, M. Kalläne, C. Sohrt, T. K. Kim, L. Kipp, and K. Rossnagel, "Gaps and kinks in the electronic structure of the superconductor $2h$-$nbse_2$ from angle-resolved photoemission at 1 k," *Phys. Rev. B*, vol. 85, p. 224532, Jun 2012.

[94] M. M. Ugeda, A. J. Bradley, Y. Zhang, S. Onishi, Y. Chen, W. Ruan, C. Ojeda-Aristizabal, H. Ryu, M. T. Edmonds, H.-Z. Tsai, A. Riss, S.-K. Mo, D. Lee, A. Zettl, Z. Hussain, Z.-X. Shen, and M. F. Crommie, "Characterization of collective ground states in single-layer nbse2," *Nat Phys*, vol. 12, pp. 92–97, Jan 2016. Article.

[95] C.-X. Liu, X.-L. Qi, H. Zhang, X. Dai, Z. Fang, and S.-C. Zhang, "Model hamiltonian for topological insulators," *Phys. Rev. B*, vol. 82, p. 045122, Jul 2010.

[96] P. D. Gennes, *Superconductivity of Metals and Alloys*. W. A. Benjamin, New York, 1966.

[97] W. Chen, M. Gong, R. Shen, and D. Y. Xing, "Detecting fuldeferrell superconductors by an andreev interferometer," *New Journal of Physics*, vol. 16, no. 8, p. 083024, 2014.

[98] G. E. Blonder, M. Tinkham, and T. M. Klapwijk, "Transition from metallic to tunneling regimes in superconducting microconstrictions: Excess current, charge imbalance, and supercurrent conversion," *Phys. Rev. B*, vol. 25, pp. 4515–4532, Apr 1982.

[99] X. Wan, A. M. Turner, A. Vishwanath, and S. Y. Savrasov, "Topological semimetal and fermi-arc surface states in the electronic structure of pyrochlore iridates," *Phys. Rev. B*, vol. 83, p. 205101, May 2011.

[100] C.-K. Chiu and A. P. Schnyder, "Classification of reflection-symmetry-protected topological semimetals and nodal superconductors," *Phys. Rev. B*, vol. 90, p. 205136, Nov 2014.

[101] Z. Fang, N. Nagaosa, K. S. Takahashi, A. Asamitsu, R. Mathieu, T. Ogasawara, H. Yamada, M. Kawasaki, Y. Tokura, and K. Terakura, "The anomalous hall effect and magnetic monopoles in momentum space," *Science*, vol. 302, no. 5642, pp. 92–95, 2003.

[102] H. Nielsen and M. Ninomiya, "Absence of neutrinos on a lattice: (i). proof by homotopy theory," *Nuclear Physics B*, vol. 185, no. 1, pp. 20 – 40, 1981.

[103] H. Nielsen and M. Ninomiya, "Absence of neutrinos on a lattice: (ii). intuitive topological proof," *Nuclear Physics B*, vol. 193, no. 1, pp. 173 – 194, 1981.

[104] R. Okugawa and S. Murakami, "Dispersion of fermi arcs in weyl semimetals and their evolutions to dirac cones," *Phys. Rev. B*, vol. 89, p. 235315, Jun 2014.

[105] S.-Y. Xu, I. Belopolski, N. Alidoust, M. Neupane, G. Bian, C. Zhang, R. Sankar, G. Chang, Z. Yuan, C.-C. Lee, S.-M. Huang, H. Zheng, J. Ma, D. S. Sanchez, B. Wang, A. Bansil, F. Chou, P. P. Shibayev, H. Lin, S. Jia, and M. Z. Hasan, "Discovery of a weyl fermion semimetal and topological fermi arcs," *Science*, vol. 349, no. 6248, pp. 613–617, 2015.

[106] P. Hosur and X. Qi, "Recent developments in transport phenomena in weyl semimetals," *Comptes Rendus Physique*, vol. 14, no. 910, pp. 857 – 870, 2013. Topological insulators / Isolants topologiquesTopological insulators / Isolants topologiques.

[107] G. Y. Cho, J. H. Bardarson, Y.-M. Lu, and J. E. Moore, "Superconductivity of doped weyl semimetals: Finite-momentum pairing and electronic analog of the ^{3}he-a phase," *Phys. Rev. B*, vol. 86, p. 214514, Dec 2012.

[108] G. Bednik, A. A. Zyuzin, and A. A. Burkov, "Superconductivity in weyl metals," *Phys. Rev. B*, vol. 92, p. 035153, Jul 2015.

[109] P. Hosur, X. Dai, Z. Fang, and X.-L. Qi, "Time-reversal-invariant topological superconductivity in doped weyl semimetals," *Phys. Rev. B*, vol. 90, p. 045130, Jul 2014.

[110] B. Lu, K. Yada, M. Sato, and Y. Tanaka, "Crossed surface flat bands of weyl semimetal superconductors," *Phys. Rev. Lett.*, vol. 114, p. 096804, Mar 2015.

[111] Y. Li and F. D. M. Haldane, "Topological nodal cooper pairing in doped weyl metals," *Phys. Rev. Lett.*, vol. 120, p. 067003, Feb 2018.

[112] P. Fulde and R. A. Ferrell, "Superconductivity in a strong spin-exchange field," *Phys. Rev.*, vol. 135, pp. A550–A563, Aug 1964.

[113] A. Larkin and Y. Ovchinnikov, "Nonuniform state of superconductors," *Sov. Phys. JETP*, vol. 20, pp. 762–770, Mar 1965.

[114] K. Yang and D. F. Agterberg, "Josephson effect in fulde-ferrell-larkin-ovchinnikov superconductors," *Phys. Rev. Lett.*, vol. 84, pp. 4970–4973, May 2000.

[115] P. E. C. Ashby and J. P. Carbotte, "Magneto-optical conductivity of weyl semimetals," *Phys. Rev. B*, vol. 87, p. 245131, Jun 2013.

[116] J. Bardeen, "Critical fields and currents in superconductors," *Rev. Mod. Phys.*, vol. 34, pp. 667–681, Oct 1962.

[117] I. Khavkine, H.-Y. Kee, and K. Maki, "Supercurrent in nodal superconductors," *Phys. Rev. B*, vol. 70, p. 184521, Nov 2004.

[118] K.-Y. Yang, Y.-M. Lu, and Y. Ran, "Quantum hall effects in a weyl semimetal: Possible application in pyrochlore iridates," *Phys. Rev. B*, vol. 84, p. 075129, Aug 2011.

[119] H. Shapourian and T. L. Hughes, "Phase diagrams of disordered weyl semimetals," *Phys. Rev. B*, vol. 93, p. 075108, Feb 2016.

[120] H. Jiang, L. Wang, Q.-f. Sun, and X. C. Xie, "Numerical study of the topological anderson insulator in hgte/cdte quantum wells," *Phys. Rev. B*, vol. 80, p. 165316, Oct 2009.

[121] C. W. Groth, M. Wimmer, A. R. Akhmerov, J. Tworzydło, and C. W. J. Beenakker, "Theory of the topological anderson insulator," *Phys. Rev. Lett.*, vol. 103, p. 196805, Nov 2009.

[122] K. Kobayashi, T. Ohtsuki, and K.-I. Imura, "Disordered weak and strong topological insulators," *Phys. Rev. Lett.*, vol. 110, p. 236803, Jun 2013.

[123] P. Titum, N. H. Lindner, M. C. Rechtsman, and G. Refael, "Disorder-induced floquet topological insulators," *Phys. Rev. Lett.*, vol. 114, p. 056801, Feb 2015.

[124] S. Ryu and K. Nomura, "Disorder-induced quantum phase transitions in three-dimensional topological insulators and superconductors," *Phys. Rev. B*, vol. 85, p. 155138, Apr 2012.

[125] J. Li, R.-L. Chu, J. K. Jain, and S.-Q. Shen, "Topological anderson insulator," *Phys. Rev. Lett.*, vol. 102, p. 136806, Apr 2009.

[126] H.-M. Guo, G. Rosenberg, G. Refael, and M. Franz, "Topological anderson insulator in three dimensions," *Phys. Rev. Lett.*, vol. 105, p. 216601, Nov 2010.

[127] Y. Xu, F. Zhang, and C. Zhang, "Structured weyl points in spin-orbit coupled fermionic superfluids," *Phys. Rev. Lett.*, vol. 115, p. 265304, Dec 2015.

[128] B. Q. Lv, H. M. Weng, B. B. Fu, X. P. Wang, H. Miao, J. Ma, P. Richard, X. C. Huang, L. X. Zhao, G. F. Chen, Z. Fang, X. Dai, T. Qian, and H. Ding, "Experimental discovery of weyl semimetal taas," *Phys. Rev. X*, vol. 5, p. 031013, Jul 2015.

[129] S.-Y. Xu, I. Belopolski, N. Alidoust, M. Neupane, G. Bian, C. Zhang, R. Sankar, G. Chang, Z. Yuan, C.-C. Lee, S.-M. Huang, H. Zheng, J. Ma, D. S. Sanchez, B. Wang, A. Bansil, F. Chou, P. P. Shibayev, H. Lin, S. Jia, and M. Z. Hasan, "Discovery of a weyl fermion semimetal and topological fermi arcs," *Science*, vol. 349, no. 6248, pp. 613–617, 2015.

[130] X. Wan, A. M. Turner, A. Vishwanath, and S. Y. Savrasov, "Topological semimetal and fermi-arc surface states in the electronic structure of pyrochlore iridates," *Phys. Rev. B*, vol. 83, p. 205101, May 2011.

[131] K.-Y. Yang, Y.-M. Lu, and Y. Ran, "Condensed matter field theory," *Phys. Rev. B*, vol. 84, p. 075129, Aug 2011.

[132] S. A. Parameswaran, T. Grover, D. A. Abanin, D. A. Pesin, and A. Vishwanath, "Probing the chiral anomaly with nonlocal transport in three-dimensional topological semimetals," *Phys. Rev. X*, vol. 4, p. 031035, Sep 2014.

[133] N. Xu and et al. 2016.

[134] A. Liang and et al. 2016.

[135] C. Wang, Y. Zhang, J. Huang, S. Nie, G. Liu, A. Liang, Y. Zhang, B. Shen, J. Liu, C. Hu, Y. Ding, D. Liu, Y. Hu, S. He, L. Zhao, L. Yu, J. Hu, J. Wei, Z. Mao, Y. Shi, X. Jia, F. Zhang, S. Zhang, F. Yang, Z. Wang, Q. Peng, H. Weng, X. Dai, Z. Fang, Z. Xu, C. Chen, and X. J. Zhou, "Observation of fermi arc and its connection with bulk states in the candidate type-ii weyl semimetal wte_2," *Phys. Rev. B*, vol. 94, p. 241119, Dec 2016.

[136] F. Y. Bruno, A. Tamai, Q. S. Wu, I. Cucchi, C. Barreteau, A. de la Torre, S. McKeown Walker, S. Riccò, Z. Wang, T. K. Kim, M. Hoesch, M. Shi, N. C. Plumb, E. Giannini, A. A. Soluyanov, and F. Baumberger, "Observation of large topologically trivial fermi arcs in the candidate type-ii weyl semimetal WTe_2," *Phys. Rev. B*, vol. 94, p. 121112, Sep 2016.

[137] M. Udagawa and E. J. Bergholtz, "Field-selective anomaly and chiral mode reversal in type-ii weyl materials," *Phys. Rev. Lett.*, vol. 117, p. 086401, Aug 2016.

[138] T. E. O'Brien, M. Diez, and C. W. J. Beenakker, "Magnetic breakdown and klein tunneling in a type-ii weyl semimetal," *Phys. Rev. Lett.*, vol. 116, p. 236401, Jun 2016.

[139] M. Koshino, "Cyclotron resonance of figure-of-eight orbits in a type-ii weyl semimetal," *Phys. Rev. B*, vol. 94, p. 035202, Jul 2016.

[140] R. Queiroz and A. P. Schnyder, "Helical majorana surface states of strongly disordered topological superconductors with time-reversal symmetry," *Phys. Rev. B*, vol. 91, p. 014202, Jan 2015.

[141] A. A. Burkov and L. Balents, "Weyl semimetal in a topological insulator multilayer," *Phys. Rev. Lett.*, vol. 107, p. 127205, Sep 2011.

[142] C. Fang, M. J. Gilbert, X. Dai, and B. A. Bernevig, "Multi-weyl topological semimetals stabilized by point group symmetry," *Phys. Rev. Lett.*, vol. 108, p. 266802, Jun 2012.

[143] F.-Y. Li, X. Luo, X. Dai, Y. Yu, F. Zhang, and G. Chen, "Hybrid weyl semimetal," *Phys. Rev. B*, vol. 94, p. 121105, Sep 2016.

[144] A. Altland and B. D. Simons, *Condensed Matter Field theory*. Cambridge, 2010.

[145] C.-Z. Chen, J. Song, H. Jiang, Q.-f. Sun, Z. Wang, and X. C. Xie, "Disorder and metal-insulator transitions in weyl semimetals," *Phys. Rev. Lett.*, vol. 115, p. 246603, Dec 2015.

[146] J. Song, H. Liu, H. Jiang, Q.-f. Sun, and X. C. Xie, "Dependence of topological anderson insulator on the type of disorder," *Phys. Rev. B*, vol. 85, p. 195125, May 2012.

[147] S. Datta, *Quantum Transport: Atom to Transistor*. Cambridge University Press, 2013.

[148] X. Huang, L. Zhao, Y. Long, P. Wang, D. Chen, Z. Yang, H. Liang, M. Xue, H. Weng, Z. Fang, X. Dai, and G. Chen, "Observation of the chiral-anomaly-induced negative magnetoresistance in 3d weyl semimetal taas," *Phys. Rev. X*, vol. 5, p. 031023, Aug 2015.

[149] J. Xiong, S. K. Kushwaha, T. Liang, J. W. Krizan, M. Hirschberger, W. Wang, R. J. Cava, and N. P. Ong, "Evidence for the chiral anomaly in the dirac semimetal na3bi," *Science*, vol. 350, no. 6259, pp. 413–416, 2015.

[150] C.-L. Zhang, S.-Y. Xu, I. Belopolski, Z. Yuan, Z. Lin, B. Tong, G. Bian, N. Alidoust, C.-C. Lee, S.-M. Huang, T.-R. Chang, G. Chang, C.-H. Hsu, H.-T. Jeng, M. Neupane, D. S. Sanchez, H. Zheng, J. Wang, H. Lin, C. Zhang, H.-Z. Lu, S.-Q. Shen, T. Neupert, M. Zahid Hasan, and S. Jia, "Signatures of the adler-bell-jackiw chiral anomaly in a weyl fermion semimetal," *Nat Commun*, vol. 7, p. 10735, Feb 2016. 26911701[pmid].

[151] S. A. Parameswaran, T. Grover, D. A. Abanin, D. A. Pesin, and A. Vishwanath, "Probing the chiral anomaly with nonlocal transport in three-dimensional topological semimetals," *Phys. Rev. X*, vol. 4, p. 031035, Sep 2014.

[152] P. Hosur, S. A. Parameswaran, and A. Vishwanath, "Charge transport in weyl semimetals," *Phys. Rev. Lett.*, vol. 108, p. 046602, Jan 2012.

[153] H.-J. Kim, K.-S. Kim, J.-F. Wang, M. Sasaki, N. Satoh, A. Ohnishi, M. Kitaura, M. Yang, and L. Li, "Dirac versus weyl fermions in topological insulators: Adler-bell-jackiw anomaly in transport phenomena," *Phys. Rev. Lett.*, vol. 111, p. 246603, Dec 2013.

[154] Q. Li, D. E. Kharzeev, C. Zhang, Y. Huang, I. Pletikosic, A. . V. Fedorov, R. . D. Zhong, J. . A. Schneeloch, G. . D. Gu, and T. Valla, "Chiral magnetic effect in zrte5," *Nature Physics*, vol. 12, pp. 550 EP –, Feb 2016.

[155] P. Goswami, G. Sharma, and S. Tewari, "Optical activity as a test for dynamic chiral magnetic effect of weyl semimetals," *Phys. Rev. B*, vol. 92, p. 161110, Oct 2015.

[156] M. N. Chernodub, A. Cortijo, A. G. Grushin, K. Landsteiner, and M. A. H. Vozmediano, "Condensed matter realization of the axial magnetic effect," *Phys. Rev. B*, vol. 89, p. 081407, Feb 2014.

[157] M.-C. Chang and M.-F. Yang, "Chiral magnetic effect in a two-band lattice model of weyl semimetal," *Phys. Rev. B*, vol. 91, p. 115203, Mar 2015.

[158] M. M. Vazifeh and M. Franz, "Electromagnetic response of weyl semimetals," *Phys. Rev. Lett.*, vol. 111, p. 027201, Jul 2013.

[159] D. I. Pikulin, A. Chen, and M. Franz, "Chiral anomaly from strain-induced gauge fields in dirac and weyl semimetals," *Phys. Rev. X*, vol. 6, p. 041021, Oct 2016.

[160] A. Cortijo, D. Kharzeev, K. Landsteiner, and M. A. H. Vozmediano, "Strain-induced chiral magnetic effect in weyl semimetals," *Phys. Rev. B*, vol. 94, p. 241405, Dec 2016.

[161] K. Fujikawa, "Path integral for gauge theories with fermions," *Phys. Rev. D*, vol. 21, pp. 2848–2858, May 1980.

[162] K. Fujikawa, "Path-integral measure for gauge-invariant fermion theories," *Phys. Rev. Lett.*, vol. 42, pp. 1195–1198, Apr 1979.

[163] S.-C. Zhang and J. Hu, "A four-dimensional generalization of the quantum hall effect," *Science*, vol. 294, no. 5543, pp. 823–828, 2001.

[164] S. L. Adler, "Axial-vector vertex in spinor electrodynamics," *Phys. Rev.*, vol. 177, pp. 2426–2438, Jan 1969.

[165] J. Bell and R. Jackiw *Il Nuovo Cimento*, vol. 60, p. 47, 1969.

[166] R. B. Laughlin, "Quantized hall conductivity in two dimensions," *Phys. Rev. B*, vol. 23, pp. 5632–5633, May 1981.

[167] K. Landsteiner, "Anomalous transport of weyl fermions in weyl semimetals," *Phys. Rev. B*, vol. 89, p. 075124, Feb 2014.

[168] D. T. Son and B. Z. Spivak, "Chiral anomaly and classical negative magnetoresistance of weyl metals," *Phys. Rev. B*, vol. 88, p. 104412, Sep 2013.

[169] F. Zhang and C. L. Kane, "Time-reversal-invariant Z_4 fractional josephson effect," *Phys. Rev. Lett.*, vol. 113, p. 036401, Jul 2014.

[170] L. Fu and C. L. Kane, "Time reversal polarization and a Z_2 adiabatic spin pump," *Phys. Rev. B*, vol. 74, p. 195312, Nov 2006.

[171] S. Ryu, J. E. Moore, and A. W. W. Ludwig, "Electromagnetic and gravitational responses and anomalies in topological insulators and superconductors," *Phys. Rev. B*, vol. 85, p. 045104, Jan 2012.

[172] K. Nomura, S. Ryu, A. Furusaki, and N. Nagaosa, "Cross-correlated responses of topological superconductors and superfluids," *Phys. Rev. Lett.*, vol. 108, p. 026802, Jan 2012.

[173] S. Ryu and S. C. Zhang *Phys. Rev. B*, vol. 85, p. 245132, 2012.

[174] O. M. Sule, X. Chen, and S. Ryu *Phys. Rev. B*, vol. 88, p. 075125, 2013.

[175] C.-T. Hsieh, O. M. Sule, G. Y. Cho, S. Ryu, and R. G. Leigh, "Symmetry-protected topological phases, generalized laughlin argument, and orientifolds," *Phys. Rev. B*, vol. 90, p. 165134, Oct 2014.

[176] A. Cappelli and E. Randellini, "Partition functions and stability criteria of topological insulators," *Journal of High Energy Physics*, vol. 2013, no. 12, 2013.

[177] C.-T. Hsieh, G. Y. Cho, and S. Ryu, "Global anomalies on the surface of fermionic symmetry-protected topological phases in (3+1) dimensions," *Phys. Rev. B*, vol. 93, p. 075135, Feb 2016.

[178] J. Polchinski, *String Theory.* Cambridge University Press, 1998.

[179] E. Witten *Commum. Math. Phys.*, vol. 100, p. 197, 1985.

[180] See supplemental material at [URL will be inserted by publisher].

[181] A. Cappelli and G. R. Zemba *Nucl. Phys. B*, vol. 490, p. 595, 1997.

[182] S. Hawking *Commun. Math. Phys.*, vol. 55, p. 133, 1977.

[183] A. Actor *J. Phys. A*, vol. 24, p. 3741, 1991.

[184] E. Elizalde, *Ten Physical Applications of Spectral Zeta Functions*. Springer, 2012.

[185] H. S. M. Coxeter and W. O. J. Moser, *Generators and Relations for Discrete Groups*. Springer, 1980.